Dynamics in Nanosystems

Dissertation

zur Erlangung des Doktorgrades
des Fachbereichs Physik
der Universität Hamburg

vorgelegt von

Benjamin Baxevanis

aus
Preetz

Hamburg

2014

Gutachterin der Dissertation:	Prof. Dr. D. Pfannkuche
	Prof. Dr. Joaquín Fernández Rossier
Gutachterin/Gutachter der Disputation:	Prof. Dr. Daniela Pfannkuche
	Dr. Alexander Khajetoorians
Datum der Disputation:	26. November 2013
Vorsitzender des Prüfungsausschusses:	Prof. Dr. Alexander Lichtenstein
Vorsitzender des Promotionsausschusses:	Prof. Dr. Peter Hauschildt
Dekan der MIN Fakultät:	Prof. Dr. Heinrich Graener

To Ursula and Athanasios

This page intentionally left blank.

Abstract

In this thesis, we study charge and spin dynamics in nanostructures such as quantum dots and small ferromagnetic clusters. These systems are brought out of equilibrium by an external perturbation like the coupling to electron baths or an abrupt change of electric fields.

To investigate the interactions and mechanisms defining the time scales of the dynamics in quantum dots and small magnetic clusters, we use model systems and the master equation approach. As a further method of choice, we implement the quantum Monte Carlo method for non-equilibrium systems.

First, the charging dynamics of quantum dots that are tunnel coupled to a two-dimensional electron gas are investigated after abruptly changing the gate potential. We show that the charging dynamics of the quantum dots are defined by the degeneracy of states and by the interplay between Coulomb correlations and relaxation processes. We discuss how to disentangle the influence of each contribution in the spectra obtained by time-resolved spectroscopy of the electron gas conductivity.

The second part of the thesis is concerned with spin dynamics of a small ferromagnetic cluster that consists of five iron atoms deposited on a non-magnetic, conducting substrate. A current flowing between a scanning tunnel microscope tip and the substrate inelastically excites the spin. We find that in the regime of weak coupling between the tip and the cluster, the current gives rise to spin noise, originating from a bi-stability of the system. We show that the spin noise can be measured in the current noise, which can be used to probe the cluster dynamics governed by inelastic spin excitation and anisotropy-induced magnetization tunneling.

Both model systems were analyzed with the master equation approach, which has proven to adequately describe the dynamics of systems that are weakly coupled to an electron bath. Finally, we implement the quantum Monte Carlo (QMC) approach for non-equilibrium situations. This numerical method is capable of describing the time evolution of systems with arbitrary interactions and couplings. We concentrate on two particular implementations of non-equilibrium QMC: one based on the expansion in the tunnel coupling, the other on the expansion in the Coulomb interaction. Both

approaches are applied to a single-level quantum dot that is tunnel coupled to electron reservoirs. We discuss their applicability and limitations due to the dynamical sign problem with regard to the time dependence after initiating the tunnel coupling. We show that the implementation of the tunnel coupling expansion is independent of the interaction strength. It is, however, limited in the simulated time. The expansion in the Coulomb interaction, on the other hand, allows for slightly longer simulation times that, then again, strongly depend on the interaction strength.

In a further step, we analyze the single-level quantum dot with an embedded impurity by extending the tunnel coupling expansion approach accordingly. This reduced model for dilute magnetic quantum dots exhibits different regimes depending on the exchange interaction strength between electron and impurity. We find that weak exchange interaction resembles an effective magnetic field, while strong exchange interaction increases the relevance of coherent spin-flip processes.

Kurzfassung

In dieser Arbeit untersuchen wir Ladungs- und Spin-Dynamik in Nanostrukturen wie Quantenpunkten und kleinen ferromagnetischen Clustern. Diese Systeme werden durch eine externe Störung, wie etwa die Kopplung an ein Elektronenreservoir oder die abrupte Änderung äußerer elektrischer Felder, aus dem Gleichgewicht gebracht.

Um die Wechselwirkungen und Mechanismen zu untersuchen, welche die dynamischen Zeitskalen in Quantenpunkten und kleinen magnetischen Clustern bestimmen, verwenden wir Modellsysteme zusammen mit der Master-Gleichung. Des Weiteren stellen wir die Implementierung der Quanten-Monte-Carlo-Methode für Nicht-Gleichgewichts-Systeme vor.

Zuerst untersuchen wir die Ladungsdynamik von Quantenpunkten, die an ein zweidimensionales Elektronengas gekoppelt sind, nachdem die Gate-Spannung abrupt geändert wurde. Wir zeigen, dass die Ladungsdynamik der Quantenpunkte durch die Entartung der Zustände sowie durch das Wechselspiel zwischen Coulomb-Korrelationen und Relaxationsprozessen festgelegt ist. Wir erörtern dann, wie sich die verschiedenen Einflüsse in zeitaufgelösten Spektren der experimentell bestimmten Leitfähigkeit des Elektronengases widerspiegeln.

Der zweite Teil der Arbeit beschäftigt sich mit der Spindynamik eines kleinen ferromagnetischen Clusters bestehend aus fünf Eisenatomen, die auf einem nicht-magnetischen, leitenden Substrat aufgebracht sind. Ein Strom, der zwischen der Spitze eines Rastertunnelmikroskops und dem Substrat fließt, führt zu inelastischen Spinanregungen des Clusters. Hier zeigt sich, dass im Regime schwacher Kopplung zwischen der Spitze und dem Cluster der Strom ein Spinrauschen erzeugt, welches von einer Bistabilität des Systems herrührt. Wir zeigen, dass sich das Spinrauschen im Rauschen des Stroms widerspiegelt. Die Messung dieses Stromrauschens kann dann verwendet werden, um die Cluster-Dynamik zu bestimmen, welche durch inelastische Spinanregung und Anisotropie-induzierte Magnetisierung charakterisiert ist.

Diese beiden Modellsysteme wurden zunächst mit Hilfe einer Master-Gleichung untersucht, welche die Dynamik von Systemen mit schwacher Kopplung an ein Elektronenreservoir beschreiben kann. Diese Betrachtung wird schließlich erweitert, indem wir

eine Quanten-Monte-Carlo (QMC) Methode für Nicht-Gleichgewichts-Systeme implementieren. Dieses numerische Verfahren ermöglicht die Beschreibung der zeitlichen Entwicklung von Systemen mit beliebiger Wechselwirkungs- und Kopplungsstärke.

Wir konzentrieren uns auf zwei Implementierungen der Nicht-Gleichgewichts-QMC: eine basierend auf der Entwicklung in der Tunnelkopplung, die andere basierend auf der Entwicklung in der Coulomb-Wechselwirkungsstärke. Beide Ansätze werden angewendet auf einen Quantenpunkt mit einem einzigen elektronischen Niveau, der an ein Elektronenreservoir gekoppelt ist. Wir diskutieren Anwendbarkeit und Einschränkungen der Methoden im Zusammenhang mit dem dynamischen Vorzeichenproblem für die Zeitentwicklung nach Einschalten der Tunnelkopplung. Hier zeigen wir, dass Berechnungen basierend auf der Entwicklung in der Tunnelkopplung zwar unabhängig von der Stärke der Wechselwirkung sind, jedoch die simulierbare Zeit beschränkt ist. Die Entwicklung in der Coulomb-Wechselwirkungsstärke auf der anderen Seite, ermöglicht die Simulation längerer Zeiten, deren Dauer allerdings stark von der Wechselwirkungsstärke abhängig ist.

In einem weiteren Schritt analysieren wir einen Quantenpunkt, in den zusätzlich eine magnetische Störstelle eingebracht wurde, indem wir den Tunnelkopplungsansatz erweitern. Dieses System dient als reduziertes Modell für magnetische Quantenpunkte und zeigt unterschiedliche Regime in Abhängigkeit der Austauschwechselwirkungsstärke zwischen Elektronen und Störstelle. Eine schwache Austauschwechselwirkung wirkt wie ein effektives Magnetfeld, während für starke Austauschwechselwirkungen kohärente Spin-Flip-Prozesse an Relevanz für die Dynamik des gekoppelten Systems gewinnen.

Acknowledgments

First I want to thank my family and friends for their love, understanding and unconditional support during all these years. Without your constant encouragement, the way would have been much harder for me.

I am truly indebted to my thesis advisor Daniela Pfannkuche. Since my time as an undergraduate at the University of Hamburg, she has been a mentor and guide. Writing this thesis would not have been possible without her support and encouragement. I also enjoyed our hour-long discussions that genuinely enriched my understanding of physics. She has had the talent to create a truly great working environment, which helped me to develop my own research profile.

I wish to thank Michael Karolak for being a friend and companion since many years. A further big thanks is directed to my office mates and colleagues during the years, Christoph Hübner, Maximilian Hollstein, Theo Gerhardt, Claas Abert, Alexander Lieder, Daniel Becker, Mohammad Sayad, Peter Miraczewski and Jacek Swiebodzinski for always being open for questions and discussions, but also for providing welcome distractions and their company in recreational lunch and coffee hours.

During my thesis work, I had the chance to collaborate with many great scientists, without whom this thesis would not have got into its final shape.

In particular I would like to acknowledge Alexander Khajetoorians at the University of Hamburg for giving me the chance to collaborate in the analysis of cluster dynamics and for generously sharing his experimental measurement data. I learned a lot from him about experimental approaches and how theoreticians and experimentalists can work together successfully to make better science.

In this context, I also would like to thank Axel Lorke at the University of Duisburg and his team members Andreas Beckel, Bastian Marquardt and Paul Martin Geller for the fruitful collaborations on the charge dynamics in quantum dots and for inviting me to Duisburg.

Alexander Lichtenstein at the University of Hamburg has provided very valuable guidance and ideas for the quantum Monte Carlo part of my thesis. I thank him for always having an open ear for my questions and for always providing catchy explanations.

Andrei Manolescu and his group are thanked for their warm invitation to the University of Iceland and the enlightening conversations about master equations.

Furthermore, I would like to acknowledge the helpful discussions and scientific exchange with Jens Wiebe, Michael Thorwart, Jürgen König, Tobias Schlenk, Alexander Chudnovskiy and Michael Potthoff.

I want to express my gratitude to the theoretical physics institute's staff, especially Bodo Krause-Kyora for his flexible and unconventional help in IT matters.

Finally, I thank the thesis committee for putting time and work into the review process.

Contents

1 Dynamics in Nanostructures

1.1 Introduction

Condensed matter physics deals with the states of matter in which the spatial proximity between individual atoms is sufficient to form a condensed state due to mutual interactions. The involved states range from hard matter – crystalline solids, glasses, metals, insulators, and semiconductors – to soft matter, including e.g. liquids, polymers, granular materials, but also a number of biological materials.

The physical description of such systems takes place at the crossroads of quantum mechanics, electromagnetism and statistical mechanics. In this sense, condensed matter physics provides the quantum-mechanical foundation for the classical physics of mechanics, electronics or thermodynamics. Despite its fundamental aspects, condensed matter science plays an extraordinary role in technological advancements and has been the source of technologies like the transistor, semiconductor chips and solid-state lasers. Hence, condensed matter physics has a profound impact on our daily lives and the way we communicate and compute.

In this context, the branch of condensed matter physics dealing with nanometer-sized structures has taken a special role. The typical scales of these so-called *nanostructures* are large compared to microscopic (atomic) scales, but small compared to the macroscopic (classical) scales. Such systems typically consist of a large number of atoms, but their behavior is considerably influenced by quantum interference effects. Particular prominent examples of quantum nanostructures are *quantum dots* that are manufactured in such a way that a small number of electrons can be confined in all spatial dimension producing an effectively zero-dimensional system. Quantum dots can be experimentally realized in processed semiconductors, carbon nanotubes or single molecules. Sophisticated experimental approaches allow to connect quantum dots to electric wires in order to probe and characterize their electronic properties. Most notable observations are signatures of single-electron tunneling and the Coulomb blockade effect [1, 2], and the detection of the Kondo effect [3, 4], which is the analog to the interaction of conduction electrons with magnetic impurities in metals [5]. The high degree of experimental control as well as the model character of quantum dots have also resulted in an increasing

interest in their *dynamical* characteristics, not at least pursuing the goal of constructing new devices for quantum computation and solid-state storage [6, 7].

With the advance of high-resolution measurement techniques, access to time-resolved transport experiments on nanostructures has become available. In the spirit of optical pump-probe experiments [8], nanostructures are being brought out of equilibrium and their approach to e.g. a steady state is recorded. Examples are experiments conducted by Marquardt et al. [9] on quantum dot ensembles in contact with a two-dimensional electron gas (2DEG). A gate voltage pulse (pump) creates a non-equilibrium condition between the system that leads to electron hopping. The time-resolved charge transfer can be monitored by measuring the response of the 2DEG (probe). Another example are scanning tunneling microscopy (STM) experiments conducted on small nanostructures that are created by assembling atom by atom [10–12]. Recently, it has been possible to measure the time-resolved spin relaxation of a magnetic atom [13] and spin switching in ferromagnetic and anti-ferromagnetic clusters composed of only a few iron atoms [14,15]. The utilized STM tip can act both as a pump exciting the spin of atoms as well as the probe recording the spin relaxation or switching.

Understanding the dynamics in these systems is also important for feasibility considerations in quantum information, for example, concerning the time span for which a (quantum) bit of information is preserved or write and read out durations. However, studying dynamics can also provide answers to fundamental questions regarding processes that define the time evolution of nanodevices. Examples are the role of coherences and correlations as well as the interplay of interaction types in the systems. In the present thesis, we develop model systems that are able to describe experimental situations and we extract the physical effects defining the charge and spin dynamics. For this purpose, master equations have proven to adequately describe many physical situations and, at the same time, offer an intuitive explanation of physics involved. At the same time, they allow for analytical solutions or require only moderate computational power.

In the absence of a small expansion parameter, on the other hand, the master equation approach is inappropriate due to its perturbative nature. This regime has lately become a thriving research field in developing theoretical approaches that can describe non-equilibrium physics in the strongly correlated regime. While an universal approach is not available up to date, a number of analytical and numerical methods have been proposed, which go beyond ordinary perturbation theory. Many of them can be categorized in two classes depending on their starting point. One class starts from the expansion in the tunnel coupling and systematically includes higher order expansion terms. This approach follows e.g. renormalization group (RG) theory [16–18] or the influence path

integral technique (INFPI) [19, 20]. The second class of approaches is based on the perturbative expansion in the Coulomb interaction. In the iterative summation of path integrals (ISPI) method [21, 22], for example, the Hubbard-Stratonovich transformation is employed to decouple the quartic field operators in the Coulomb interaction term. The expansion in orders of the resulting auxiliary field is then iteratively implemented including a finite time history of the system. Although these methods go beyond ordinary perturbation theory, they are restricted to a sufficiently large bias or temperature regime, resulting from their perturbative foundation.

A special part in the zoo of non-equilibrium methods takes the diagrammatic quantum Monte Carlo (QMC) approach. It is based on the path-integral expansion of the density matrix and has recently been adapted to non-equilibrium situations. QMC comes in two versions: either based on an expansion in the tunnel coupling or in the Coulomb interaction.

Each of these methods has been applied to the Anderson impurity model that often serves as a drosophila for the theoretical description of equilibrium and transport effects. Originally developed to describe resonances between conduction electrons in a metal interacting with embedded magnetic impurities [23], today it serves as a model for a variety of quantum systems ranging from atoms and molecules to quantum dots. Its particular appeal arises from its, at first glance, simple structure: A single, spin-degenerate electronic level with Coulomb interaction is tunnel coupled to a macroscopic electron reservoir. Despite its idealized model character, the impurity model shows rich dynamics, while allowing to (qualitatively) describe features of larger systems.

1.2 Scope and contributions of this thesis

This thesis is devoted to the analysis of non-equilibrium dynamics of nanostructures. In the subsequent section, we introduce the non-interacting Anderson impurity model and study its non-equilibrium dynamics. The Anderson impurity model in the limit of vanishing Coulomb interaction resembles the resonant level model. Its analytical solution will be derived and the transient dynamics in this system are discussed. Following up, the master equation approach is introduced defining the equation of motion of the density matrix for systems in the weak tunnel coupling regime. The master equation approach as well as the discussion of the resonant level model will provide the foundation for the following chapters.

In chapter 2, the master equation approach is applied to determine the charging dynamics of a quantum dot coupled to an electron reservoir with the intention to better

understand the role of Coulomb interaction and relaxation processes in the system and in particular the time-dependent occupation probabilities observed in recent experiments [9, 24,25]. To incorporate many-body effects, the eigenstates of a finite number of correlated electrons in the quantum dot obtained by the exact diagonalization method are taken into account. The electrons in the quantum dot can interact with phonons and nuclear spins, which leads to two types of relaxation processes: 1. orbital relaxation in the dot, which is instantaneous compared to the tunneling dynamics and 2. spin relaxation with a time scale that can be in the order of the tunneling times. A detailed analysis of the time dependence reveals the complex interplay between Coulomb correlations and different spin-relaxation mechanisms.

Chapter 3 deals with the spin dynamics in a small ferromagnetic cluster on a non-magnetic substrate. Few-atom systems have revealed magnetic bi-stability at low temperatures, which manifests in a measured telegraph (flicker) signal [14, 15, 26–29]. Magnetic bi-stabilities are not only of interest as a potential implementation of information storage, but also because they shed light on the role of the interaction between substrate and tip in the dynamics of an atomic-scale magnet. We show how the dynamic time scales can be extracted from noise measurements and reveal that the switching is governed by the interplay of inelastic spin excitations and magnetization tunneling.

Chapters 2 and 3 both have an experimental motivation and the experimental parameters allowed for an perturbative treatment in the framework of the master equation approach. In chapter 4, we depart from the weak tunnel coupling regime and deal with the non-Markovian dynamics of quantum dots without small parameters. The method of choice is the recently developed non-equilibrium Monte Carlo approach [30–32]. We will introduce the weak tunnel coupling flavor of QMC and develop a particular version for the strong tunnel coupling regime. The testbed for the comparison of the two methods will be the Anderson impurity model. In strong tunnel coupling QMC, auxiliary parameters will be introduced, which has been shown to compensate the sign problem in equilibrium. We will investigate the role of these parameters in non-equilibrium and their potential in managing the sign problem. The weak tunnel coupling version of QMC is extended to treat a wider class of systems by implementing the *magnetic Anderson impurity model*. In the magnetic impurity model, a localized magnetic impurity is embedded into the quantum dot, which then interacts with electrons by exchange interaction. The understanding of the dynamics in this system is important in the context of time-dependent transport experiments in systems with strong hyperfine interaction and diluted magnetic semiconductor quantum dots [33–36]. The latter is regarded as one of the potential implementations of a quantum storage device.

1.3 Exact solution of the non-interacting Anderson impurity model

In this section, we discuss the analytical solution for the time-dependent charge dynamics in the so-called *resonant level model*. The resonant level model resembles the non-interacting Anderson impurity model (AIM) which comprises a single, spin-degenerate level connected to two metallic leads. The single level, denoted as quantum dot in the following, can be occupied by one spin-up electron and one spin-down electron. Coulomb interaction between the particles is neglected, resulting in the quantum dot Hamiltonian

$$H_{dot} = \varepsilon_d \sum_{\sigma=\uparrow,\downarrow} d_\sigma^\dagger d_\sigma, \tag{1.1}$$

with the single-particle energy ε_d and quantum dot creation and annihilation operators $d_\sigma^{(\dagger)}$ for spin $\sigma = \uparrow, \downarrow$. The quantum dot is connected to two leads that are treated as electron reservoirs with different chemical potentials created by applying a bias voltage. The Hamiltonian of the left lead (L) and right lead (R) is given by non-interacting electrons

$$H_{lead} = \sum_{\alpha \in L,R} \sum_k \varepsilon_{\alpha,k} c_{\alpha,k}^\dagger c_{\alpha,k}, \tag{1.2}$$

with the energy $\varepsilon_{\alpha,k}$ of an electron in lead α and with momentum k, and corresponding creation and annihilation operators $c_{\alpha,k}^{(\dagger)}$. Electrons can hop from the leads into the quantum dot and back into the leads. These processes can be described by a Bardeen-type transfer Hamiltonian [37]

$$H_{tunnel} = \sum_{\alpha,k,\sigma} [t_{\alpha,k}(t) c_{\alpha,k,\sigma}^\dagger d_\sigma + H.c.], \tag{1.3}$$

which transforms quantum dot electrons into lead electron and vice versa [38]. The tunnel coupling, $t_{\alpha,k}$, is determined by the overlap of single-electron wavefunctions between the subsystems. Here, we treat the tunnel coupling as a phenomenological, time-dependent coefficient that will be specified later.

The Hamiltonian operator $H = H_{dot} + H_{lead} + H_{tunnel}$ is quadratic in the fermionic operators, which allows for the analytical treatment of the system's time evolution for any selected parameter. In the following, we discuss this solution by means of the non-equilibrium Green's function (GF) formalism. For technical details on the Green's function technique we refer to the literature, e.g. [39,40]. The non-equilibrium approach, also known as Kadanoff-Baym-Keldysh technique, is an extension of the equilibrium GF

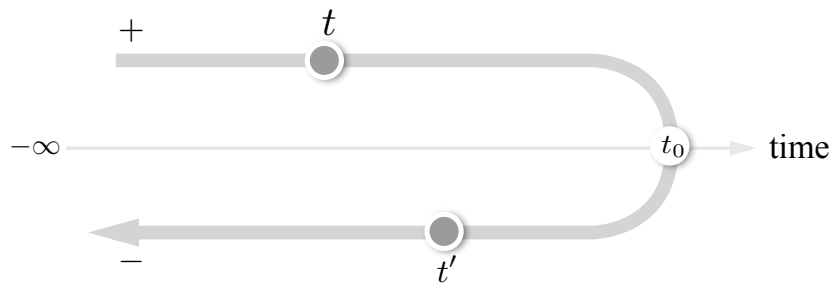

Figure 1.1: The Schwinger-Keldysh contour consists of two branches, an upper branch running from $t = -\infty$ to time $t = t_0$ and a lower branch returning from $t = t_0$ to $t = -\infty$. Calculation of quantities of interest like the occupation or current at time $t = t_0$ involve Green's functions whose two time arguments, t and t', are propagated along both branches of the Keldysh contour.

formalism. However, while the equilibrium theory relies on the property of the system to return to its equilibrium state at $t \to \infty$, irreversible effects break the symmetry between $t \to -\infty$ and $t = \infty$ in the non-equilibrium situation. This problem can be circumvented by propagating the system from $t = -\infty$ to the time of measurement $t = t_0$ and then back to $t = -\infty$ [41, 42]. The procedure allows to calculate expectation values of time-dependent operators. This, however, comes at the price of extending the GF formalism to two time branches. The equilibrium Green's function which depends on two times, t and t', is replaced by the 2×2 non-equilibrium Green's function matrix with times located on the two branches of the Schwinger-Keldysh time contour (Fig. 1.1).

In the follwing, the Keldysh formalism is applied to the non-interacting AIM in order to determine the time-dependent occupation $n(t)$ of the single-level quantum dot. The time-dependence is introduced by assuming that the leads and the quantum dot are decoupled in the remote past. Each part of the system is in thermal equilibrium before the coupling between quantum dot and leads is established at a point $t = 0$ in time. The coupling, however, is included as perturbation, for which perturbation theory can be performed analytically in all orders as demonstrated in [43, 44].

We begin by introducing the Green's function matrices for the two parts of the system, quantum dot and leads, assuming they are initially decoupled. The treatment of the quantum dot is particularly easy since, in the absence of Coulomb interaction, spin-up and spin-down particles can be independently considered. In the following, we regard only one spin species and drop the spin index. The Keldysh Green's function comprises four components, the lesser and greater Green's functions, $G_0^<(t,t')$ and $G_0^>(t,t')$, and the time-ordered and anti-time-ordered Greens's functions, $G_0(t,t')$ and $\tilde{G}_0(t,t')$, which

can be condensed into

$$G_0(\tau,\tau') = \begin{cases} G_0^<(t,t') \equiv i\langle d^\dagger(t')d(t)\rangle & \text{if } \tau \in C^+, \tau' \in C^-, \\ G_0^>(t,t') \equiv -i\langle d(t)d^\dagger(t')\rangle & \text{if } \tau \in C^-, \tau' \in C^+, \\ G_0(t,t') \equiv -i\langle T\,[d(t)d^\dagger(t')]\rangle & \text{if } \tau,\tau' \in C^+, \\ \tilde{G}_0(t,t') \equiv -i\langle \tilde{T}\,[d(t)d^\dagger(t')]\rangle & \text{if } \tau,\tau' \in C^-, \end{cases} \tag{1.4}$$

with times τ, τ' living on the two branches C^+ and C^- of the Keldysh contour (cf. Fig. 1.1) and t, t' being the associated real times. The operators T and $\tilde{T}$ are time-ordering and anti-time ordering operators [39, 40]. The expectation values $\langle \ldots \rangle$ are given with respect to the density matrix of the system.

Two initial conditions for the quantum dot can be considered: The quantum dot level is either unoccupied at $t = 0$, $n_{init} = 0$ or occupied by one electron, $n_{init} = 1$. Together with the free time evolution of the quantum dot operators, $d(t) = d(0)\exp(-i\varepsilon_d t)$, the Green's function matrix for the quantum dot is

$$\mathbf{G}_0(t) = \begin{bmatrix} G_0(t) & G_0^<(t) \\ G_0^>(t) & \tilde{G}_0(t) \end{bmatrix} \tag{1.5}$$

$$= \begin{bmatrix} \Theta(t)(n_{init}-1) + \Theta(-t)n_{init} & n_{init} \\ n_{init}-1 & \Theta(t)n_{init} + \Theta(-t)(n_{init}-1)] \end{bmatrix} \times i\exp(-i\varepsilon_d t), \tag{1.6}$$

with the Heaviside step function $\Theta(t)$. Furthermore, the retarded and advanced components are

$$G_0^R(t) = G_0(t) - G_0^<(t) = -i\Theta(t)e^{-i\varepsilon_d t}, \tag{1.7}$$

$$G_0^A(t) = G_0^<(t) - \tilde{G}_0(t) = i\Theta(-t)e^{-i\varepsilon_d t}. \tag{1.8}$$

Similarly, the Green's function matrix can be obtain for the lead electrons. The leads are assumed to form a non-interacting electron gas in equilibrium at temperature T. The corresponding Green's functions of the uncoupled leads are

$$g_{\alpha,k}^<(t,t') = i\langle c_{\alpha,k}^\dagger(t')c_{\alpha,k}(t)\rangle = i f_\alpha(\varepsilon_{\alpha,k})\exp\left[-i\varepsilon_{\alpha,k}(t-t')\right], \tag{1.9}$$

$$g_{\alpha,k}^>(t,t') = -i\langle c_{\alpha,k}(t)c_{\alpha,k}^\dagger(t')\rangle = -i(1-f_\alpha(\varepsilon_{\alpha,k}))\exp\left[-i\varepsilon_{\alpha,k}(t-t')\right], \tag{1.10}$$

$$g_{\alpha,k}^{R/A}(t,t') = \mp i\Theta(\pm t \mp t')\langle\{c_{\alpha,k}(t)c_{\alpha,k}^\dagger(t')\}\rangle = \mp\Theta(\pm t \mp t')\exp\left[-i\varepsilon_{\alpha,k}(t-t')\right], \tag{1.11}$$

with the Fermi function $f_\alpha = [\exp[(E-\mu_\alpha)/k_BT]+1]^{-1}$ and the chemical potential μ_α in lead α.

The analytical solution for the time evolution of system containing the quantum dot that is coupled to the leads can be found for arbitrary time dependencies of the coupling $t_{\alpha,k}(t)$ [43, 45]. Here, we concentrate on the case where the coupling between quantum dot and leads is switched on at $t = 0$, i.e. $t_\alpha(t) = \Theta(t)\, t_\alpha$. The Dyson equation defines the time evolution of the Green's function for the quantum dot coupled to the leads and is given by

$$\mathbf{G}(t,t') = \mathbf{G}_0(t-t') + \int_0^\infty dt_1 \int_0^\infty dt_2 \mathbf{G}_0(t-t_1)\Sigma(t_1-t_2)\mathbf{G}(t_2,t'), \tag{1.12}$$

with the self-energy

$$\mathbf{\Sigma}(t-t') = \sum_{\alpha,k} t_\alpha^* \, \mathbf{g}_{\alpha,k}(t-t')\, t_\alpha. \tag{1.13}$$

This matrix equation is simplified if one is interested only in a specific component, e.g. the retarded Green's function for times $t, t' \geq 0$,

$$G^R(t,t') = G_0^R(t-t') + \int_0^\infty dt_1 \int_0^\infty dt_2 G_0^R(t-t_1)\Sigma^R(t_1-t_2)G^R(t_2,t'). \tag{1.14}$$

Then, the solution for the retarded and advanced Green's functions can be obtained by iteration [43, 45] and are given by

$$G^{R/A}(t-t') = \mp i\Theta(\pm t \mp t') e^{-i\varepsilon_d(t-t')} e^{\mp\Gamma(t-t')}. \tag{1.15}$$

At first sight, $G^<(t,t')$ has a more complicated structure that reads

$$G^<(t,t') = (1+G^R\Sigma^R)G_0^<(1+G^A\Sigma^A) + G^R\Sigma^<G^A, \tag{1.16}$$

where the time convolution is implicitly assumed. The expression, however, can be simplified considerably if an initially unoccupied quantum dot with $n_0 = 0$ is considered,

resulting in $G_0^< = 0$. In this case, the analytical expression for $G^<(t,t')$ is

$$\begin{aligned}
G^<(t,t') &= G^R \Sigma^< G^A, \\
&= i \int_0^\infty dt_1 \int_0^\infty dt_2 G^R(t,t_1) \left[\sum_{\alpha=L,R} \int \frac{d\omega}{2\pi} e^{-i\omega(t_1-t_2)} \Gamma^\alpha f_\alpha(\omega) \right] G^A(t_2,t') \\
&= i \frac{\Gamma}{2\pi} \int d\omega [f_L(\omega) + f_R(\omega)] \int_0^\infty dt_1 \int_0^\infty dt_2 \Theta(t-t_1)\Theta(t'-t_2) \\
&\quad \times e^{-i\omega(t_1-t_2)} e^{-i\varepsilon_d(t-t_1)} e^{-\Gamma(t-t_1)} e^{-i\varepsilon_d(t_2-t')} e^{\Gamma(t_2-t')} \\
&= i \frac{\Gamma}{2\pi} \int d\omega \frac{f_L(\omega) + f_R(\omega)}{\Gamma^2 + (\varepsilon_d - \omega)^2} \\
&\quad \times \left[e^{-i\omega(t-t')} + e^{-\Gamma(t+t')} e^{-i\varepsilon_d(t-t')} \left[1 - e^{(\Gamma + i(\varepsilon_d-\omega))t} - e^{(\Gamma - i(\varepsilon_d-\omega))t'} \right] \right] \qquad (1.17)
\end{aligned}$$

Here, a constant density of states ρ_0 in each metallic lead is assumed (wide flat band limit), which allows to define the effective single-particle tunneling rate $\Gamma^\alpha = \pi |t_\alpha|^2 \rho_0$ and $\Gamma = \Gamma^L + \Gamma^R$.

The last component of the Keldysh Green's function can be obtained by the relation

$$G^R(t,t') - G^A(t,t') = G^>(t,t') - G^<(t,t'). \qquad (1.18)$$

The same procedure can be applied if one assumes an initially occupied quantum dot with $n_0 = 1$. Again, an expression for $G^>(t,t')$ can be simplified due to $G_0^>(t,t') = 0$.

The knowledge of the different components of the Keldysh Green's function allows us to calculate different time-dependent observables like the occupation of the quantum dot or the current through the system. The quantum dot occupation $n(t) = \langle d^\dagger(t) d(t) \rangle$ at time t depends only on one component of the Keldysh Green's function,

$$n(t) = -i G^<(t,t). \qquad (1.19)$$

Using the expressions derived above, the analytical results for the time-dependent quantum dot occupation reads

$$n(t) = \frac{\Gamma}{2\pi} \int d\omega \frac{f_R(\omega) + f_L(\omega)}{\Gamma^2 + (\varepsilon_d - \omega)^2} \left[1 + \exp(-2\Gamma t) - 2\exp(-\Gamma t) \cos((\varepsilon_d - \omega)\, t) \right]. \qquad (1.20)$$

The occupation as a function of time can be rewritten as

$$n(t) = \left(1 + e^{-2\Gamma t}\right) n_{stat} - e^{-\Gamma t}\, n_{trans}, \tag{1.21}$$

which distinguishes between the stationary occupation of the quantum dot, n_{stat}, and a transient part n_{trans}. The stationary occupation is asymptotically approached on a time scale given by Γ and reads

$$n_{stat} \equiv \lim_{t\to\infty} n(t) = \frac{\Gamma}{2\pi} \int d\omega \frac{f_R(\omega) + f_L(\omega)}{\Gamma^2 + (\varepsilon_d - \omega)^2}, \tag{1.22}$$

with $\mu_L = -\mu_R = V/2$. The integration can be performed analytically and yields the following expressions at zero and finite temperature. The stationary occupation at finite temperature is

$$n_{stat} = \frac{1}{2} + \frac{1}{2\pi} \sum_{\alpha=L,R} \mathrm{Im}\Psi\left(\frac{1}{2} + i\frac{\mu_\alpha - \varepsilon_d + i\Gamma}{2\pi\, k_B T}\right), \tag{1.23}$$

with the Digamma function Ψ [46]. In the zero-temperature limit, the stationary occupation is given by

$$n_{stat} = \frac{1}{2} + \frac{1}{2\pi} \sum_{\alpha=L,R} \arctan\left(\frac{\mu_\alpha - \varepsilon_d}{\Gamma/2}\right). \tag{1.24}$$

Important properties of the stationary solution can be inferred from these equations. The filling of the quantum dot depends on the available states in the leads defined by the Fermi function and by the energy of the level in the quantum dot. The density of states in the dot are not δ-distributed, but adopt a Lorentzian line shape with a resonance at the single-electron energy and a width of 2Γ due to the tunnel coupling to the leads (Fig. 1.2a).

The Lorentzian broadening is reflected in the stationary occupation n_{stat} when applying a bias at low temperatures $k_B T \lesssim \Gamma$ (Fig. 1.2b). At high temperatures $k_B T \gg \Gamma$, the tunneling-induced broadening is covered by a temperature broadening. The time-dependent occupation also reveals that the stationary occupation is reached at a time scale given by Γ. Before the stationary state is reached, the transient part

$$n_{trans}(t) = \frac{\Gamma}{\pi} \int d\omega \frac{f_R(\omega) + f_L(\omega)}{\Gamma^2 + (\varepsilon_d - \omega)^2} \cos[(\varepsilon_d - \omega)\, t] \tag{1.25}$$

contributes to the time-dependent occupation. The transient term decays on a time-scale given by Γ and its integrand shows oscillatory behavior, which is induced by the coherent tunneling of electrons.

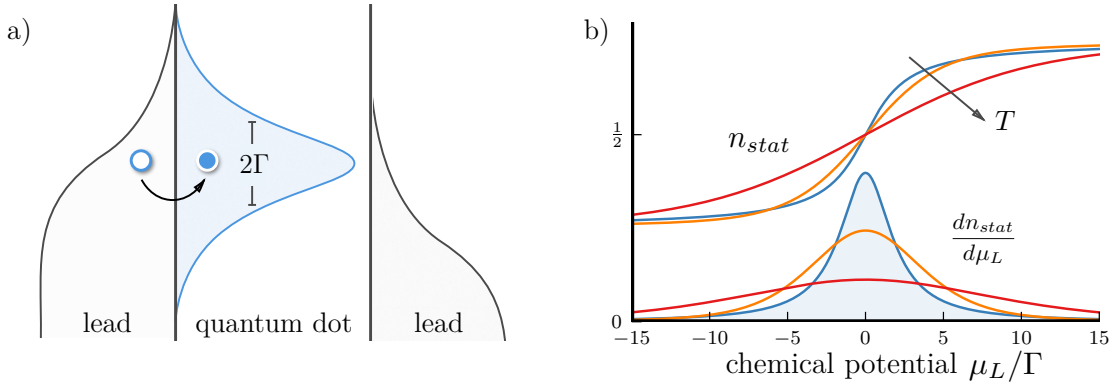

Figure 1.2: a) Schematic depiction of the density of states in the quantum dot and the leads. The distribution function in the leads is given by the Fermi function. The tunnel coupling of the quantum dot to the leads induces a Lorentzian broadening of the quantum dot level of width 2Γ. b) The stationary occupation n_{stat} and its derivative with respect to the change of the chemical potential μ_L in the left lead. The other parameters are $\mu_R = \varepsilon_d = 0$. The occupation versus the chemical potential is shown for different temperatures $k_BT = 0$ (blue), 2Γ (orange), 5Γ (red). The tunneling-induced Lorentzian broadening of width Γ is clearly observable in $dn/d\mu_L$ (5× magnification) for low temperatures ($k_BT \ll \Gamma$).

In Fig. 1.3, we show the time evolution of the occupation $n(t)$ for different quantum dot energies ε_0 and for bias voltage $V = 0$. If the quantum dot energy is well below the Fermi edge of the leads, the occupation monotonically approaches the steady state given by an occupied quantum dot $n_{stat} = 1$. For $\varepsilon_d = \mu_L = \mu_R$, a half filling of the quantum dot is obtained in steady state. Up to this point, the approach of the steady state is dominated by a exponential filling of the quantum dot. For quantum dot energies that lie above the Fermi energies of the leads, however, an overshooting is observed, accompanied by small oscillations. These oscillations arise from the transient part and have a period of $(\varepsilon_d - \mu_{leads})^{-1}$, which corresponds to the energetic distance of the quantum dot level from the Fermi edge in the leads.

Further observations can be made when considering the bias dependence of the quantum dot occupation. We assume a symmetrically applied bias voltage, V, that shifts the chemical potentials in the leads, $\mu_L = -\mu_R = V/2$, and a quantum dot level located at $\varepsilon_d = 0$. For these parameters, the stationary occupation given by $n_{stat} = 1/2$ is bias independent. If the bias is sufficiently high, $eV \gg \Gamma$, the time-dependent occupation

$$n(t) = (1 - e^{-\Gamma t})\, n_{stat}, \tag{1.26}$$

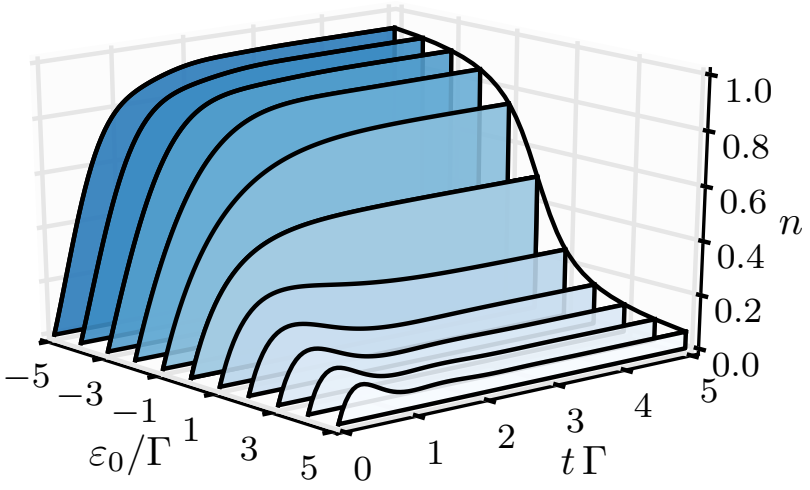

Figure 1.3: Exact time-dependent occupation probability versus the position of the level energy ε_0 for a non-interacting quantum dot coupled to two leads. For a bias voltage $V = 0$, the time-dependent occupation for a quantum dot level below the Fermi energy of the leads exponentially increases in first order. For a quantum dot level above the Fermi energy, small, $(\varepsilon_0 - \mu_{leads})^{-1}$-periodic oscillations are noticeable.

reduces to an exponential law that can also be obtained by a second-order perturbation expansion in the tunneling coupling shown in the next section. In fact, a master equation approach in second order of the tunneling coupling is only valid in the regime of large bias and high temperatures, $eV; k_BT \gg \Gamma$. For bias voltages and temperatures in the order of the tunnel coupling or smaller, expansions in the tunneling coupling are invalid.

1.4 Quantum master equation approach

In the regime of weak tunnel coupling between the quantum dot and the leads, electrons in the two subsystems are efficiently decoupled by the tunnel barrier. Interactions between electrons in the subsystems other than long-range Coulomb interactions are negligible and collective effects like the Kondo effect are of minor importance. In this regime, the dynamics are mainly determined by the spectral properties of the quantum dot and a master equation approach is applicable. The master equation is an equation of motion for the reduced density operator of a subsystem. Here, the subsystem is given by the quantum dot. However, the approach can also be conducted for a subsystem given by the leads [47, 48]. The starting point of the derivation of the master equation

is the von *Neumann equation*

$$\frac{d}{dt}\rho = -i\,[H, \rho], \tag{1.27}$$

for the full system described by the Hamiltonian $H = H_{dot} + H_{leads} + H_{tunnel}$. Typically, however, one is only interested in the dynamics of the reduced density operator for the quantum dot

$$\rho_{dot}(t) = \mathrm{Tr}_{leads}\,[\,\rho(t)], \tag{1.28}$$

with the trace performed over the many-electron states of the leads. The quantum master equation approach represents the dynamics of the reduced density operator of the quantum dot under the assumption that H_{tunnel} can be treated perturbatively.

In a first step, the operators are transformed into the interaction picture subject to the time evolution of the uncoupled system

$$\mathcal{O}(t) = \exp\left[i(H_{dot} + H_{leads})t\right]\,\mathcal{O}\,\exp\left[-i(H_{dot} + H_{leads})t\right]. \tag{1.29}$$

In the interaction picture, the equation of motion for the density operator reads

$$\frac{d}{dt}\rho(t) = -i\,[H_{tunnel}(t), \rho(t)]. \tag{1.30}$$

Formally integrating the equation of motion gives

$$\rho(t) = \rho(t_0) - i\int_0^t dt'\,[H_{tunnel}(t'), \rho(t')], \tag{1.31}$$

and by reinserting this result into the equation of motion (Eq. 1.30) we obtain

$$\frac{d}{dt}\rho(t) = -i\,[H_{tunnel}(t), \rho(0)] - \int_0^t dt'\,[H_{tunnel}(t), [H_{tunnel}(t'), \rho(t')]]. \tag{1.32}$$

Higher orders can be included by continuing the iterations [49].

The initial condition for the density operator is defined as

$$\rho(t = 0) = \rho_{dot}(t = 0) \otimes \rho_{leads}(t = 0), \tag{1.33}$$

where the leads are in thermal equilibrium, $\rho_{leads}(t = 0) = \exp(-H_{leads}/k_BT)$, with temperature T in the leads. The quantum dot and leads are decoupled for $t < 0$ and the interaction H_{tunnel} is switched on at time $t = 0$. Since H_{tunnel} changes the particle

number in the quantum dot and the leads, the first term in Eq. (1.32) vanishes,

$$\mathrm{Tr}_{leads}\left[H_{tunnel}(t)\,\rho(0)\right] = 0. \tag{1.34}$$

Then, the time evolution of the reduced density matrix of the quantum dot is given by

$$\frac{d}{dt}\,\rho_{dot}(t) = -\int_0^t dt'\,\mathrm{Tr}_{leads}\left[H_{tunnel}(t),[H_{tunnel}(t'),\rho(t')]\right]. \tag{1.35}$$

Up to this point, only the assumption of weak tunnel coupling has been made. Further simplifications can be achieved by assuming that the tunneling has a negligible effect on the leads represented by large electron reservoirs. The leads will stay in equilibrium at all times, which gives $\rho_{leads}(t) \equiv \rho_{leads}(0) \equiv \rho_{leads}$ and $\rho(t) = \rho_{dot}(t) \otimes \rho_{leads}$.

With this assumption, the master equation in the non-local time version reads

$$\frac{d}{dt}\,\rho_{dot}(t) = -\int_0^t dt'\,\mathrm{Tr}_{leads}\left[H_{tunnel}(t),[H_{tunnel}(t'),\rho_{dot}(t')\otimes\rho_{leads}]\right]. \tag{1.36}$$

The solution of the non-local master equation demands for propagating the density matrix and its full history. If the lead correlation functions, however, rapidly decay on the time scale of the dynamics in the quantum dot, they can be replaced by δ-functions in time which allows to substitute $\rho_{dot}(t')$ by $\rho_{dot}(t)$. This replacement means that the change of the density matrix at time t only depends on its value at time t and not on the history of the density matrix. This approximation is also known as Markov approximation. The Markov assumption, furthermore, allows to shift the initial time to $t = -\infty$ if t is large compared to the correlation time in the leads.

With the shift of the initial time, the time-local master equation in the Schrödinger picture is

$$\begin{aligned}\frac{d}{dt}\rho_{dot}(t) = -i\left[H_{dot},\rho_{dot}(t)\right] - \int_0^\infty dt' \\ \times \mathrm{Tr}_{leads}[H_{tunnel},[e^{i(H_{dot}+H_{leads})t'}H_{tunnel}e^{i(H_{dot}+H_{leads})t'},\rho_{dot}(t)\otimes\rho_{leads}]].\end{aligned} \tag{1.37}$$

The first term describes the free time evolution of the quantum dot and the second term incorporates the coupling to the leads in second order. Restricting to the second order in tunnel coupling corresponds to the sequential tunneling approximation in which tunneling events through the left barrier are independent of tunneling events through the right barrier. Thus, the effect of an electron coherently tunneling through both barriers is neglected. As a result, the sequential tunneling approximation fails to describe the

finite conductance in the Coulomb blockade regime [50]. In fact, the approach is only appropriate if the temperature broadening in the leads is larger than the tunneling-induced level broadening, i.e. $k_B T \gg \Gamma$, or if a large bias voltage is applied $eV \gg \Gamma$ [51].

The local master equation (Eq. 1.37) derived above is an equation of motion for the reduced density operator of the quantum dot. However, strong interactions of the quantum dot electrons with the environment can lead to a short decoherence time T_2. In this regime, the off-diagonal elements of ρ_{dot} decay exponentially with $1/T_2$ and thus can be neglected. When the off-diagonal elements rapidly decay, the system can be described only by the probabilities to occupy the quantum dot many-electron states $|n\rangle$ given by the diagonal elements $P_n \equiv \langle n|\rho_{dot}|n\rangle$. The equation of motion for the occupation probabilities is given by the Markovian master equation for the diagonal density matrix elements,

$$\frac{d}{dt}P_n = 2\pi \sum_{i,j} \sum_{m} |\langle i|\langle m|H_{tunnel}|m\rangle|j\rangle|^2 \left(W_j\, P_m - W_i\, P_n\right) \delta(E_m - E_n - \varepsilon_i + \varepsilon_j), \qquad (1.38)$$

with the quantum dot energies E_n of the many-electron state $|n\rangle$, the lead density matrix elements $W_i = \langle i|\rho_{leads}|i\rangle$ for lead states $|i\rangle$ and their associated energies ε_i. By rearranging Eq. (1.38), we obtain the well-known rate equation

$$\frac{d}{dt}P_n = \sum_{m} \left(W_{m\to n} P_m - W_{n\to m} P_n\right) \qquad (1.39)$$

with the transition rates

$$W_{m\to n} = 2\pi \sum_{ij} W_j\, |\langle i|\langle n|H_{tunnel}|m\rangle|j\rangle|^2 \delta(E_m - E_n - \varepsilon_i + \varepsilon_j). \qquad (1.40)$$

The rate equation consists of two parts describing transitions from states $|m\rangle$ to $|n\rangle$ and transitions out of state $|n\rangle$. Furthermore, the conservation of probability is ensured by the structure of the rate equation, i.e. $\sum_n P_n(t) = 1$ for all times if $\sum_n P_n(t=0) = 1$.

Expressions for the tunneling rates can be derived by explicitly inserting H_{tunnel}:

$$W_{m\to n} = 2\pi \sum_{ij} \sum_{\alpha,\beta,k,k',\sigma,\sigma'} t^*_{\alpha,k} t_{\beta,k'} \langle i|c_{\alpha,k,\sigma}|j\rangle\langle j|c^\dagger_{\beta,k',\sigma'}|i\rangle \times \langle n|d^\dagger_\sigma|m\rangle\langle m|d_{\sigma'}|n\rangle \qquad (1.41)$$

$$\times\, \delta(E_m - E_n - \varepsilon_i + \varepsilon_j). \qquad (1.42)$$

The leads are given by non-interacting electron baths in equilibrium with the lead elec-

tron correlation functions

$$2\pi \sum_{\alpha,\beta,k,k',\sigma,\sigma'} t^*_{\alpha,k} t_{\beta,k'} \langle i|c_{\alpha,k,\sigma}|j\rangle\langle j|c^\dagger_{\beta,k',\sigma'}|i\rangle = \Gamma\, f(\varepsilon_i - \varepsilon_j)\, \delta_{\sigma,\sigma'}. \tag{1.43}$$

By inserting this expression into Eq. (1.44), rates are obtained that resemble Fermi's Golden Rule

$$W_{m\to n} = \Gamma \sum_{ij} \sum_{\sigma} \langle n|d^\dagger_\sigma|m\rangle\langle m|d_\sigma|n\rangle\, f(\varepsilon_i - \varepsilon_j)\, \delta(E_m - E_n - \varepsilon_i + \varepsilon_j). \tag{1.44}$$

The δ-function ensures energy conservation during the transition from the initial to the final state. If an electron initially located in the leads tunnels into the quantum dot, a transition between lead states $i \to j$ and quantum dot states $m \to n$ can be induced. Energy conservation requires

$$\varepsilon_i - \varepsilon_j = E_m - E_n = \varepsilon_{mn}, \tag{1.45}$$

with the quasi single-particle level ε_{mn} in the quantum dot that is associated with the transition from an N-state state to an $(N+1)$-electron state. The energy ε_{mn} defines the resonance energy for transport and generally does not correspond to any single-electron orbital. In the previous section, the regime of strong tunnel coupling revealed tunneling-induced broadening of the quasi levels. In contrast, the present weak tunnel coupling allows tunneling into the quantum dot only at discrete energies. Each available transition gives rise to a transport channel at energy ε_{mn}. Transport can only take place if a lead electron with sufficient energy is available, expressed by the Pauli blocking factor $f(E_m - E_n)$ (Fig. 1.4). Finally, summation over the lead states yields the rates in sequential tunneling approximation

$$W^+_{m\to n} = \Gamma \sum_{\sigma} |\langle n|d^\dagger_\sigma|m\rangle|^2\, f(E_m - E_n), \tag{1.46}$$

$$W^-_{n\to m} = \Gamma \sum_{\sigma} |\langle n|d_\sigma|m\rangle|^2\, (1 - f(E_m - E_n)), \tag{1.47}$$

and $W_{n\to m} = W^+_{n\to m} + W^-_{n\to m}$. The current in the weak tunnel coupling approximation can be obtained with the knowledge of the probabilities

$$I = -e \sum_{n\neq m} (P_m W^+_{m\to n} - P_n W^-_{n\to m}). \tag{1.48}$$

In this Golden Rule approximation, only transitions between quantum dot states are

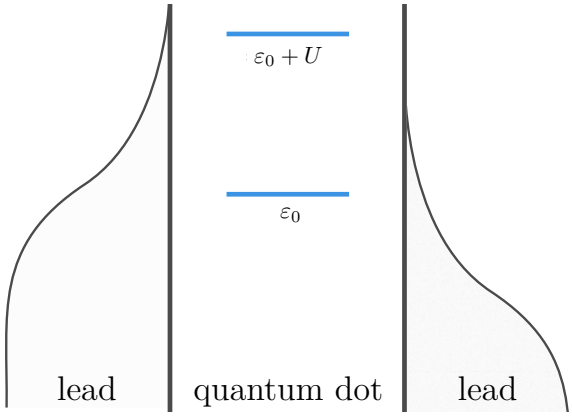

Figure 1.4: In the master equation approach, the distribution function of leads is given by the Fermi function. Transport can take place whenever states in the leads are available at the quasi single-particle levels ε_{mn}. The quasi single-particle levels are given by the energy difference between N to $N \pm 1$-particle changes.

considered that differ by a single electron. Furthermore, it is only applicable for energies and temperatures larger than the tunnel coupling, $|E_m - E_n|$; $|eV|$; $k_B T \gg \Gamma$.

Finally, we summarize the assumption that result in the present form of the master equation:

- Systems are separated, $\rho(t = 0) = \rho_{dot}(t = 0) \otimes \rho_{leads}(t = 0)$, for times $t < 0$
- Electron reservoirs are in equilibrium for all times, $\rho(t) = \rho_{dot}(t) \otimes \rho_{leads}$
- Time-local (Markov) approximation, $\rho_{dot}(t') \to \rho_{dot}(t)$
- Fast decoherence leads to rapidly decaying off-diagonal elements of the dot density matrix, $P_n \equiv \langle n|\rho_{dot}|n\rangle$

Although many assumptions are involved deriving the master equation it has been proven to adequately describe many experimental situations and, at the same time, it offers an intuitive explanation of involved processes. In the next chapter, we employ the master equation approach for the analysis of the dynamics in a quantum dot weakly tunnel coupled to a two-dimensional electron gas.

This page intentionally left blank.

2 Charging and Relaxation in Open Quantum Dots

2.1 Experimental motivation

Semiconductor quantum dots (QDs) are nanoscale objects that incorporate charge carriers confined in all three spatial dimensions. QDs exhibit a wide range of physical phenomena connected to their atom-like electronic structure. Furthermore, QDs are regarded as promising building blocks for quantum or classical information. The application of these structures as future information devices, however, requires controlled preparation and read out of electronic states with charge and spin degrees of freedom. In this respect, distinct advantages have been made by using optical methods for excitation and detection of self-assembled QDs [52–54]. While optical experiments allow for comprehensive probing of the electronic structure of quantum dots, the implementation in highly integrated devices may be difficult. An all-electrical approach is preferable in order to prepare and detect electronic states in QDs and has been demonstrated on lithographically defined QDs [55–58] at milli-Kelvin temperature. Recent experimental advantages made it possible to probe self-assembled InAs QDs at liquid helium temperature (~ 4.2 Kelvin). In the following, we discuss two experimental approaches to the time-dependent characterization of quantum dot states.

The minimal setup to electrically prepare and probe (excited) many-particle states in a quantum dot consists of the following parts:

- a reservoir providing electrons,
- a high-sensitivity detector to read out the time-dependent state of the QDs,
- an adjustable tunnel coupling between reservoir and detector.

One example of such an experimentally realized setup is a lithographically defined system consisting of three parts [57, 59]: a single, electrostatically defined quantum dot coupled to electron reservoirs and a quantum point contact (schematically depicted in Fig 2.1a). The zero dimensional quantum dot is created by a laterally modulated two-dimensional electron gas (2DEG). The quantum dot is tunnel coupled to electron reservoirs, and the tunnel coupling can be electrically adjusted to control the electron

flow into and out of the QD. In this setup, the time-dependent detection of single-electron transfers, which induces tiny currents of the order of 10^{-19} A, poses a major challenge to the experiment due to the limited resolution available. However, the electron flow through the quantum dot can be indirectly measured by capacitively coupling the quantum dot to a quantum point contact (QPC) that acts as a highly sensitive charge detector. When the quantum dot is charged with electrons, the potential of the QPC is changed, which decreases the width of the 1D channel and can be sensed by the change in the current through the QPC [55, 59].

Recently, a different time-resolved spectroscopic method has been realized using epitaxially grown quantum dots [9]. This approach is schematically depicted in Fig. 2.1b. In contrast to lithographically defined quantum dots, epitaxially grown quantum dots have distinct advantages for their potential application. Their smaller size leads to a stronger confinement, which can create an energy spacing between single-particle levels of up to 80 meV in the quantum dots [60, 61]. The large energy spacing allows for an application at room temperature. Furthermore, epitaxially grown quantum dots can be produced without the need of time consuming lithography.

This chapter deals with the theoretical treatment of the experiments on epitaxially grown quantum dots [9]. To set the scene, a short overview with some details on the experimental techniques is given. The two main components of the experimental setup are an *ensemble* of epitaxially grown quantum dots and a 2DEG that are *vertically*

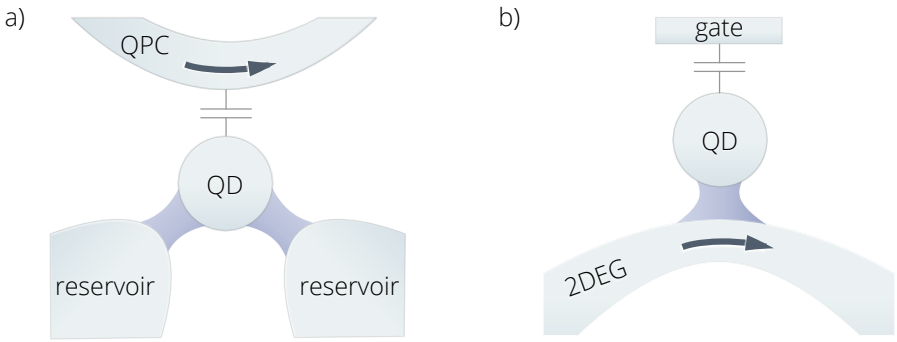

Figure 2.1: Two different setups to prepare and probe many-particle states in a quantum dot. In (a), an electrostatically defined quantum dot (QD) is coupled through adjustable tunnel barriers to electron reservoirs. The current through a nearby quantum point contact (QPC), capacitively coupled to the quantum dot, can be measured to detect the charge state of the quantum dot. In (b), electrons can tunnel from a two-dimensional electron gas (2DEG) to the quantum dot (QD). The change in the current through the 2DEG is used to determine the charging of the QD. The potential in the QD can be adjusted by a capacitively coupled gate electrode.

tunnel coupled. Measuring the time-dependent conductance of the 2DEG will provide information about tunnel dynamics between the two systems.

The experiment is performed in two steps: the initialization and the probing (Fig. 2.2). In a first step, the potential in the quantum dots is shifted by applying a voltage between the gate electrode and the 2DEG. By shifting the energy levels in the quantum dots compared to the Fermi level in the 2DEG, a defined equilibrium many-electron state can be prepared in the quantum dots. If the Fermi energy in the 2DEG is selected to be below all energy states in the QDs, then the electrons in the QDs are depleted resulting in a neutral charge state. The step in which the equilibrium configuration of electrons in the QDs is prepared represents the initialization for times $t < 0$.

At time $t = 0$, the gate voltage is abruptly changed, i.e. the time needed to change the gate voltage is shorter than the tunneling time of electrons between the 2DEG and the QDs. The actual tunneling time in the experiments by Marquardt et. al [9] is in the order of milliseconds. The change of the gate voltage by ΔV_G creates a non-equilibrium between the chemical potentials in the 2DEG and the QDs. If the gate potential shifts the energies in the QDs below the Fermi energy in the 2DEG, electrons can tunnel from the 2DEG into (excited) states in the QDs. This step represents the probing of the quantum dot states as will be explained below.

In this setup, the 2DEG acts as an electron source as well as a highly sensitive, time-resolved detector. The charging of the quantum dots can be controlled by the

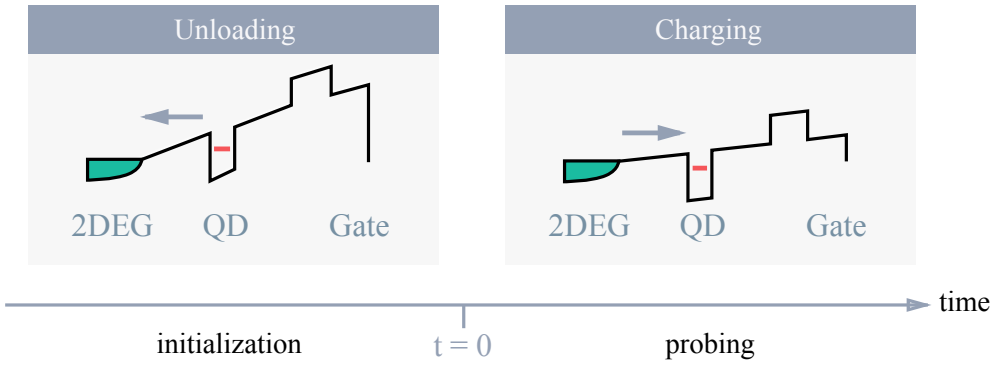

Figure 2.2: Schematic depiction of the conduction band profile of the experimental setup consisting of an ensemble of quantum dots (QD) and a two-dimensional electron gas (2DEG) separated by a tunnel barrier. During *initialization*, the applied gate voltage shifts the energies in the QD above the Fermi energy in the 2DEG and electrons flow from the QDs into the 2DEG (arrows point into the direction of the electron flow). At time $t = 0$, the applied gate voltage shifts the QD energy levels below the 2DEG Fermi energy (*probing* step).

gate electrode, which enables or blocks the electron transfer from the 2DEG into the QDs. Concurrently, the time-resolved carrier concentration in the 2DEG, $n_{2d}(t)$, can be gathered by recording the current through the 2DEG

$$I_{2d}(t) \propto n_{2d}(t)\,\mu_{2d}(t), \tag{2.1}$$

with $\mu_{2d}(t)$ being the electron mobility. After the initialization step, the QDs and 2DEG relax to equilibrium, and the measured current is defined by the carrier density n_{2d} in the 2DEG and their mobility μ_{2d}. When the gate voltage is abruptly changed at $t = 0$, electrons start to tunnel from the 2DEG into the ensemble of quantum dots and the time-dependent current $I_{2d}(t)$ decreases considerably. Two sources for the decay of the current can be identified [24]. The electrons tunneling into the QDs deplete the 2DEG and are no longer available for transport, thus, reducing the current (cf. Eq. 2.1). The proportionality of the change of charge carriers in the QDs, n_{QD}, and in the 2DEG, n_{2d}, can be estimated by the lever arm law [62, 63]

$$\Delta n_{QD} \propto (1 - \frac{1}{\lambda})\,\Delta n_{2d}, \tag{2.2}$$

where λ is the lever arm. Additionally, the electrons in the quantum dots act as Coulomb scatterers and have an impact on the mobility μ_{2d} in the 2DEG. Marquardt et. al [24] have shown that in the actual experimental measurements the change in the number of carriers and the change in the electron mobility result in contributions of the same order.

The experimental spectrum of the time-resolved charging of the quantum dots is depicted in Fig. 2.3. The surface plot shows the change in current through the 2DEG, $\Delta I_{2d}(t) = I_{2d}(0) - I_{2d}(t)$, differentiated with respect to the gate voltage, $d\Delta I_{2d}/dV_G$, as a function of time and for different gate voltages. Distinct peaks evolving in time become visible, corresponding to the charging of the quantum dots with different numbers of electrons. Each additional peak emerging as the gate voltage is increased, indicates that on average an additional electron is tunneled into each of the quantum dots due to the relation $d\Delta I_{2d}/dV_G \propto dn_{QD}/dV_G$.

In *Nat. Commun.* 2:209 (2011) [9], we have specified the many-body states in the quantum dots that participate in the measured relaxation dynamics. In the following, we will show how the charging dynamics can be derived by a master equation and how intrinsic and extrinsic mechanisms determine this dynamics.

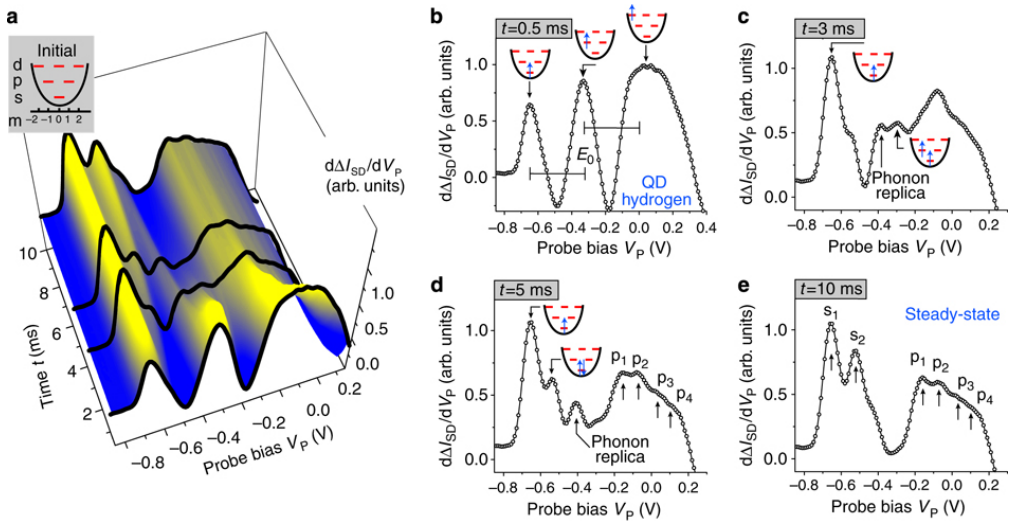

Figure 2.3: Surface plot (a) of the experimentally measured signal $d\Delta I_{2d}/dV_G$ as a function of time and gate voltage (here denoted as probe bias V_p). The initially empty quantum dots are charged by changing the gate voltage at $t = 0$. Different many-electron states can be identified in traces taken at different times (b–e). At $t = 10$ ms, an equilibrium has been reached with peaks indicating the $1-6$ electron ground states (denoted as $s1, s2$ and $p3-p6$). Taken from Marquardt et al., Nat. Commun. 2:209 doi: 10.1038/1205 (2011), licensed under CC BY-NC-SA 3.0 [64].

2.2 Time evolution in quantum dots

Quantum dots are low-dimensional systems in the size of nanometers with a quantum confinement in all three spatial dimensions. Widely used methods to build QDs are based on the processing of a semiconductor heterostructure which contains a two-dimensional electron gas. The movement of the conduction electrons is restricted by either electrostatic gates, by etching or by applying special growing techniques in their fabrication. While various methods exist to fabricate QDs, their electronic structure can often be successfully described on the basis of the effective mass approximation. In this approach, the conduction electrons in the QD are treated as a separate electron system, and effects of the interaction with valence and core electrons as well as the effect of the lattice structure are taken into account effectively. The effective, separate system is constructed by assigning an effective mass m^* to the electrons and describing their interaction by a screened Coulomb potential with the static dielectric constant ε of the underlying semiconductor. For small momenta and low temperatures, typical values are $m^* = 0.067\, m_e$ for GaAs and $m^* = 0.026\, m_e$ for InAs [65–67].

The Hamiltonian of N interacting electrons in a quantum dot is given by

$$H_{QD} = \sum_{i}^{N} H_i^{(1)} + \sum_{i<j}^{N} \frac{e^2}{\varepsilon |\vec{r}_i - \vec{r}_j|}, \tag{2.3}$$

where the electron motion is assumed to be confined in the (x, y) plane and ε denotes the dielectric constant of the bulk material. Usually, the precise form of the lateral confinement potential in quantum dots is not known. However, the model of an isotropic parabolic potential given by

$$H_i^{(1)} = \frac{|\vec{p}_i|^2}{2m^*} + \frac{m^* \omega_0^2 |\vec{r}_i|^2}{2}. \tag{2.4}$$

has been very successfully applied to describe the low-energy spectrum of quantum dots [68]. The strength of the confinement potential is characterized by $\hbar\omega_0$ and the effective mass is given by m^*. Position and momentum of the particles in the (x, y) plane are denoted by $\vec{r}_i$ and $\vec{p}_i$. The energy spectrum and the few-electron eigenstates of the Hamiltonian H_{QD} in Eq. (2.3) are determined by exact diagonalization including correlation effects.

In order to calculate the charging dynamics of a quantum dot, the time-dependent probabilities P_β of occupying the many-electron states $|\beta\rangle$ are determined by a master equation. The master equation approach is justified by the long tunneling times relevant for the experiment (milliseconds), meaning that the system is in a weak coupling regime in which the electrons in the quantum dot efficiently decouple from the electrons in the 2DEG. Electrons sequentially tunnel between the systems, and the charging times are mainly determined by the bare single-particle tunneling time as well as spectral properties of the quantum dot.

The experimental setup is modeled by the transport Hamiltonian

$$H_{trans} = H_{QD} + H_{2d} + H_{tunnel}, \tag{2.5}$$

where H_{tunnel} describes the electron tunneling between the 2DEG (H_{2d}) and the QD (H_{QD}, cf. Eq. 2.3). The electrons in the reservoir are considered to represent a nearly free electron gas described by the Hamiltonian

$$H_{2d} = \sum_{\vec{k}} \varepsilon_{\vec{k}}\, c_{\vec{k}}^\dagger c_{\vec{k}}, \tag{2.6}$$

where $c_{\vec{k}}^{(\dagger)}$ is the annihilation (creation) operator for an electron with energy $\varepsilon_{\vec{k}}$ in the

2DEG. The treatment of the 2DEG electrons as nearly free is justified by their relatively high density, which leads to an effective screening of the Coulomb interaction between electrons. The quantum dot Hamiltonian is given by H_{QD} (in Eq. 2.3). The quantum dot energies, however, are shifted by an electrostatic potential eV_G due to an externally applied gate voltage $V_G^{(ext)}$. The relation between the gate bias and the electrostatic potential imposed on the quantum dot can be described by the lever arm model $V_G \approx \lambda^{-1} V_G^{(ext)}$, with the lever arm λ depending on the experimental geometry [63]. In the following, we use the effective electrostatic potential, resulting in the following QD energies

$$E_\alpha = E_\alpha^0 - N\, eV_G, \tag{2.7}$$

where E_α^0 are the bare quantum dot energies obtained from Eq. (2.4) and N is the number of electrons in state α. Similarly, an electrostatic coupling to the 2DEG can be modeled, which is assumed to be constant throughout the calculations.

The quantum dot and the 2DEG are coupled by the tunneling Hamiltonian

$$H_{tunnel} = \sum_{a,b,\vec{k}} t_{\vec{k},a}\, c_{\vec{k}}^\dagger\, d_a + t_{\vec{k},b}^*\, c_{\vec{k}}\, d_a^\dagger, \tag{2.8}$$

which transfers electrons between the 2DEG and the QD by creating a quantum dot electron in the single-particle state $|a\rangle$ and simultaneously annihilates an electron in the 2DEG, and vice versa. The tunneling matrix elements $t_{\vec{k},a}$ are given by the overlap of electron wave functions in the quantum dot and in the 2DEG, which depends on the properties of the tunnel barrier. An exact model of the tunnel barrier is difficult to obtain since electrons in the 2DEG screen the applied electrostatic potentials, and the barrier potential is disturbed by impurities. In the following, however, the focus will lie on the impact of spectral properties of the quantum dot on charging time scales and thus a phenomenological transmission coefficient will be used.

Following Fermi's Golden Rule [69], rates can be obtained to describe the charging dynamics of a quantum dot when coupled to a 2DEG in a master equation approach. Within the sequential tunneling approximation, the time-dependent probabilities P_β of finding the quantum dot in a few-electron eigenstate $|\beta\rangle$ can be obtained for different times t by solving

$$\frac{d}{dt} P_\beta = \sum_{\alpha \neq \beta} \Gamma_{\alpha\to\beta} P_\alpha - \Gamma_{\beta\to\alpha} P_\beta, \tag{2.9}$$

where P_α is the occupation probability of the many-electron state $|\alpha\rangle$ in the quantum dot. Tunneling into and out of the quantum dot changes the occupation probabilities

according to

$$\begin{aligned}\Gamma_{\alpha\to\beta} &= \Gamma_0 \sum_a |\langle\beta|d_a^\dagger|\alpha\rangle|^2 \, f(E_\beta - E_\alpha - eV_G) \\ &\quad + \Gamma_0 \sum_a |\langle\beta|d_a|\alpha\rangle|^2 \, (1 - f(E_\alpha - E_\beta + eV_G)),\end{aligned} \tag{2.10}$$

where Γ_0 is the bare single-electron tunneling rate given by $\Gamma_0 = \frac{2\pi}{\hbar} \sum_{\tilde{k}} t_{\tilde{k}}^* t_{\tilde{k}} \delta(\varepsilon - \varepsilon_k)$. Transitions between quantum dot states are proportional to the Fermi function f in the 2DEG and to the spectral weights $|\langle\beta|d_a^{(\dagger)}|\alpha\rangle|^2$. In the absence of correlations, the spectral weights result in a factor that is equal to the degeneracy of available eigenstates at a specific energy. In the present approach, the information on the density of states in the back contact, the transmission of the barrier, and the overlap between electrons in the quantum dot and the 2DEG is encoded in the rate Γ_0 [70, 71]. Because of the multitude of parameters determining the specific dependence of Γ_0 and in order to keep the model simple, a constant tunneling probability is assumed in the following. Furthermore, the tunneling rates in the present form do not incorporate the band bottom of the two-dimensional electron gas. Electrons can only tunnel into quantum dot states that are energetically located between the band bottom E_0 and the Fermi energy E_F in the 2DEG, which is determined by the carrier density $n_{2D} = (E_F - E_0)\, m^*/(\pi\hbar^2)$ [72]. However, if the conduction band width is large compared to the available quantum dot energies, the present transition rates are valid in a first-order approximation.

2.2.1 Time evolution of a single-level quantum dot

Preceding the results for a many-level quantum, a toy model of a quantum dot with a single electronic level is discussed in order to highlight relationships determining the charging times. A QD Hamiltonian

$$H_{QD} = (\varepsilon_d - eV)(n_\uparrow + n_\downarrow) + U n_\uparrow n_\downarrow, \tag{2.11}$$

describes a spin-degenerate level of energy ε_d that can be occupied by two electrons at most, interacting through a Coulomb term with strength U. The eigenstates of this system are given by an emptry quantum dot $|0\rangle$, a single-electron with spin up $|\uparrow\rangle$ or spin down $|\downarrow\rangle$, and a doubly occupied quantum dot $|\uparrow\downarrow\rangle$. The time evolution of the probabilities P_α of occupying the these states of the dot is given by the rate equation

$\dot{P} = WP$ with the rates

$$W = \Gamma_0 \begin{pmatrix} -2f^+(\varepsilon) & f^-(\varepsilon) & f^-(\varepsilon) & 0 \\ f^+(\varepsilon) & -f^-(\varepsilon) - f^+(\varepsilon+U) & 0 & f^-(\varepsilon+U) \\ f^+(\varepsilon) & 0 & -f^-(\varepsilon) - f^+(\varepsilon+U) & f^-(\varepsilon+U) \\ 0 & f^+(\varepsilon+U) & f^+(\varepsilon+U) & -2f^-(\varepsilon+U) \end{pmatrix}, \quad (2.12)$$

where $\varepsilon = \varepsilon_d - eV_G$ is the effective single-particle energy in the presence of a gate potential. The full time-evolution of the occupation probabilities including the charging rates of the quantum can be obtained by calculating the eigenspace of the non-Hermitian matrix W. The formal solution reads

$$P(t) = \sum_i \exp(\gamma_i t)\,(\vec{r}_i \otimes \vec{l}_i)\,P(0), \quad (2.13)$$

where $\vec{l}_i$ and $\vec{r}_i$ are the left and right eigenvectors of W associated with the eigenvalue γ_i. The matrix W is not decomposable and time-independent, which implies that one eigenvalue is equal to zero and a stationary solution P_{eq} exists for $t \to \infty$ [73].

In the following, we are interested in the time scales of the time-dependent charge $n(t)$ in the quantum dot. Using the solution of the time-dependent occupations $P(t)$, we find that the time-dependent occupation is given by

$$n(t) = n_{in}\, e^{-\gamma_{charge} t} + n_{eq}\,(1 - e^{-\gamma_{charge} t}), \quad (2.14)$$

with the rate

$$\gamma_{charge} = \Gamma_0\,[f^+(\varepsilon_d - eV) + f^-(\varepsilon_d - eV + U)]\,. \quad (2.15)$$

The initial occupation of the quantum dot n_{in} decays, while the equilibrium occupation

$$n_{eq} = \frac{2\,f(\varepsilon)}{1 + f(\varepsilon) - f(\varepsilon+U)}, \quad (2.16)$$

emerges on a time scale given by the rate γ_{charge}. In order to make a connection to the experimentally measured spectra, the change of the time-dependent electron number in the quantum dots with respect to the gate voltage is obtained from

$$\frac{dn}{dV_G}(t) = (1 - e^{-\gamma t})\,\frac{dn_{eq}}{dV_G} + t\,e^{-\gamma t}\,(n_{eq} - n_{in})\,\frac{d\gamma}{dV_G}. \quad (2.17)$$

The first part of Eq. (2.17) describes the exponential time evolution toward the equilibrium signal $\frac{dn_{eq}}{dV_G}$, while the second part accounts for the transients relating to the change

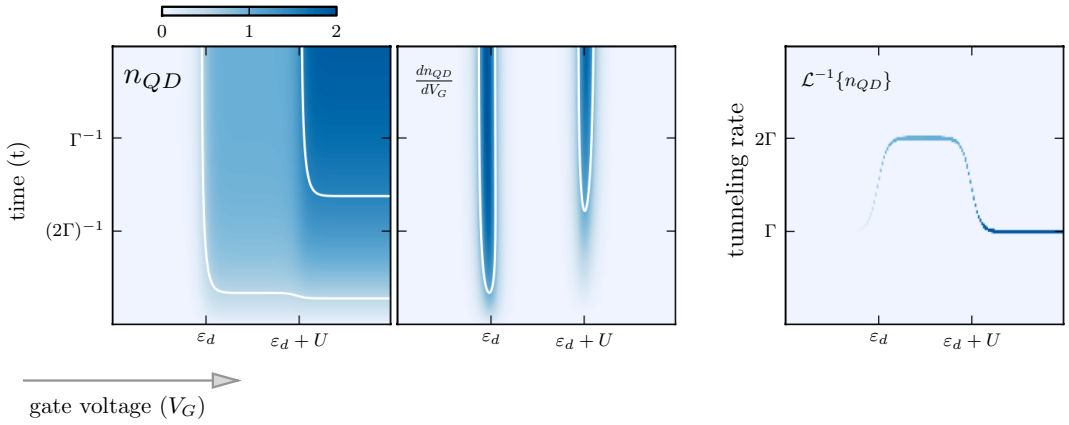

Figure 2.4: The time-dependent occupation $n(t)$, dn/dV_G and the inverse Laplace transform $\mathcal{L}^{-1}\{n(t)\}$ for a toy model of a single-level quantum dot. Peaks in dn/dV_G show the charging of the quantum dot with one and two electrons at the position of their respective charging energies. The inverse Laplace transform $\mathcal{L}^{-1}$ reveals the rates and amplitudes of the exponential charging.

of the tunneling rate γ.

While the toy model exhibits only a single time-scale for the charge, later calculations will reveal a variety of different decay rates for a more complex quantum dot model. In order to uncover the time scales in the time-dependent occupation probability $n(t)$, we introduce the inverse Laplace transform $\mathcal{L}^{-1}\{n(t)\}$ applied to $n(t)$, defined as the inverse function to the Laplace transform

$$\mathcal{L}\{f(t)\} = \int_0^\infty dt\, e^{-st} f(t). \tag{2.18}$$

While $n(t)$ is given by a multi-exponential function, $\mathcal{L}^{-1}\{n(t)\}$ returns a delta function depending on the charging rates (Fig. 2.4). The inverse Laplace transform of the time-dependent occupation number is a convenient approach to quantitatively compare experimental measurements with theoretically obtained dynamics [74, 75].

2.3 Relaxation mechanisms

The transition rates in the master equation discussed so far induce transitions between quantum dot states by changing the electron number. In the following, intrinsic and extrinsic relaxation in the quantum dots due to interactions with the environment are discussed. While intrinsic relaxation mechanisms are related to phonons or spin-orbit in-

teraction, extrinsic relaxation mechanisms arise from the coupling to an external electron reservoir (e.g. an electron gas). Different means of relaxation are exemplarily discussed to include them as effective rates for orbital and spin relaxation in the master equation.

2.3.1 Intrinsic relaxation due to interaction with phonons

Transitions between non-degenerate quantum dot states can be induced by phonon interaction while keeping the number of electrons constant. Commonly, bulk phonons are discussed as the main relaxation mechanism. While this approach is not always accurate because quantum dots are formed at a heterointerface, considering only bulk phonons has proved to be adequate in explaining experimental observations of phonon relaxation [76–78]. Generally, two types of phonon interaction are distinguished, depending on the particular way in which electric field fluctuations are generated. The deformation of the crystal lattice alters the band-gap in space and leads to fluctuations in the electric field associated with the so-called deformation potential (DP) phonons. While DP phonons emerge in all semiconductors, so-called piezo-electric (PZ) phonons occur in polar crystals like GaAs, where strain leads to electric fields.

The interaction of electrons in the dot with phonons can be captured in the following Hamiltonian

$$\mathcal{H}_{e,ph} = \sum_{\vec{k},\vec{q},\sigma} M_{\vec{q},\lambda} \left(-b^\dagger_{\vec{q},\lambda} + b_{\vec{q},\lambda}\right) c^\dagger_{\vec{k}+\vec{q},\sigma} c_{\vec{k},\sigma}, \tag{2.19}$$

where $b^\dagger_{\vec{q},\lambda}, b_{\vec{q},\lambda}$ are phonon creation and annihilation operators, $\vec{q}$ is the three-dimensional phonon wave vector, λ is the phonon's polarization (one longitudinal and two transversal), and $c^{(\dagger)}_{\vec{k},\sigma}$ create/annihilate electrons with momentum $\vec{k}$ and spin σ. The geometrical factors $M_{\vec{q},\lambda}$ measure the electric field strength and define the dispersion relation of phonons. Piezo-electric phonons scale as $1/\sqrt{q}$, while deformation potential phonons scale as $\sqrt{q}$. Small phonon energies correspond to long wavelengths associated with the piezo-electric effect, while higher phonon energies are linked to the deformation potential.

The matrix elements connecting different orbitals depend on the size of the quantum dot and the phonon wavelength [79]. The electron-phonon interaction is averaged out for high phonon energies, where the phonon wavelengths are much shorter than the size of the quantum dot. For very small energies, the electron-phonon coupling decreases as well, because phonon wavelengths much longer than the quantum dot size just shift the entire potential of the quantum dot without coupling different orbitals. The most efficient electron-phonon coupling inducing transitions between quantum dot orbitals occurs for phonon wavelengths comparable to the quantum dot size.

Electrons can dissipate and absorb energy due to phonon interaction. However, the isolated action of the phonon interaction conserves the total spin and cannot induce spin transitions in the quantum dots. Therefore, we discriminate between purely orbital relaxation caused by the dissipation of energy through phonons and spin relaxation. Spin relaxation in the quantum dots can be affiliated to two principle mechanisms [57]. Hyperfine interaction of the lattice nuclei with the electron spins evokes spin relaxation [80–82]. While the nuclei and electrons can exchange momentum, the discrepancy between energy scales prevents energy exchange. Thus, energy relaxation between different spin states occurs due to the combination of hyperfine and phonon coupling. If the relaxation mechanism is produced by such higher order process, spin relaxation times can be very long compared to orbital relaxation [76].

An additional spin relaxation mechanism is associated with spin-orbit coupling, which induces spin-flip transition. Spin-orbit coupling arises in solids due to internal magnetic fields. For example, the bulk inversion asymmetry in crystals like the zinc-blende structure of GaAs leads to a contribution to the spin-orbit interaction, denoted as Dresselhaus effect [83,84]. Furthermore, structural inversion asymmetry due to asymmetric confining potentials contribute to the spin-orbit coupling, which is known as Rashba term [85,86].

The type and magnitude of relaxation mechanisms present in experiments depends on various factors like the material of the QDs, temperature, and internal and external fields [57]. The later analysis, however, does not aim at a quantitative description of relaxation processes, but will include orbital and spin relaxation as an effective transition mechanism in the master equation.

2.3.2 Extrinsic spin relaxation due to interaction with an electron bath

In the previous section, two intrinsic mechanisms producing spin relaxation have been described: spin-orbit interaction and hyperfine interaction with nuclear spins. Spin-flip times can be as short as a few 10 ns without magnetic fields and up to a few milliseconds with an applied magnetic field [57]. If the quantum dots are strongly coupled to an electron reservoir and the intrinsic relaxation times are long compared to the tunneling time, then extrinsic spin-relaxation mechanisms due to electron tunneling can be important [87].

In order to illustrate the basic mechanisms involved in extrinsic spin-relaxation, we consider a spin-degenerate level with energies $E_\uparrow = E_\downarrow = E$ coupled to a single electron reservoir. The distance between the Fermi energy E_F in the reservoir and the energy levels in the quantum dot is denoted by $\Delta = E - E_F$. The relevant states in the quantum

dot are empty (P_0) and singly occupied with spin up or down ($P_\uparrow$ and $P_\downarrow$). The sequential tunneling rates in this simplified model are given by

$$\gamma_+ = \Gamma_0 \, f^+(\Delta), \tag{2.20}$$

$$\gamma_- = \Gamma_0 \, f^-(\Delta), \tag{2.21}$$

for processes that involve an electron tunneling into (γ_+) and off (γ_-) the quantum dot. Here, $f^\pm(\Delta) = [1 + \exp(\pm\Delta/k_BT)]^{-1}$ corresponds to the Fermi function of the lead. The next order transition rates associated with double exchange of electrons between the quantum dot and reservoir involve the virtual states $|\uparrow\rangle$ and $|\downarrow\rangle$

$$\gamma_2 = \frac{2\pi}{\hbar} \sum_k N_F \, |W_k|^4 \left| \frac{1}{\Delta - E_k + i0} \right|^2 f^+(E_k) \, f^-(E_k), \tag{2.22}$$

where E_k is the energy of an electron in the reservoir. The transition rate γ_2 is relevant for energies $|\Delta| \gg k_BT$, when contributions for $E_k \approx \Delta$ are exponentially suppressed. In this low temperature regime, the transition rates can be approximated as

$$\gamma_2 = \tilde{\Gamma}_0^2 \frac{k_BT}{\Delta^2}, \tag{2.23}$$

with $\tilde{\Gamma}_0^2 = \frac{\hbar}{2\pi}\Gamma_0^2$ and $\Gamma_0 = \frac{2\pi}{\hbar} N_F |W_k|^2$. Solving this model gives two relevant time scales associated with charge $P_\uparrow + P_\downarrow$ and spin $P_\uparrow - P_\downarrow$. The rates corresponding to charging (γ_{charge}) and spin relaxation (γ_{spin}) are given by

$$\gamma_{spin} = \gamma_- + 2\,\gamma_2, \tag{2.24}$$

$$\gamma_{charge} = \gamma_- + 2\,\gamma_+^2. \tag{2.25}$$

Both rates receive contributions in the order of the square of the tunneling time. While extrinsic spin relaxation has been observed in strongly coupled systems [88], this type of relaxation mechanism is of minor importance in quantum dots for which the tunneling time is long compared to the instrinsic relaxation time. At a later point in chapter 3, we will show that extrinsic relaxation can have a strong impact on the spin noise.

2.4 Charge dynamics in multi-level quantum dots

In section 2.2.1, the time scales of the charge dynamics of a single-level quantum dot are determined by the bare tunneling time Γ_0 and the degeneracy of the participating

quantum dot states. In the following, we extent the study to a many-orbital quantum dot in order to examine the effects of orbital correlations and intrinsic relaxation mechanisms on the charging dynamics.

We start with the discussion of the conditions in the experiment by Marquardt et. al [9]. The energies in the self-assembled InAs quantum dots correspond to a level spacing of $\hbar\omega_0 = 52$ meV and an effective Hartree energy of Ha$^* =$ Ha $m^*/(m_e\varepsilon^2) = 7.1$ meV. These parameters have been obtained by fitting $\hbar\omega_0$ to the energy spacing between the signals corresponding to the first electron tunneling into the s, p, and d shell, associated with the degenerate single-electron ground state and excited states. The strength of the Coulomb interaction can be adjusted by identifying the position of the signal associated with the two-particle ground state. For these particular parameters, the electrons in the quantum dots can be regarded as weakly interacting. The exact many-particle states together with the corresponding energies E_N^i for $N = 1-6$ electrons are calculated using exact diagonalization [89]. Considering the symmetries of the system, a classification of eigenstates by the angular moment L, the total spin S and by spin projection S_z can be achieved.

The sequential tunneling of an electron into a quantum dot changes the electron number $N \to N+1$ whenever the tunneling condition

$$\Delta E^{N+1} = E_{N+1}^i - E_N^j \lesssim eV_G. \tag{2.26}$$

is fulfilled (assuming $k_BT \ll \Delta E^{N+1}$). Relaxation, e.g. through phonons, however, modifies the tunneling condition if relaxation occurs on time scales that are in the order of the tunneling time or faster. In a first step, an instantaneous orbital and spin relaxation is assumed (orders of magnitude faster than the tunneling time), which leads to the tunneling condition

$$\Delta E^{N+1} = E_{N+1}^i - E_N^{GS} \lesssim eV_G, \tag{2.27}$$

where E_N^{GS} is the energy associated with the N-particle ground state.

In Fig. 2.5, the energy differences ΔE^{N+1} obtained by exact diagonalzation are shown together with their degeneracy and total spin of the final $(N+1)$-state. Using the obtained energies and many-particle states, the transition rates for the master equation are evaluated. We obtain the charge dynamics for an initially empty quantum dot by solving the master equation and calculating the inverse Laplace transform of the particle density depicted in Fig. 2.6.

Each line shown in the depiction of the inverse Laplace transform corresponds to a rate associated with a charge state of the quantum dot. As the gate voltage increases, additional rates emerge, which can be attributed to intermediate and final charge states.

In the regime of gate voltages between $1.0 - 2.0\,\hbar\omega_0$, the first two electrons are charged into the respective ground states. Similar to the previous example of a single-level quantum dot, the time scale for charging the multi-level quantum dot with electrons is associated with the degeneracy of states. Moreover, the charging times of electrons tunneling into p and d orbitals at multiples of $\hbar\omega_0$ can be identified. They correspond to the number of all available one-electron states at the specific gate voltage. Similarly, the many-particle charging rates depend on the degeneracy of many-particle states. Correlations, however, can reduce their magnitude, which can be seen, for example, in the charging of two-particle states.

For gate voltages between $2.0\,\hbar\omega_0$ and $2.5\,\hbar\omega_0$, excited two-particle states are charged. The charging time at an energy associated with the lowest two-particle triplet state cannot be purely described by the degeneracy factor. For example, transition rates between a single spin-up electron state and two-electron states given by the singlet ground state and states with $S = 1$, $S_z = \{0, 1\}$, and $L = \pm 1$, would result in a deceptive rate of $\Gamma = 5\,\Gamma_0$.

The exchange correlations of the states with $S = 1$, $S_z = 0$ and $L = \pm 1$, however, reduce the total transition rate observed in Fig. 2.6. Similarly, Coulomb correlations can reduce the transition rates, which are proportional to the Fermi function as well as

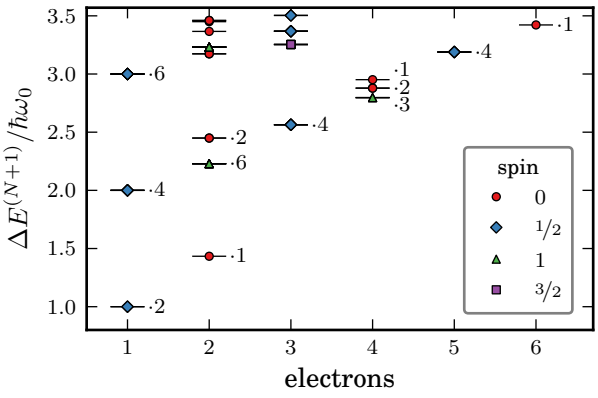

Figure 2.5: Low-lying energy spectrum of the quantum dot with up to 6 electrons with spin and multiplicity. The energy difference $\Delta E^{(N+1)} = E_\alpha^{(N+1)} - E_{GS}^{(N)}$ is shown, based on which the required gate voltage for a transition by a tunneling electron can be inferred according to $\Delta E^{N+1} \lesssim eV_G$.

to the spectral weight $S_{\alpha\beta} = \sum_a |\langle\beta|d_a^\dagger|\alpha\rangle|^2$. The effect of Coulomb correlations will be examined in more detail in the next section.

The trace of tunneling rates exhibits distinct features that do not only depend on the bare tunneling rate, but are also associated with degeneracy and correlations in the quantum dot. With the knowledge of the time scales in the system, the time-dependent charging of a quantum dot can be determined and compared to the experiment. For this purpose, a Laplace transform

$$n(t) = \int \mathrm{d}\Gamma\, \mathcal{L}^{-1} \exp(\Gamma t) \tag{2.28}$$

is applied to the numerically obtained data shown in Fig. 2.6 in order to obtain the charge density $n(t)$ versus gate voltage. The differential conductance of the 2DEG measured in experiments depends on the change of the charge state in the quantum dots with respect to the gate voltage $dn(t)/dV_G$ (c.f. sec. 3.1). The signal only indicates a change in the charge occupation with respect to the gate bias and, thus, can give information about charging times, but not individual tunneling channels. In the following calculation of $n(t)$, a Gaussian broadening of width $\sigma = 0.1\,\hbar\omega_0$ is applied to simulate an ensemble

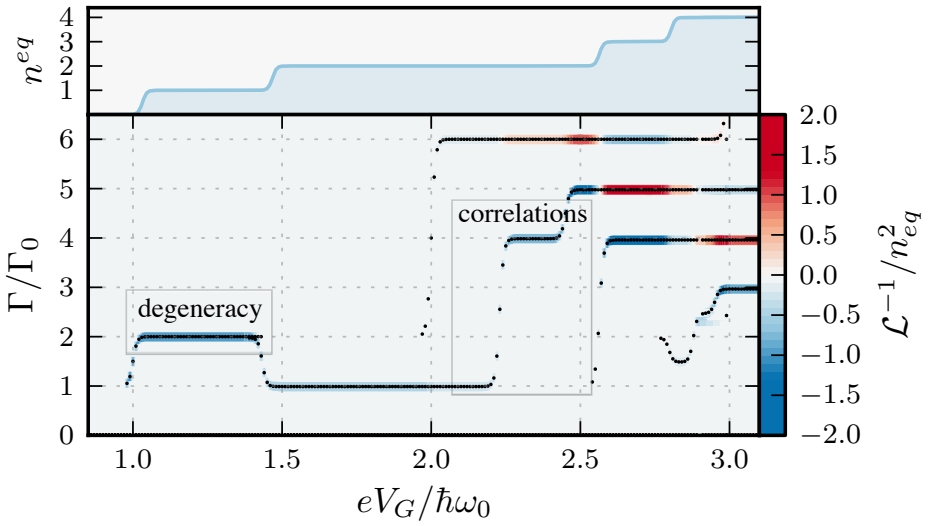

Figure 2.6: Upper panel shows the equilibrium occupation $n_{eq} = \lim_{t\to\infty} n(t)$ of the quantum dot with up to 4 particles. The inverse Laplace transform (lower panel) uncovers the rates involved in the time evolution from non-equilibrium to equilibrium. Examples for the effect of degeneracy and correlations in the quantum dot are highlighted. The line spread across the Γ axis has been broadened to ease the readability of the lower plot. The tunneling rate $\Gamma = 12\,\Gamma_0$ emerging at $eV_G = 3.0\,\hbar\omega_0$ is not shown.

broadening and allow for a clearer depiction.

The simulated time-dependent charging depicted in Fig. 2.7 reproduces many features of the experimental data (Fig. 2.3), despite having approximated the bare tunneling time as being constant.

For short times, peaks at multiples of the harmonic confinement energy are noticeable and are associated with the charging of a single electron into the s, p and d shell. The long-time limit exhibits distinct peaks when an additional electron charges the quantum dots and induces transitions exclusively between ground states. During the charging toward the equilibrium state, several transients appear that depend on the charging times in Fig. 2.6. These transients only indicate a change in the transient charge occupation (signal $\propto dn(t)/dV_G$). While different features are reproduced, a quantitative analysis is limited by undetermined effects like, for example, the energy dependence of the tunnel barrier. Nevertheless, the present analysis demonstrates the characteristics originating from the electronic structure of the quantum dots.

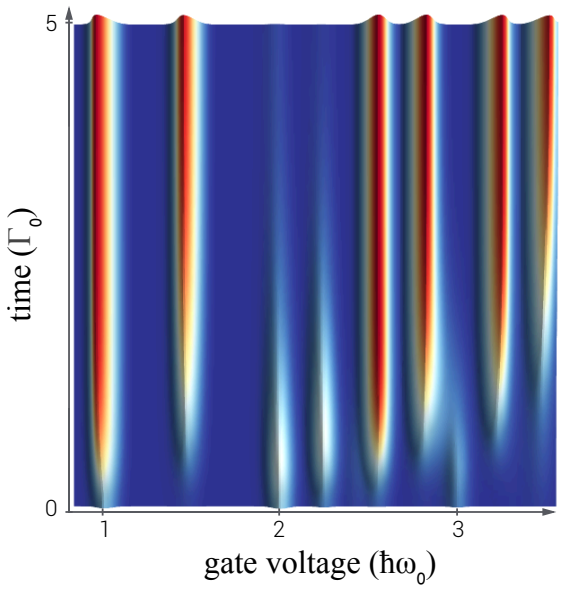

Figure 2.7: Density plot of $\frac{dn}{dV_G}(t)$ as a function of gate voltage V_G and time t (blue to red equals low to high). Different peak structures are recognizable, which correspond to electrons charging into ground states and excited states. At short times, three distinct peaks at multiples of $\hbar\omega_0$ are associated with the single-particle charging into the quantum dot orbitals. Another transient peak corresponds to the charging of an excited two-particle state with $S = 1$. Long times exhibit peaks for transitions between $(n-1) \to n$ particle ground states.

2.4.1 Coulomb correlation and spin relaxation

The effects of Coulomb correlation and relaxation on the charging times are unveiled in Fig. 2.8 for the example of a $2 \rightarrow 3$ particle transition rate. Fig. 2.8 (left) shows the transition rate between the two-particle ground state and all accessible three-particle states as a function of gate voltage and for different level spacings in the quantum dot. A QD with a harmonic confinement strength of $\hbar\omega_0$ = 50 meV (Fig. 2.8, dark blue) can be regarded as weakly correlated,[1] and the effective transition rates are primarily associated with the degeneracy of states. For smaller confinement energies, Coulomb interaction leads to stronger correlated states and the absolute value of the spectral weight is reduced. Consequently, the steps in transition rates are not only shifted to higher gate voltages proportional to the strength of Coulomb interaction, but also their magnitude is reduced by the effect of Coulomb correlations. In strongly correlated quantum dots, the charging time of many-particle states is prolonged compared to weakly correlated quantum dots.

Fig. 2.8 (right) shows the impact of a spin relaxation time much larger than the tunneling time on the effective transition rate between 2 and 3 particle states. When the relaxation time is long compared to the tunneling time, a finite probability of occupying excited states exists. In the example of two particle configurations, the ground state

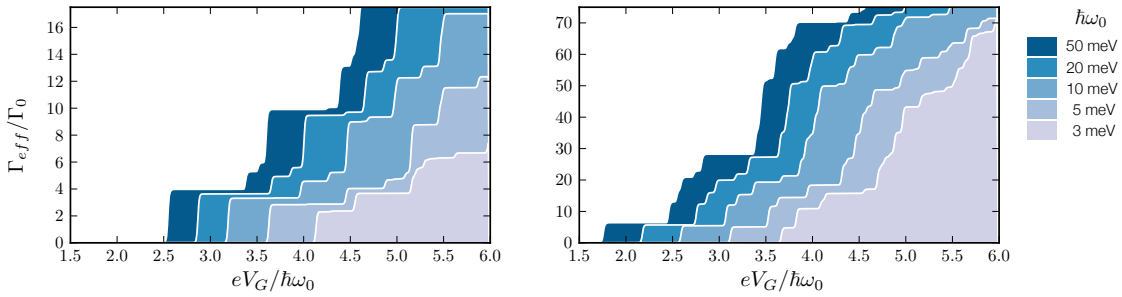

Figure 2.8: Effective rate for changing the electron number in the QD from 2 to 3 for different single-particle energies $\hbar\omega_0$ (Ha* = 7.1meV from [9]) with fast spin relaxation rate (left) and slow spin relaxation rate (right). In the left figure, only transitions between the 2-particle ground state and all available 3-particle states at a given gate voltage are involved. Large $\hbar\omega_0$ lead to transition rates determined by the degeneracy and exchange correlations, while at smaller $\hbar\omega_0$ Coulomb correlations reduce the transition rates. In the right panel, transitions from the 2-particle ground state (singlet) and first excited spin state (triplet) to the available 3-particle states give rates that are one magnitude larger than in the left panel.

[1] $\hbar\omega_0/\text{Ha}^* \approx 7.3$ for self-assembled InAs QDs in [9].

(singlet) and also the first excited states (triplet) are initially available, which results in a larger number of possible transitions. The effective transition rates shown in Fig. 2.8 (right) become one magnitude larger than in Fig. 2.8 (left).

2.5 The role of the tunneling matrix element

In the previous sections, the single-electron tunneling rate in different quantum dot orbitals has been considered as a constant rate Γ_0. In the following, we discuss consequences of including the effect of the overlap between single-particle wave functions in the quantum dot and a two dimensional electron gas. The transition rates for tunneling through the barrier separating QD and 2DEG are proportional to the overlap matrix elements $t_{\vec{k}}$. These matrix elements can be expressed by [37]

$$t_{\vec{k}} = -\frac{\hbar^2}{2m} \iint d^2S \left(\Psi^*_{qd} \left.\frac{\partial \Psi_{2d}}{\partial z}\right|_{z=z_0} - \Psi_{2d} \left.\frac{\partial \Psi_{qd}}{\partial z}\right|_{z=z_0} \right). \tag{2.29}$$

The integration has to be carried out in the plane separating the 2DEG and QD at $z = z_0$. Neglecting the coupling between x, y and z coordinates, the following wave functions for the two domains of the barrier can be used

$$\Psi^{(\nu)}_{2d} = \exp(ik_x x)\, \exp(ik_y y)\, \chi_{2d}(z), \qquad \text{(2DEG)} \tag{2.30}$$

$$\Psi^{(n,m)}_{qd} = \Psi^{(n,m)}_{qd}(x, y)\, \chi_{qd}(z), \qquad \text{(QD)} \tag{2.31}$$

where $\Psi^{(\nu)}_{2d}$ and $\Psi^{(n,m)}_{qd}$ are the single-particle wave functions in the 2DEG and QD, respectively. The 2DEG wave function can be expressed as plane waves with momentum $\vec{k}$ in the $x-y$ plane and a separated part χ_{2d} in z direction. The QD wave function is also separated into a part $\Psi^{(n,m)}_{qd}$ depending on the quantum numbers n, m and a z-dependent part χ_{qd}. Assuming the 2DEG and QD stacked in z-direction with the interface at z_0, the transfer matrix elements reads

$$t_{\vec{k}} = -\frac{\hbar^2}{2m} \left(\chi^*_{qd} \left.\frac{\partial \chi_{2d}}{\partial z}\right|_{z=z_0} - \chi_{2d} \left.\frac{\partial \chi_{qd}}{\partial z}\right|_{z=z_0} \right) \tilde{\Psi}_{qd}(k_x, k_y), \tag{2.32}$$

where $\tilde{\Psi}_{qd}(k_x, k_y)$ is the Fourier transform of the quantum dot wave function $\Psi_{qd}(x, y)$. In Fig. 2.9, the single-particle tunneling rates $\Gamma = \frac{2\pi}{\hbar} \sum_{\vec{k}} t^*_{\vec{k}}\, t_{\vec{k}}\, \delta(\varepsilon - \varepsilon_k)$ (Eq. 2.10) are calculated for resonant tunneling into different quantum dot orbitals as a function of the QD size $\ell_{QD} = \sqrt{\hbar/m^*\omega_0}$ and the Fermi vector $k_{Fermi} = |\vec{k}_{Fermi}|$ of the tunneling electron. The z-dependent part of the transfer matrix elements is assumed to be independent of

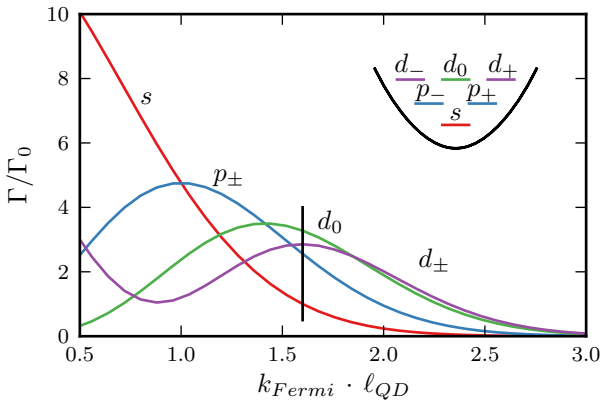

Figure 2.9: Single-particle rate Γ for tunneling into different QD orbitals as a function of QD size ℓ_{QD} and Fermi wave vector in the 2DEG k_{Fermi}. The inset schematically depicts the orbitals in an isotropic harmonic potential. Experimentally determined values are marked by a vertical black line corresponding to ℓ_{QD} = 8nm and k_{Fermi} = 0.2 nm^{-1} [25]. The tunneling rates are normalized by Γ_0 associated with tunneling into an s-orbital at $k_{Fermi} \cdot \ell_{QD} = 1.6$.

the specific QD orbitals and constant. Then, the momentum integral is calculated by integrating over the Fermi circle.

The tunneling rates for different orbitals strongly dependent on the size of the quantum dot and the Fermi wave vector k_{Fermi}, which itself depends on the carrier density in the 2DEG. For small quantum dots and small wave vectors, tunneling into an s and p orbital is faster compared to tunneling into the d-shell. The single-particle ground state in the QD is localized at the center and gives rise to larger contributions for a small wave vector. For larger quantum dots and larger wave vectors, tunneling into s orbitals becomes the slowest process. The larger contributions from p and d orbitals together with the high degeneracy leads to the fast charging times experimentally observed for excited states and many-electron ground states [9].

2.6 Summary

We have studied the charging times emerging in the time-evolution of a multi-level quantum dot with full Coulomb interaction coupled to an electron gas, after a sudden change in the gate potential. Employing exact diagonalization and a master equation approach revealed various contributing factors determining the charging time scales: degeneracy of the quantum dot states, exchange and Coulomb correlations, internal relaxation, and overlap between single-particle wave functions in the quantum dot and

the electron gas.

A toy model of a single-level quantum dot showed that the degeneracy together with the bare tunneling rate defines the charging rate of electrons into the system. The analysis have been extended to a multi-level quantum dot where tunneling rates are no longer uniquely determined by the degeneracy. Exchange correlation prevalent in many-electron states reduce the magnitude of spectral weights and, as a consequence, extend transition times between few-particle configurations. In addition, transition rates are reduced in quantum dots where strong Coulomb interaction leads to correlated states.

Furthermore, the effect of orbital relaxation and spin relaxation on the charging rates has been studied. While the direct observation of relaxation rates in the time-dependent occupation of the quantum dot is not possible, internal relaxation affects the number of available tunneling channels as well as the magnitude of transients in $dn(t)/dV$. In systems with long spin relaxation times, a transient occupation of excited states is available leading to huge charging rates compared to the bare tunneling rate.

The described aspects are related to the internal structure of the quantum dot and have been obtained using a constant parameter for the tunneling rate. In a final step, the overlap between single-particle wave functions in the quantum dot and electron gas shows a strong dependence on the quantum dot size and the carrier concentration in the electron gas. For designated parameters, a stronger tunneling into ground states or excited states can be induced.

The analysis has shown that the presented theoretical approach provides a sound framework for the interpretation of experimental findings and for the disentanglement of effects observed. Furthermore, the presented theory can be used as a starting point for the targeted design of further experiments to study the non-equilibrium dynamics of quantum dots.

This page intentionally left blank.

3 Spin Noise in Small Ferromagnetic Cluster on Surfaces

3.1 Experimental motivation

Controlling and probing the spin of a single magnetic ion and small magnetic cluster in order to store classical and quantum information has recently attracted scientific interest. Crucial for the application as storage is the understanding of interactions at the nanoscale, determining magnetic stability. Scanning tunneling microscopy (STM) offers a versatile tool to probe and manipulate the spin of atoms deposited on a conducting surface [90]. An STM setup consists of a sample, e.g. a single atom or atomic cluster, placed on top of an atomically flat surface, and an atomically sharp tip (schematically sketched in Fig. 3.1). Two complementary methods have been developed to probe the spin of a single or few atoms: spin-flip inelastic electron tunneling spectroscopy (IETS) and spin-polarized scanning tunneling microscopy (SP-STM).

In IETS, the spin excitation energies of the sample are resolved by measuring the current-voltage characteristics. When a voltage is applied between the STM tip and the surface, electrons tunnel from the tip to the surface or vice versa. Only an elastic tunneling current is measured when the applied voltage is smaller than the excitation energy of the sample. When the bias voltage exceeds the excitation energy associated with a spin transition in the sample, an additional inelastic tunneling current is measured. This leads to a change in current I measured versus the voltage V, which is visible as a step in the conductance dI/dV at voltages associated with spin excitations.

SP-STM, on the other hand, utilizes a spin-polarized current to measure the spin-dependent magneto-resistance of the sample. This procedure can be used as a spectroscopic tool to provide information about the orientation of the spin of the sample relative to the spin of the conduction electrons in the STM tip. At the same time, it allows to manipulate the orientation of the spin of the atoms by exerting spin-transfer torque. Electrons from the STM tip induce inelastic spin flips in the sample that favorably excite spin states depending on the spin polarization of the current.

IETS and SP-STM probe the spin state of the sample through spin-dependent electron tunneling. Simultaneously, the tunneling electrons can modify the spin state of the

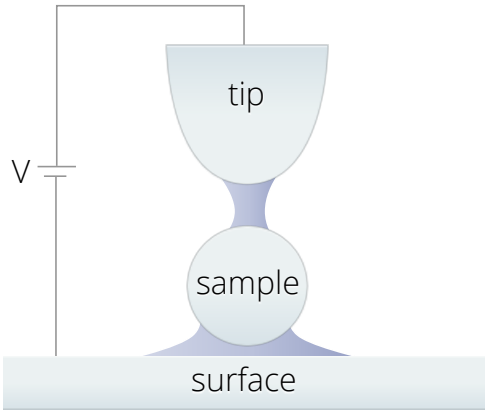

Figure 3.1: Schematic depiction of a scanning tunneling microscopy setup. The sample is deposited on an atomically flat, conducting surface and probed by an atomically sharp tip. By applying a voltage V between the tip and the surface, electrons tunnel from the tip to the surface or vice versa.

sample by inelastic excitation. Two distinct time scales are relevant: the average time between two spin flip events t_{flip} and the spin relaxation time t_{relax}. For $t_{flip} \gg t_{relax}$, the spin of the sample atoms is driven out of equilibrium, leading to bias-dependent spin states. In the complementary regime $t_{flip} \ll t_{relax}$, the spin of the sample atoms is in equilibrium with the environment while interacting with the tunneling electrons.

In the intermediate regime, few-atom systems have revealed magnetic bistability at low temperatures, which manifests in a measured telegraph signal [14, 15]. Magnetic bistabilities are not only of interest as a potential implementation of information storage, but also because they shed light on the role of the interaction with substrate and tip in the dynamics of a atomic-scale magnet.

In *Science* 339, 55 (2013) [15], we have shown that the bistability in a few-atom cluster originates in the interplay between spin flips, magnetic relaxation and magnetization tunneling. In this chapter, we show how the spin noise in the cluster can be obtained by a master equation approach taking into account the interactions with surface and tip. We discuss the contribution of spin flips, magnetic relaxation and magnetization tunneling to the dynamics of a small ferromagnetic cluster and analyze the influence of an applied voltage, temperature and an external magnetic field.

3.2 Spin Hamiltonian

We start with a brief overview of the spin Hamiltonian approach, while referring to [26] for more details. A *spin Hamiltonian* is a common approach to interpret the spectra of magnetic systems without treating the full microscopic Hamiltonian. In this approach, orbital degrees of freedom are eliminated and the system is described only by spin coordinates. The spin Hamiltonian represents a good approximation for low-lying energy states of a magnetic system.

In this approach, a magnetic atom with n unpaired electrons is characterized by a total spin of $S = n/2$. External fields and interactions with the surrounding can reduce the symmetry of the system and split the $2S+1$ spin levels. In the following, two different terms will be introduced in the Hamiltonian: a Zeeman Hamiltonian and a crystal field Hamiltonian.

The Zeeman Hamiltonian associated with an applied magnetic field can be written as

$$H_{\mathrm{Z}} = g\,\mu_{\mathrm{B}}\,\mathbf{B}\,\mathbf{S}, \tag{3.1}$$

where μ_{B} is the Bohr magneton, $\mathbf{B}$ is the magnetic field and $\mathbf{S}$ is the spin vector. Here, g is a system-specific Landé factor which connects spin and magnetic field.

The crystal field Hamiltonian presents an effective treatment of the interaction with surrounding atoms, e.g. in the underlying non-magnetic surface. In many cases, a good approximation is provided by a Hamiltonian that is quadratic in the spin operators [91]

$$H_{\mathrm{CF}} = \mathbf{S}\,\mathbf{D}\,\mathbf{S}, \tag{3.2}$$

where $\mathbf{D}$ is a real, symmetric tensor. This Hamiltonian can be recast through unitary transformation into

$$H_{\mathrm{CF}} = D\,S_z^2 + E\,(S_x^2 - S_y^2), \tag{3.3}$$

where D and E are the axial and transverse anisotropy, respectively. The transformed Hamiltonian Eq. (3.3) shows the following advantage if expressed in the basis spanned by the eigenvectors $|m\rangle$ of S_z, with $S_z\,|m\rangle = m\,|m\rangle$ and $m = -S, \ldots, S-1, S$. The first term of Eq. (3.3) has only diagonal elements. In contrast, diagonal elements are absent in the second term of Eq. (3.3). Both terms remove the $(2S+1)$ degeneracy of the spin multiplet even in the absence of an external magnetic field which is reflected in the expression zero-field splitting (ZFS).

In a system with axial symmetry, i.e. $E = 0$, the crystal field Hamiltonian simplifies to

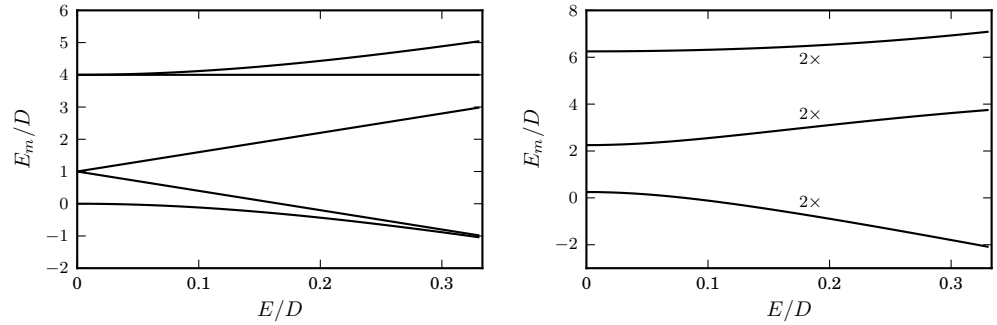

Figure 3.2: Energy spectrum of the crystal field Hamiltonian for $S = 2$ (left) and $S = 5/2$ (right) versus the transverse anisotropy. Each branch of $S = 5/2$ is doubly degenerated.

$H_{\mathrm{CF}} = D\,S_z^2$ yielding eigenstates $|m\rangle$ and eigenenergies

$$E_m = D\,m^2. \tag{3.4}$$

A pair of eigenstates $|m\rangle$ and $|-m\rangle$ is degenerate. Reducing the symmetry by a non-zero value of E removes this degeneracy if S is integer. In the case of S being half-integer, time reversal symmetry is retained and $(S + 1/2)$ pairs of degenerate levels are found, which are called Kramers doublets [92]. It is common to limit values of E according to $-1/3 \leq E/D \leq 1/3$. Other values of E/D can be mapped back into the given range by renaming the reference axes.

Fig. 3.2 exemplarily shows the energy spectrum of the crystal field Hamiltonian for $S = 2$ (e.g. Fe [93]) and $S = 5/2$ (e.g. Mn [13]) and different values of E/D. Finite transverse anisotropy, E, completely removes the degeneracy in the case of integer spin. The double degeneracy is, however, retained for half-integer spin and all values of E. Transverse anisotropy also affects the composition of the eigenstates. For $E = 0$, the eigenstates are given by the pure eigenstates $|m\rangle$ of S_z. If E is finite, each eigenstate receives admixtures of different $|m\rangle$ states.

3.2.1 Spin Hamiltonian for a cluster

The spin Hamiltonian can be extended to treat a cluster of magnetic atoms. While each atom is described by a non-interacting Hamiltonian (Eq. 3.2 and Eq. 3.1), a common approach to add interaction among the atoms is given by a spin-spin Hamiltonian of the

form [94–96]

$$H_{SS} = \sum_{i<j} \mathbf{S}_i \, \mathbf{J}_{ij} \, \mathbf{S}_j, \tag{3.5}$$

where $\mathbf{S}_i$ are spin vectors and $\mathbf{J}_{ij}$ is a matrix describing the interaction between two spins. It is possible to discriminate between isotropic, anisotropic and antisymmetric spin-spin contributions by re-expressing Eq. (3.5)

$$H_{SS} = \sum_{i<j} \left[-J_{ij} \, \mathbf{S}_i \, \mathbf{S}_j + \mathbf{S}_i \, \mathbf{D}_{ij} \, \mathbf{S}_j + d_{ij} \, (\mathbf{S}_i \times \mathbf{S}_j) \right], \tag{3.6}$$

where the isotropy constant is $J_{ij} = -\mathrm{Tr}\, \mathbf{J}_{ij}/3$, the anisotropy constant is $\mathbf{D}_{ij} = (\mathbf{J}_{ij} + \mathbf{J}_{ij}^T)/2 - \mathrm{Tr}\, \mathbf{J}_{ij}/3$ and the antisymmetry constant is $\mathbf{d}_{ij} = (\mathbf{J}_{ij} - \mathbf{J}_{ij}^T)/2$. In the systems studied in the following, the isotropic interaction

$$H_J = -\sum_{i<j} J_{ij} \, \mathbf{S}_i \, \mathbf{S}_j, \tag{3.7}$$

will dominate, i.e. $J_{ij} \gg |\mathbf{D}_{ij}|, |\mathbf{d}_{ij}|$. In this case, the total spin $\mathbf{S} = \sum_i \mathbf{S}_i$ is a good quantum number and can be used to denote cluster states. In case of a dimer, for example, the energies are given by

$$E_S = -\frac{J_{12}}{2} \left[S(S+1) - S_1(S_1+1) - S_2(S_2+1) \right], \tag{3.8}$$

where the total spin, S, satisfies

$$|S_1 - S_2| \leq S \leq S_1 + S_2. \tag{3.9}$$

For ferromagnetic coupling ($J_{ij} > 0$), the ground state is given by S with maximum multiplicity, while for anti-ferromagnetic coupling ($J_{ij} < 0$) the total spin is minimal. The bilinear form of Eq. (3.7) represents the simplest approximation to the interaction energies of a cluster. In principle, one could also include anisotropic, antisymmetric or bi-quadratic terms. These contributions, however, are assumed to be small and, thus, will be neglected in the following.

The state space rapidly grows with the number of atoms in the cluster. The number of eigenstates in a cluster with N identical spins is $(2S+1)^N$. Further simplifications, however, can be made for strongly ferromagnetically coupled spins and if $|J_{ij}| \gg |D_i|, |D_{ij}|, |d_{ij}|$. In this case, it can be shown that an effective anisotropy ten-

sor exists [97]:

$$\mathbf{D}_S = \sum_i d_i \mathbf{D}_i + \sum_{i<j} d_{ij} \mathbf{D}_{ij}, \tag{3.10}$$

where

$$d_i = \frac{2S_i - 1}{N(2NS_i - 1)}, \quad d_{ij} = \frac{2S_i}{N(2NS_i - 1)}. \tag{3.11}$$

Similar formulas can be found for the effective coupling strength between spin and magnetic field, g_S. Using this argument, we will describe a ferromagnetic atom cluster by a single, effective spin exposed to a Hamiltonian which includes a crystal field, Eq. (3.2), and Zeeman interaction, Eq. (3.1).

3.3 Spin current through atoms and coupling to the surface

In the previous section, we introduced the spin Hamiltonian to model the low-lying energy spectrum of a magnetic atom and ferromagnetic cluster which represents the sample in an STM experiment. The magnetism in these systems arises from strongly interacting electrons in the d orbitals. If the sample is tunnel coupled to an STM tip, a current can flow through the system. The main conduction channel is assumed to be the s-channel, which gives rise to a model where d-levels are coupled to a non-interacting bath of conduction electrons. This can be described by the following Hamiltonian

$$\mathcal{H} = \mathcal{H}_{MS} + \mathcal{H}_B + \mathcal{H}_{MS\text{-}B}. \tag{3.12}$$

The magnetic system $\mathcal{H}_{MS}$ is coupled by $\mathcal{H}_{MS\text{-}B}$ to electrons originating from the surface (S) and STM tip (T), which are considered non-interacting electron baths $\mathcal{H}_B = \sum_\alpha \varepsilon_\alpha c_\alpha^\dagger c_\alpha$. The multi-index $\alpha = \{k, \sigma, r\}$ combines the momentum k, spin σ and bath $r = S, T$ of the electrons created (annihilated) by $c_\alpha^\dagger$ (c_α) in the STM tip or surface.

The magnetic system can be characterized by the number of electrons N in the incomplete shells of the ion and a set of quantum numbers $\mathbf{m}$ defining the multiplet. If the corresponding energies are denoted by $E_{N,\mathbf{m}}$, the Hamiltonian of the magnetic system yields

$$\mathcal{H}_{MS} = \sum_{N,\mathbf{m}} E_{N,\mathbf{m}} |N, \mathbf{m}\rangle\langle N, \mathbf{m}|. \tag{3.13}$$

The previously discussed spin Hamiltonian is one possible approximation of $\mathcal{H}_{MS}$ for ferromagnetic systems with fixed N.

The Hamiltonian $\mathcal{H}_{MS-B}$ couples d electrons and the conduction electrons and induces transitions between states $|N,\mathbf{m}\rangle$ and $|N',\mathbf{m}'\rangle$ for $N' = N \pm 1$:

$$\mathcal{H}_{MS-B} = \mathcal{H}^{+} + \mathcal{H}^{-} = \sum_{\alpha,\mathbf{m},\mathbf{m}'} V_{\alpha}^{\mathbf{m},\mathbf{m}'} |N+1,\mathbf{m}'\rangle\langle N,\mathbf{m}|c_{\alpha} + H.c.\,, \tag{3.14}$$

where $V_{\alpha}^{\mathbf{m},\mathbf{m}'}$ are the transition matrix elements. The Hamiltonian $\mathcal{H}$ (Eq. 3.12) combining all three parts is also known as ionic model [98] and represents a generalization of the Anderson model [23]. The number of parameters in this model makes it particularly complex. Therefore, we neglect in a first step the exchange interaction and other splittings and consider an N-impurity Anderson model for the N orbitals contributing to an effective spin of $S = N/2$ of the magnetic system

$$\mathcal{H}_{MS}^{U} = \sum_{i}^{N} \varepsilon_0 n_i + U n_i n_i, \tag{3.15}$$

where the number operator $n_i = \sum_{\sigma} d_{i\sigma}^{\dagger} d_{i\sigma}$ counts the electrons occupying the orbital i. The charge states with N, $N-1$ and $N+1$ electrons in the magnetic system are relevant for transport. In the magnetic systems under study, however, the chemical potentials for creating an electron $E(N) - E(N-1)$ or hole $E(N+1) - E(N)$ are of order eV [99] and much larger than the temperature $k_B T$ or the bias voltage $|V|$. This conditions lead to exponentially suppressed sequential tunneling through the system. In this deep co-tunneling regime, tunneling is only possible by coherent processes of higher orders and we will consider the fourth order in the coupling $\mathcal{H}_{MS-B}$.

To obtain the co-tunneling rates, an effective Hamiltonian $\mathcal{H}_{eff}$ can be derived by degenerate perturbation theory which describes the transfer of electrons between the system in lowest order [100],

$$\mathcal{H}_{eff} = \sum_{i,M_{\mp}} \frac{\mathcal{H}^{\pm}|M_{\mp}\rangle\langle M_{\mp}|\mathcal{H}^{\mp}}{E_{M_{\mp}} - E_0}, \tag{3.16}$$

where M_{+} (M_{-}) are products of states in the magnetic system with $N+1$ ($N-1$) electrons and bath states. Note that the following expressions can also be obtained by using other approaches like the Schrieffer-Wolff canonical transformation [101].

With the definition of the spin on the i-th impurity $S_i = \frac{1}{2}\sum_{\sigma\sigma'} d_{\sigma}^{\dagger}\tau_{\sigma\sigma'}d_{\sigma}$ and the spin density of the conduction electrons $s_{k,k',r,r'} = \frac{1}{2}\sum_{\sigma\sigma'} c_{k\sigma,r}^{\dagger}\tau_{\sigma\sigma'}c_{k\sigma r'}$ ($\tau_{\sigma\sigma'}$ are the Paul matrices), we obtain three contributions to $\mathcal{H}_{eff}$ after some calculations. First, an

exchange term

$$\mathcal{H}_{eff,ex} = \sum_{k,k',r,r'} J_{k,k',r,r'} s_{k,k',r,r'} \sum_i S_i, \tag{3.17}$$

with a tunneling-induced exchange interaction

$$J_{k,k',r,r'} = V^*_{k,r} V_{k',r'} \left(\frac{1}{\varepsilon_0 + U - \varepsilon_{kr}} + \frac{1}{\varepsilon_0 - \varepsilon_{k'r'}} \right). \tag{3.18}$$

Additionally, a direct, spin-independent interaction term appears

$$\mathcal{H}_{eff,d} = \sum_{k,k',\sigma,r,r'} U_{k,k',r,r'} c^\dagger_{k\sigma r} c_{k'\sigma r'}, \tag{3.19}$$

with

$$U_{k,k',r,r'} = V^*_{k,r} V_{k',r'} \sum_i \left(\frac{1}{\varepsilon_0 + U - \varepsilon_{kr}} - \frac{1}{\varepsilon_0 - \varepsilon_{k'r'}} \right). \tag{3.20}$$

The exchange term $\mathcal{H}_{eff,ex}$ can induce spin-flips between the spin of the magnetic system and the conduction electrons, which can be elastic or inelastic transitions. In contrast, the direct term $\mathcal{H}_{eff,d}$ characterizes spin-independent scattering of the conduction electrons. This term is still of importance as it represents interference between direct and exchange terms in the co-tunneling rates.

Finally, a third term $\mathcal{H}_{eff,int}$ is produced by Eq. (3.16) which describes inter-orbital interactions [102],

$$\mathcal{H}_{eff,int} = \sum_{k,k',r,r'} T_{k,k',r,r'} \sum_{i<j,\sigma} \left(d^\dagger_{i\sigma} d_{j\sigma} + d^\dagger_{j\sigma} d_{i\sigma} \right), \tag{3.21}$$

with

$$T_{k,k',r,r'} = \delta_{kk'} \delta_{rr'} |V_{k,r}|^2 \sum_i \frac{\varepsilon_0 + U - n_i U/2}{\varepsilon_0 \left(\varepsilon_0 + U \right)}. \tag{3.22}$$

The inter-orbital term is related to internal electron fluctuations between orbitals of the magnetic system. Strong Coulomb interaction leads to single occupancy of each orbital ($n_i \approx 1$), and in the limit of the particle-hole symmetry $\varepsilon_0 = -U/2$, the inter-orbital interaction gives only a small contribution. However, in the valence-fluctuation regime ($\varepsilon_0 \to 0$), internal noise originating from electrons hopping between the orbitals becomes important. In the following, we will only consider the case away from the valence-fluctuation regime and neglect $\mathcal{H}_{eff,int}$. Furthermore, we assume that the temperature in the system is low and the exchange term of the Coulomb interaction aligns the spins in the d orbitals. This leads to a ferromagnetic state with total spin $S = N/2$, and $\mathcal{H}_{eff,ex}$

is replaced by

$$\mathcal{H}_{eff,ex} = \sum_{k,k',r,r'} J_{k,k',r,r'} s_{k,k'} S, \tag{3.23}$$

with $S = \mathcal{P}(\sum_i S_i)\mathcal{P}$ and where $\mathcal{P}$ is projecting on the subspace of states with total spin $S = N/2$. In the following, the co-tunneling rates will only connect initial and final states with the same total spin S.

In a next step, the co-tunneling rates in a master equation approach can be obtained by applying Fermi's golden rule to $\mathcal{H}_{eff}$. With the spin-dependent density of states $\rho_{r,\sigma}$, the rates read [103, 104]

$$\begin{aligned} W^{r\sigma r'\sigma'}_{M,M'} = \frac{2\pi}{\hbar} \int d\varepsilon\, \rho_{r\sigma}(\varepsilon)\rho_{r\sigma'}(\varepsilon + \Delta_{M,M'}) f(\varepsilon - \mu_r)\left(1 - f(\varepsilon + \Delta_{M,M'} - \mu'_r)\right) \\ \times |\langle M|U + J\,\tau_{\sigma,\sigma'}\, S|M'\rangle|^2, \end{aligned} \tag{3.24}$$

where $f(\varepsilon)$ is the Fermi distribution function and $\Delta_{MM'} = E_M - E_{M'}$ is the energy difference between state $|M\rangle$ and $|M'\rangle$. Furthermore, we have introduced the parameterizations U and J for the contributions of the direct and exchange terms, respectively.

After rearranging the rates, we arrive at the following master equation

$$\frac{dP_M}{dt} = \sum_{M'} P_{M'} W_{M',M} - P_M \sum_{M'} W_{M,M'}. \tag{3.25}$$

The transition rates $W_{M,M'}$ between states M and M' are split into the following parts

$$W_{M,M'} = W^{(sub-sub)}_{M,M'} + W^{(tip-tip)}_{M,M'} + W^{(tip-sub)}_{M,M'} + W^{(sub-tip)}_{M,M'}. \tag{3.26}$$

The first part describes spin relaxation and thermal excitation of the sample by the surface electrons

$$W^{(sub-sub)}_{M,M'} = \Gamma_{S,S}\left(|S^{M,M'}_+|^2 + |S^{M,M'}_-|^2 + |S^{M,M'}_z|^2\right)\zeta(\Delta_{M,M'}), \tag{3.27}$$

with $\Gamma_{r,r'} = \frac{\pi}{\hbar} v_r^2 v_{r'}^2 \rho_r \rho_{r'} J^2$, $r = T$; S and $\rho_r = \rho_{r,\uparrow} + \rho_{r,\downarrow}$. The energy-dependent factor $\zeta(x) = x[1 - \exp(-\beta x)]^{-1}$ originates from the convolution of two Fermi functions associated with the creation and annihilation of surface or tip electrons. Furthermore, v_T and v_S have been introduced to parameterize the coupling strength of the magnetic system to the STM tip and substrate, respectively. The factor $\zeta(\Delta_{M,M'})$ can be re-expressed by using the Bose function $n_B(x) = [\exp(-\beta x) - 1]^{-1}$ as $\zeta(\Delta_{M,M'}) = \Delta_{M,M'}[1 + n_B(\Delta_{M,M'})]$. The first term of $\zeta(\Delta_{M,M'})$ corresponds to spontaneous relaxation, which is proportional

to the energy-difference between spin states, while the second term describes thermal spin excitation by surface electrons. The spectral weights for transitions are given by the matrix elements $|S_\alpha^{M,M'}|^2 = |\langle M|S_\alpha|M'\rangle|^2$.

In analogy, the interaction of the sample with the tip induces similar processes with

$$W_{M,M'}^{(tip-tip)} = \Gamma_{T,T}\left(|S_+^{M,M'}|^2 + |S_-^{M,M'}|^2 + |S_z^{M,M'}|^2\right)\zeta(\Delta_{M,M'}). \tag{3.28}$$

The third part of Eq. (3.26) includes electrons tunneling from the STM tip to the surface and vice versa with

$$W_{M,M'}^{(tip-sub)} = \Gamma_{T,S}\left(\frac{1-\mathcal{P}_T}{2}|S_+^{M,M'}|^2 + \frac{1+\mathcal{P}_T}{2}|S_-^{M,M'}|^2 + |S_z^{M,M'}|^2\right)\zeta(\Delta_{M,M'} + eV), \tag{3.29}$$

and

$$W_{M,M'}^{(sub-tip)} = \Gamma_{S,T}\left(\frac{1+\mathcal{P}_T}{2}|S_+^{M,M'}|^2 + \frac{1-\mathcal{P}_T}{2}|S_-^{M,M'}|^2 + |S_z^{M,M'}|^2\right)\zeta(\Delta_{M,M'} - eV). \tag{3.30}$$

Depending on the bias voltage between tip and surface, the spin of the sample is excited or de-excited. For a bias voltage smaller than the energy of the first spin excitation in the sample, inelastic co-tunneling ($\propto \zeta(\Delta_{M,M'} - eV)$) is suppressed, while the elastic current ($\propto \zeta(eV)$) has a linear V-dependence for $eV \gg k_BT$. A spin-polarized STM tip creates an asymmetry between the spin-flip processes involving the majority spin or minority spin given by the polarization $\mathcal{P}_T = \frac{\rho_{T,\uparrow}-\rho_{T,\downarrow}}{\rho_{T,\uparrow}+\rho_{T,\downarrow}}$.

When a bias voltage is applied between the STM tip and the surface, the steady-state current through the sample can be calculated by

$$I = -e\sum_{M,M'} P_M\left(W_{M,M'}^{tip-sub} - W_{M,M'}^{sub-tip}\right). \tag{3.31}$$

The current receives contributions associated with elastic and inelastic rates. With the ratio U/J between direct and exchange contributions, elastic rate ($\Delta_{M,M'} = 0$) are given by

$$W_{M,M'}^{r,r'} = \Gamma_{r,r'}\left[(U/J + S_z^{M,M'})^2\frac{1-\mathcal{P}_t}{2} + (U/J - S_z^{M,M'})^2\frac{1+\mathcal{P}_t}{2}\right]\zeta(\mu_r - \mu_{r'}), \tag{3.32}$$

and the inelastic rates ($\Delta_{M,M'} \neq 0$)

$$W^{r,r'}_{M,M'} = \Gamma_{r,r'} \left[|S^{M,M'}_{+}|^2 \frac{1 \mp \mathcal{P}_T}{2} + |S^{M,M'}_{-}|^2 \frac{1 \pm \mathcal{P}_T}{2} + |S^{M,M'}_{z}|^2 \right] \zeta(\Delta_{M,M'} + \mu_r - \mu_{r'}). \tag{3.33}$$

The elastic rates only give contributions to the current and, therefore, are not included in the rates changing the probabilities P_M. The rates contain direct and exchange contributions as well as interference terms that give rise to tunnel magneto-resistance (TMR). This effect is the underlying principle of spin-polarized STM when U is large compared to J [13–15]. In contrast, TMR is absent in inelastic tunneling spectroscopy (IETS) experiments due to the unpolarized STM tip. The contributions to the inelastic current are exclusively associated with elastic rates, which increases the current as more inelastic channels become available. Measurements of the differential conduction are a common tool to probe the spectra of magnetic atoms. In the following, we will show how the measurement of current noise can be used to obtain insight into dynamical processes in the magnetic systems.

3.4 Cumulants of current noise and spin noise

The measurement of shot noise goes back to 1918, when Walter Schottky performed experiments on electrical tubes. However, shot noise still gains both experimental and theoretical attention because it provides further insight into dynamical mechanisms in a system, well beyond mean quantities.

Shot noise denotes temporal fluctuations of electric current that originate from the discreteness of the charge carriers and depend on the charge of the particles as well as on their correlations. The current I fluctuates in time around its average value $\langle I \rangle$,

$$I(t) = \langle I \rangle + \delta I(t), \tag{3.34}$$

which gives rise to the current correlation function

$$S^{(2)}_I(t - t') = \langle \delta I(t) \delta I(t') \rangle. \tag{3.35}$$

The current correlation function is translation invariant for systems without time-dependent external fields and reduces to a function of $\tau = t - t'$. The corresponding spectral corre-

lation function is defined by

$$S_I^{(2)}(\omega) = \int d(t-t')\, e^{-i\omega(t-t')}\, \langle \delta I(t) \delta I(t') \rangle. \tag{3.36}$$

At low frequencies $\omega \to 0$, it can be discriminate between thermal noise and shot noise. In the zero-bias limit $V \to 0$, the correlation function $S_I^{(2)} \equiv \lim_{\omega \to 0} S_I^{(2)}(\omega)$ indicates thermal noise

$$S_I^{(2)} = 2\, k_B T\, G, \tag{3.37}$$

with temperature T and conductivity G of the sample. For finite bias, however, shot noise is obtained in the low-temperature limit $T \to 0$

$$S_I^{(2)} = F_2\, e\, \langle I \rangle, \tag{3.38}$$

where e is the electron charge. The Fano factor F_2 is sample specific and defines the ratio between the zero-frequency noise $S_I^{(2)}$ and the full Poisson noise $e\langle I \rangle$.[1] If successive electron tunneling events through a system are uncorrelated, then the low-frequency noise is $S_I^{(2)} = e\langle I \rangle$, which implies $F_2 = 1$. This case defines Poissonian (uncorrelated) shot noise. Interactions in the system lead to suppression or enhancement of shot noise with respect to the Poissonian limit. The system is then characterized by a sub-Poissonian Fano factor $F_2 < 1$ or by a super-Poissonian Fano factor $F_2 > 1$, respectively.

One example of the emergence of sub-Poissonian noise is transport through a single level in the Coulomb blockade regime. The Pauli exclusion principle introduces correlations which lead to a sub-Poissonian Fano factor between 1/2 and 1 depending on the asymmetry between left and right coupling of the level to external leads [105–107]. In contrast, if several channels with different coupling symmetries contribute to the current, then Coulomb correlations can lead to a super-Poissonian Fano factor. This has been theoretically predicted in single quantum dots with ferromagnetic leads [108–111] and coupled quantum dots [111–114]. Furthermore, super-Poissonian noise has been experimentally observed in tunnel barriers and quantum dots [59, 115–117].

Super-Poissonian noise has also been theoretically predicted in iron atoms deposited on a non-magnetic surface subject to an external magnetic field [118]. In the bias regime below the spin excitation threshold, a current associated with elastic co-tunneling leads to Poissonian shot noise. As soon as the bias can excite the spin of the atom from the ground state to the first excited state, super-Poissonian noise sets in.

In the following, we discuss shot noise and spin noise in a ferromagnetic atom cluster

[1] These expressions can vary by a factor of 2 due to different definitions in literature.

that possesses two degenerate ground states. A strong coupling between the cluster and the surface can lead to fast decoherence and relaxation into one of its ground states [119]. Approaching the atoms with a tip acts as a perturbation that induces transitions between the two ground states and gives rise to spin fluctuations in the cluster. These fluctuations have been observed in terms of random telegraph noise in time-dependent measurements [14,15]. We will show that in this regime, the spin fluctuations are reflected in the current noise and give rise to super-Poissonian shot noise.

3.4.1 Counting statistics

We showed in section 3.3 that measuring the current in STM experiments can be used to probe the spin state of an atom cluster. At the same time, the cluster spin affects the current through the cluster and it can be expected that spin fluctuations in the cluster are revealed in the current noise. In order to study the current noise, we are using an approach developed by Flindt et. al [120, 121] to obtain the shot noise and higher cumulants of the current correlator for an atom cluster. Their approach is particularly suitable for systems with large eigenspaces, where analytical expressions become cumbersome. In order to numerically evaluate the current cumulants, Flindt et al. [120] derived expressions using Rayleigh-Schrödinger perturbation theory. This method has been successfully employed to obtain zero-frequency noise of nano-electromechanical systems [120, 122]. Furthermore, the procedure has been extended to treat finite-frequency noise [123] and non-Markovian systems [124].

We will give a short introduction to the calculation of current noise and the required notation while referring to the literature for details (e.g. [121,125] and references therein). In the following, the zero-frequency current cumulants will be denoted by $\langle\!\langle I^m \rangle\!\rangle$ with the order $m = 1, 2, \ldots$ for a consistent notation. We are interested in the first three current cumulants, given by the current $\langle\!\langle I^1 \rangle\!\rangle \equiv \langle I \rangle$, the shot noise $\langle\!\langle I^2 \rangle\!\rangle \equiv S_I^{(2)}$ and the skewness of the current distribution $\langle\!\langle I^3 \rangle\!\rangle \equiv S_I^{(3)}$ corresponding to the zero-frequency limit of

$$S_I^{(3)}(\omega_1, \omega_2) = \int d(t - t')\, d(t' - t'')\, e^{-i\omega_1(t-t')-i\omega_2(t'-t'')}\, \langle \delta I(t) \delta I(t') \delta I(t'') \rangle. \tag{3.39}$$

Using the current cumulants, the Fano factors $F_2 = \langle\!\langle I^2 \rangle\!\rangle / e \langle\!\langle I^1 \rangle\!\rangle$ and $F_3 = \langle\!\langle I^3 \rangle\!\rangle / e \langle\!\langle I^2 \rangle\!\rangle$ can be defined. A common approach to obtain the current cumulants is to apply full counting statistics to obtain the cumulants of the particle operator $\langle\!\langle n^m \rangle\!\rangle$.

In order to obtain the counting statistics, we start by introducing an n-resolved Marko-

vian master equation

$$\dot{\rho}_n(t) = \sum_{n'} \mathcal{W}(n-n')\,\rho_{n'}(t), \tag{3.40}$$

where n gives the number of transferred electrons from an emitter to a collector through the sample. Then, the density matrix of the system is given by $\rho(t) = \sum_n \rho_n$. Then, the n-resolved master equation can be transformed by introducing $\rho_\chi = \sum_n \rho_n(t)\, e^{in\chi}$ into

$$\dot{\rho_\chi}(t) = \mathcal{W}_\chi\, \rho_\chi(t). \tag{3.41}$$

The relation between the cumulant generating function (CGF) and the n-resolved density matrix is established by

$$e^{-F(\chi)} = \mathrm{Tr}\,[\rho_\chi(t)] = \mathrm{Tr}\,\left[\sum_n \rho_n(t) e^{in\chi}\right], \tag{3.42}$$

where the trace is performed over the system degrees of freedom. With the knowledge of the CGF, the zero-frequency cumulants of the current are obtained through

$$\langle\!\langle I^m \rangle\!\rangle = \frac{d}{dt}\langle\!\langle n^m \rangle\!\rangle(t)\Big|_{t\to\infty} = \frac{d}{dt}\frac{\partial^m F(\chi,t)}{\partial(i\chi)^m}\Big|_{\chi\to 0, t\to\infty} \tag{3.43}$$

Flindt et al. [120] derived expressions for these cumulants by expanding $\mathcal{W}_\chi$ using Rayleigh-Schrödinger perturbation theory. Here, we summarize their findings and refer to the literature [120–122] for a detailed derivation. For the present model, $\mathcal{W}_\chi$ is given by

$$\mathcal{W}_\chi = \mathcal{W}_0 + (e^{i\chi}-1)\mathcal{I}_+ + (e^{-i\chi}-1)\mathcal{I}_-, \tag{3.44}$$

where $\mathcal{W}_0$ contains rates that do not transfer charge from the tip to the substrate and vice versa, $W^{sub-sub}$ and $W^{tip-tip}$ (cf. Eq. 3.26). The current operators $\mathcal{I}_\pm$ transfers charge from the emitter to the collector across the junction and vice versa and are associated with the rates $W^{tip-sub}$ and $W^{sub-tip}$, respectively. The current flowing through the sample can be obtained by the net flow $\mathcal{I} = \mathcal{I}_+ - \mathcal{I}_-$ and we further define the total current flow according to: $\mathcal{J} = \mathcal{I}_+ + \mathcal{I}_-$. Using these expressions, the first three current cumulants in the long-time limit read

$$\langle\!\langle I^1 \rangle\!\rangle = \langle\!\langle \tilde{0}|\mathcal{I}|0\rangle\!\rangle, \tag{3.45}$$

$$\langle\!\langle I^2 \rangle\!\rangle = \langle\!\langle \tilde{0}|\mathcal{J}|0\rangle\!\rangle - 2\langle\!\langle \tilde{0}|\mathcal{I}\mathcal{R}\mathcal{I}|0\rangle\!\rangle, \tag{3.46}$$

$$\langle\!\langle I^3 \rangle\!\rangle = \langle\!\langle \tilde{0}|\mathcal{I}|0\rangle\!\rangle - 3\langle\!\langle \tilde{0}|\mathcal{J}\mathcal{R}\mathcal{I} + \mathcal{I}\mathcal{R}\mathcal{J}|0\rangle\!\rangle - 6\langle\!\langle \tilde{0}|\mathcal{I}\mathcal{R}(\mathcal{R}\mathcal{I}\mathcal{P} - \mathcal{I}\mathcal{R})\mathcal{I}|0\rangle\!\rangle. \tag{3.47}$$

Here, the stationary states $|0\rangle\!\rangle$ and $\langle\!\langle\tilde{0}|$ are defined by

$$\frac{d}{dt}|0\rangle\!\rangle = \mathcal{W}_0\,|0\rangle\!\rangle \equiv 0 \;\text{ and }\; \frac{d}{dt}\langle\!\langle 0| = \langle\!\langle\tilde{0}|\mathcal{W}_0 = 0, \tag{3.48}$$

with $\langle\!\langle\tilde{0}|0\rangle\!\rangle = 1$. Note that $\langle\!\langle\tilde{0}|$ is not given by $\langle\!\langle 0|$ because $\mathcal{W}_0$ is not a Hermitian operator in a dissipative system. The projectors in Eq. (3.47) are given by $\mathcal{P} = \mathcal{P}^2 = |0\rangle\!\rangle\langle\!\langle\tilde{0}|$ and $\mathcal{Q} = \mathcal{Q}^2 = 1 - \mathcal{P}$. Furthermore, the pseudo-inverse $\mathcal{R} = Q\mathcal{W}_0^{-1}\mathcal{Q}$ is used, which is well-defined in the subspace corresponding to $\mathcal{Q}$. Using Eq. (3.45) - (3.47), we can numerically obtain the Fano factors $F_2 = \langle\!\langle I^2\rangle\!\rangle/e\langle\!\langle I^1\rangle\!\rangle$ and $F_3 = \langle\!\langle I^3\rangle\!\rangle/e\langle\!\langle I^2\rangle\!\rangle$ for the ferromagnetic cluster.

Spin Noise The current noise is related to the spin noise in the cluster due to magnetoresistance as well as inelastic current terms. In order to compare current noise and spin noise, we obtain the spin noise by calculating the Fourier transform

$$S_z^{(2)}(\omega) = 2\int d\tau\,\kappa(\tau)\,e^{i\omega\tau} \tag{3.49}$$

of the correlation function

$$\kappa(\tau) = \langle S_z(t+\tau)S_z(t)\rangle - \langle S_z\rangle\langle S_z\rangle. \tag{3.50}$$

Note that for the autocorrelation function the imaginary part of Eq. (3.49) vanishes. Similarly to the current noise, the spin noise is obtained through

$$\langle\!\langle S_z^2\rangle\!\rangle = -2\,\langle\!\langle\tilde{0}|S_z\mathcal{R}S_z|0\rangle\!\rangle. \tag{3.51}$$

Before we proceed to the discussion of the results for a ferromagnetic cluster, current noise and spin noise are analyzed based on the example of a two-level system.

3.4.2 Noise in a two-state system

We consider a model system that can switch between two states. The transition probability from state 1 to state 2 and vice versa during a time interval Δt is given by $\Gamma_1\,\Delta t$ and $\Gamma_2\,\Delta t$, respectively. If the transition rate Γ_1 or Γ_2 vanishes the model system becomes stable and noise goes to zero. For finite transition rates and long measurement times Δt compared to the switching time $\tau = (\Gamma_1 + \Gamma_2)^{-1}$, however, the system switches between the two states multiple times. In this regime, the dynamics of the system can be

described by a Markovian rate equation for the occupation probabilities $\mathbf{P} = (P_1, P_2)^T$

$$\dot{\mathbf{P}} = \mathcal{W}\,\mathbf{P}, \tag{3.52}$$

with

$$\mathcal{W} = \begin{pmatrix} -\Gamma_1 & \Gamma_2 \\ \Gamma_1 & -\Gamma_2 \end{pmatrix}. \tag{3.53}$$

Any initial state relaxes with the rate $\Gamma = \Gamma_1 + \Gamma_2$ to a stationary state given by the occupation probabilities $\bar{P}_1 = \Gamma_2/\Gamma$ and $\bar{P}_2 = \Gamma_1/\Gamma$. Each of the two states is associated with a current I_1 and I_2, respectively. The cumulants describing the transport statistics in this model are given by [126]

$$\langle\langle I^1 \rangle\rangle = I_1 P_1 + I_2 P_2, \tag{3.54}$$

$$\langle\langle I^2 \rangle\rangle = 2(\Delta I)^2 \Gamma_1 \Gamma_2 / \Gamma^3, \tag{3.55}$$

$$\langle\langle I^3 \rangle\rangle = 6(\Delta I)^3 \Gamma_1 \Gamma_2 \Delta\Gamma / \Gamma^5, \tag{3.56}$$

with $\Delta I = I_2 - I_1$ and $\Delta\Gamma = \Gamma_2 - \Gamma_1$. From Eq. (3.55) and Eq. (3.56) it is obvious that large values of the cumulants can be expected if the switching between the two states is slow ($\Gamma \to 0$). These results can be used to identify telegraph noise in a general system by checking the first three cumulants. Substituting Eq. (3.54) and Eq. (3.55) in Eq. (3.56) yields the following necessary condition for a bi-stability [120, 127]

$$\langle\langle I^3 \rangle\rangle = 3\langle\langle I^2 \rangle\rangle^2 \frac{\langle\langle I^1 \rangle\rangle - (I_1 + I_2)/2}{(\langle\langle I^1 \rangle\rangle - I_1)(\langle\langle I^1 \rangle\rangle - I_2)}. \tag{3.57}$$

Similarly, expressions for the spin noise $\langle\langle S_z^2 \rangle\rangle$ can be obtained by assuming that the spin fluctuates between the spin projections $S_z = \pm S$,

$$\langle\langle S_z^2 \rangle\rangle = 4\,\frac{S^2}{\Gamma}. \tag{3.58}$$

The spin noise and the second cumulant of the current noise decay with the switching rate. The current noise, however, also depends on the asymmetry between the occupation probability of the two states.

3.5 Results for a small ferromagnetic cluster

3.5.1 Random telegraph noise

In this section, we discuss the conditions leading to a slow switching of magnetization using the example of a five atom cluster. The orientation of the spins in the cluster are energetically separated by the zero-field splitting. If we assume a fast decoherence time in the cluster and neglect the transverse anisotropy, the states of the system can be decomposed into two decoupled subspaces specified by $\langle S_z \rangle > 0$ and $\langle S_z \rangle < 0$. Interaction with the surface and the STM tip connects the two subspaces and can induce a switching between subspaces. If the coupling of the cluster to the tip and surface is of the same order, an applied polarized current can drive the system between the subspaces [119]. In the limit of vanishingly small coupling to the tip, however, the system stays in one of its ground states for most of the time, with only a small probability to switch into the opposite ground state. This is the origin of telegraph noise observed in transport measurements through atomic clusters [14, 15].

Telegraph noise manifests itself in a super-Poissonian Fano factor. We have calculated the Fano factor F_2 and the zero-frequency spin noise $\langle\langle S_z^2 \rangle\rangle$ for the spin Hamiltonian (Eq. 3.1, 3.3) to model a 5 Fe-atoms cluster with an effective total spin $^{15}/_2$. An axial anisotropy of $D = -0.1$ meV obtained from the experiment [15] energetically separates the spin subspaces. Without transverse anisotropy E, the eigenstates of the system can be labeled by $|S_z\rangle$ with $S_z = -^{15}/_2 \ldots {}^{15}/_2$.

With a finite transverse anisotropy $E = 0.02$ meV measured in experiments, however, eigenstates become superpositions of $|S_z\rangle$ with coefficients shown in Fig. 3.3. The two ground states, which will be labeled $|g_+\rangle$ and $|g_-\rangle$, receive only small contributions from states $|S_z| < S$, while energetically higher states receive large contributions from different S_z states.

For these parameters, we obtain a colossal Fano factor F_2 when the coupling to the STM tip becomes small ($v_T/v_S = 0.1$; see Fig. 3.4). The large Fano factor suggests random telegraph noise due to the slow switching between the ground states of the cluster which resembles an effective two-level system. In this regime, the occupation probability of excited states is small due to fast spin relaxation. Increasing the bias voltage or the coupling to the tip reduces the Fano factors, implying that excited states are increasingly occupied. To check these claims, the Fano factor F_3 is compared with the condition Eq. (3.57) that indicates an effective two-level system (Fig. 3.4 right). While the results for F_3 match the Fano factor of a two-level system for $v_T/v_S = 0.1$

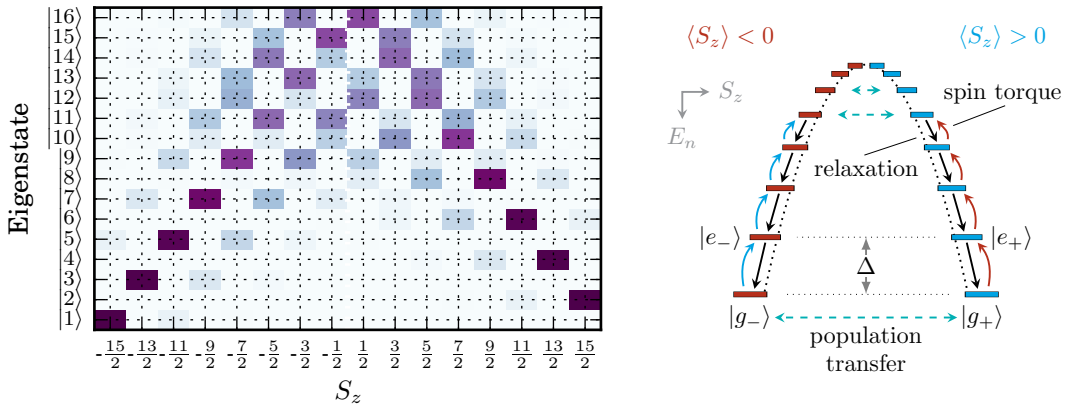

Figure 3.3: The coefficients $|c_i|^2$ (left; the darker the color the larger the values) obtained from the expansion of the eigenstates $|i\rangle$ in $|S_z\rangle$ states, $|i\rangle = \sum_i c_i|S_z\rangle$. The eigenstates, $|i\rangle$, are ordered from low to high energy and demonstrate that the higher states receive contributions from many different $|S_z\rangle$. The right figure shows the eigenstates arranged to resemble the anisotropy barrier together with transition rates described in the text.

in the range of considered voltages, deviations occur for $v_T/v_S > 0.1$ at higher voltages. The deviations imply that the spin is driven into excited states, and the current noise in this range does not originate from a bistability of an effective two-level system.

Before we begin with further discussions of results for the noise, we introduce effective rates contributing to the dynamics of the spin which are derived from the rates in the master equation Eq. (3.26). In an atom with an odd spin, two ground states exist according to Kramers theorem, which are separated by an energy barrier resulting from the zero-field splitting [92]. The energy landscape of the atom resembles a double well and a transition between each side can occur by coherent tunneling through the barrier or by driving the system over the barrier. Coherent tunneling in atoms interacting with their surrounding, however, is suppressed if the tunneling time is larger than the dephasing time. In this case, the surface acts as a measuring device and destroys coherences [119]. In the present study, we assume fast decoherence due to the strong coupling to the surface which allows for the use of the master equation for only the diagonal elements of the density matrix.

We find that the switching between the two ground states of the system is mainly determined by three rates associated with magnetization tunneling, inelastic excitation and magnetic relaxation. The interaction with the surface induces magnetization tunneling between the two ground states if a finite transverse anisotropy E is present. The

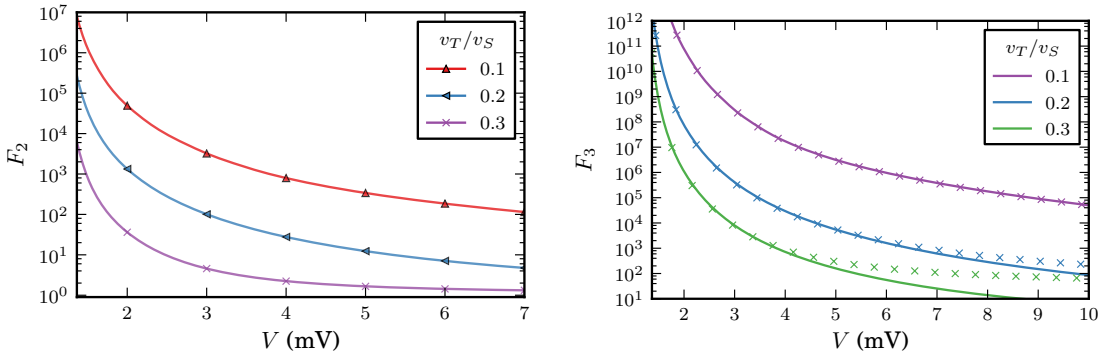

Figure 3.4: Fano factor F_2 (left) for a small ferromagnetic cluster with total spin $S = 15/2$, $D = -0.1$ meV and $E = 0.02$ meV at $T = 0.5$ K ($U/J = 3$). The bias voltage V is chosen larger than the magnetic excitation energy Δ when inelastic transitions set in. The Fano factor F_3 (right) is shown for the small cluster (solid lines) and a two-level system (crosses).

corresponding rate γ_{tunnel} for switching between the ground states $|g_\pm\rangle$ reads

$$\gamma^{\pm}_{tunnel} = \Gamma_{S,S}\; k_B T\; |\langle g_-|S_-|g_+\rangle|^2 + \Gamma_{S,T}\; \frac{1 \pm \mathcal{P}_T}{2}\; \zeta(|eV|)\; |\langle g_-|S_-|g_+\rangle|^2. \tag{3.59}$$

The origin of this kind of magnetization tunneling is the interplay of transverse anisotropy and exchange interaction with surface and tip electrons. Approximating the magnetization tunneling by $\gamma^{+}_{tunnel} + \gamma^{-}_{tunnel} \approx \Gamma_{S,S}\; k_B T\; (E/D)^{2S-1}$ reveals that the rate becomes exponentially small for large spins because $|E/D| < 1/3$. Further, a linear temperature dependence becomes apparent. The asymmetry between these rates, $\gamma^{+}_{tunnel} - \gamma^{-}_{tunnel} \approx \Gamma_{S,T}\, \mathcal{P}_T\, (E/D)^{2S-1}\, |eV|$, depends on the spin polarization of the current and is linear in bias V.

Finally, we discuss two contributions accounting for the excitation and de-excitation of the atoms. A spin-polarized current drives the spin out of equilibrium and induces transitions from the ground state $|g_\pm\rangle$ to the first excited state $|e_\pm\rangle$ with the rate

$$\gamma^{\pm}_{inel} = \Gamma_{S,T}\; \frac{1 \pm \mathcal{P}_T}{2}\; \zeta(\Delta - eV)\; |\langle e_\pm|S_\mp|g_\pm\rangle|^2. \tag{3.60}$$

The pumping into excited states is exponentially suppressed for bias voltages smaller than the spin excitation energy. If the bias is increased, inelastic driving of the spin sets in and $\gamma^{\pm}_{inel}$ becomes linear in bias V. The atoms can dissipate energy by interacting

with electrons in the tip and surface

$$\gamma_{relax} = (\Gamma_{S,S} + \Gamma_{T,T})\ \zeta(|\Delta|)\ |\langle g_+|S_+|e_+\rangle|^2. \tag{3.61}$$

It has been found that a strong hybridization of the cluster with the surface can lead to relaxation times in the order of picoseconds [27].

The transitions induced by the different rates are schematically shown for a spin $S = {}^{15}/_{2}$ in Fig. 3.3. If the coupling of the STM tip to the atoms is weak, the cluster switches between the two ground states and develops characteristics of a two-level fluctuator [15, 126]. The following simplified model will be used to interpret the results of the current noise and spin noise. Switching between the two ground states $|g_\pm\rangle$ occurs by either magnetization tunneling γ_{tunnel} or by inelastic excitation γ_{inel} to an intermediate level $|e\rangle$. Any transient occupation of $|e\rangle$ relaxes into one of the two ground states with the large rate γ_{relax}. The rate for the switching between $|g_+\rangle$ and $|g_-\rangle$ is given by

$$\begin{aligned}\Gamma \;=\; & \gamma^+_{inel} + \gamma^-_{inel} + \gamma^+_{tunnel} + \gamma^-_{tunnel} + 2\gamma_{relax} \\ & -\sqrt{\left(\gamma^+_{inel} - \gamma^-_{inel} + \gamma^-_{tunnel} - \gamma^+_{tunnel}\right)^2 + 4\left(\gamma_{relax} - \gamma^+_{tunnel}\right)\left(\gamma_{relax} - \gamma^-_{tunnel}\right)}\end{aligned} \tag{3.62}$$

If the asymmetry between rates $\frac{\gamma^+ - \gamma^-}{\gamma^+ + \gamma^-}$ is negligible because the spin polarization $\mathcal{P}_T$ of the current and the anisotropy $|E/D|$ are small, the rates simplify to

$$\Gamma \;=\; \gamma^+_{inel} + \gamma^-_{inel} + \gamma^+_{tunnel} + \gamma^-_{tunnel}. \tag{3.63}$$

In the limit of large U/J, the shot noise is associated with the spin noise because the main contribution to the current originates from the magneto-resistance. The time-dependent current I is proportion to the spin of the atoms: $I \propto \langle S_z\rangle + \mathcal{O}(J^2/U^2)$. Then, the spin dynamics are reflected in the current dynamics $\langle I(t)I(t')\rangle \propto \langle S_z(t)S_z(t')\rangle\langle I_z(t)I_z(t')\rangle$ [128].

In Fig. 3.5 we compare the spin noise for different transverse anisotropy values. Two regimes become apparent when the bias voltage is below and above the spin excitation energy Δ, respectively. For a bias voltage $e|V|$ below the energy Δ, inelastic excitation of the spin is exponentially suppressed. However, switching is possible due to the interplay between electrons and transverse anisotropy that leads to a small rate of magnetization tunneling. The switching rate can be approximated by

$$\Gamma \approx \gamma^+_{tunnel} + \gamma^-_{tunnel} \propto k_B T, \tag{3.64}$$

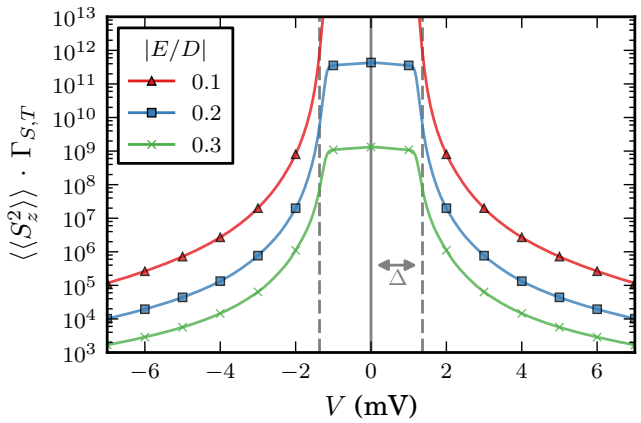

Figure 3.5: The zero-frequency spin noise $\langle\langle S_z^2 \rangle\rangle$ develops a plateau for bias voltage V below the spin excitation energy Δ due to a finite transition probability γ_{tunnel}. At $V > \Delta$, inelastic excitation of the cluster sets in and the spin noise decays with $|V|^{-1}$.

which is only weakly bias dependent due to the polarization $\mathcal{P}_T = 0.1$.

For a bias voltage near the excitation energy, inelastic excitation of the atoms sets in and the switching rate increases proportional to the bias voltage

$$\Gamma \approx \gamma^+_{inel} + \gamma^-_{inel} \propto eV, \tag{3.65}$$

and spin noise decays with $|V|^{-1}$ for a large bias $|V| \gg \Delta$. Inelastic tunneling leads to excitation of the cluster and a higher switching rate between the ground state.

Transverse anisotropy E induces magnetization tunneling not only between ground states but also between each degenerate level. A larger E decreases the overall magnitude of spin noise in the regime $|V| > \Delta$ by enhancing the switching rate (Fig. 3.5). In the regime $|V| < \Delta$, the transverse anisotropy limits the stability of the atom as it induces transitions between the states on the time scale $(\gamma^+_{tunnel} + \gamma^-_{tunnel})^{-1}$.

The current noise in the large U/J case reflects the spin noise as the elastic current gives the main contribution to the current. In the opposite limit $U \to 0$, the inelastic rates define the current. The Fano factor F_2 for $|E/D| = 0.2$ in Fig. 3.6 shows for intermediate values of U/J several distinctions from the spin noise. For a bias voltage above the spin excitation energy, the Fano factor decays in a way that is similar to the decay of the spin noise, whereas F_2 is not symmetrical under bias reversal. The interference between direct and exchange terms in the tunneling leads to odd and even terms in the current which results in the asymmetry in the Fano factor. In the bias regime below Δ, the asymmetry

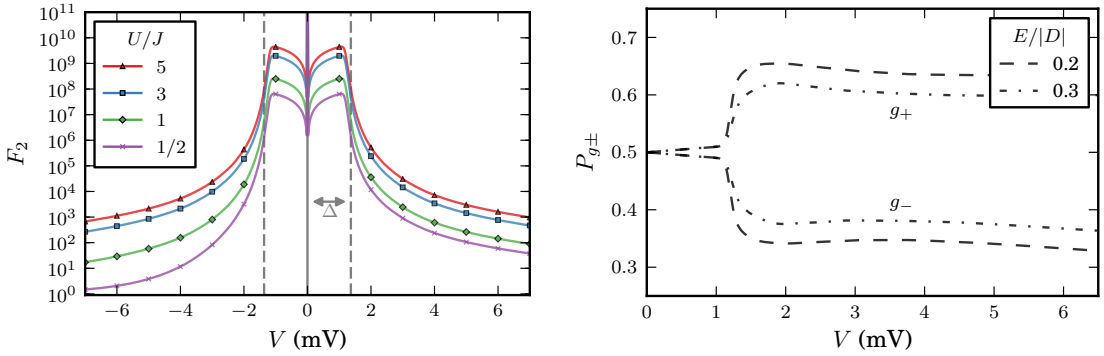

Figure 3.6: Left: Fano factor F_2 for different ratios U/J between direct and exchange tunneling rate exhibits an asymmetry under bias reversal. Right: voltage-dependent occupation $P_{g_\pm}$ of the two ground states g_+ and g_- for different anisotropy values.

is absent because inelastic current is suppressed and the current noise originates only from the direct tunneling terms. However, the plateau seen in the spin noise for $V < \Delta$ is not reflected in the Fano factor. While the spin noise is proportional to the switching time, the Fano factor also incorporates the occupation probabilities of the ground state. The occupation probabilities in Fig. 3.6 show an asymmetry for $V < \Delta$ due to the rate $\gamma^+_{tunnel} - \gamma^-_{tunnel} \propto eV$, which lead to the shape of F_2.

The findings show that the spin noise is reflected in the noise of the current through the ferromagnetic cluster. In distinct parameter regimes, the noise indicates a bistable system originating in the slow switching between the ground states of the cluster governed by inelastic excitation and magnetization tunneling. In particular, magnetization tunneling turned out to be a limiting factor for the stability of the cluster for bias voltages below the magnetic excitation energy.

3.5.2 Magnetization tunneling

A common approach to describe switching in experiments on larger magnetic systems, like nanoislands containing few 100 iron atoms, is the Néel-Brown theory which describes the switching by an Arrhenius law [129–131]. The magnetic system is reduced to two states in a double well which represent the two stable orientations of the magnetic moment due to the magnetic anisotropy. The rate Γ to overcome the barrier exponentially depends on the barrier's energy E_b and temperature T according to

$$\Gamma = \Gamma_0 \exp\left(-\frac{E_b}{k_B T}\right), \tag{3.66}$$

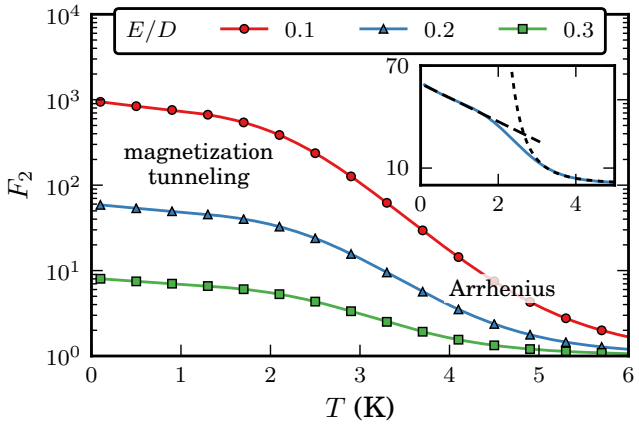

Figure 3.7: The Fano factor F_2 shows the transition between magnetization tunneling and Arrhenius-type switching behavior for different temperature T. The inset depicts the data for $E = 0.02$ meV and $D = -0.1$ meV using a linear scale.

with the attempt rate Γ_0. In this framework, the spin-polarized current can be introduced by modifying the parameters. The exerted spin-transfer torque leads to an effective barrier energy $E_b \pm \Delta E$ [29]. The parameters ΔT and ΔE depend on the current and can be determined by measuring the telegraph noise [14, 29].

In the following, we will show that in small magnetic clusters the switching at low temperatures significantly deviates from Néel-Brown theory. Remarkably, the low-temperature behavior indicates the presence of electron-mediated magnetization tunneling of the spin through the anisotropy barrier.

Fig. 3.7 shows the temperature dependence of the shot noise for $V = 5$ meV and different ratios of the anisotropy $|E/D|$. The Fano factor F_2 exhibits a linear dependence in the low-temperature range, $T < 2$ K, and strongly decays for larger temperatures. The exponential tail for temperatures $T > 2$ K indicates Arrhenius behavior and originates from the influence of the electrons in the surface. The cluster cannot only dissipate energy through the interaction with the surface atoms, but can also be thermally excited. The corresponding rates (Eq. 3.27) depend on the spin excitation energy Δ and are proportional to $\zeta(-|\Delta|) \propto n_B(|\Delta|)$, with n_B being the Bose distribution function. At high temperatures, these rates are proportional to $\exp(-|\Delta|/k_BT)$ and are responsible for Arrhenius behavior.

The low-temperature behavior of F_2 can be attributed to the interplay between tunneling electrons and anisotropy. Inelastic excitation is not responsible for the linear dependence because the rate $\gamma_{inel} \propto \zeta(eV - \Delta) \approx eV - \Delta$ is independent of temperature

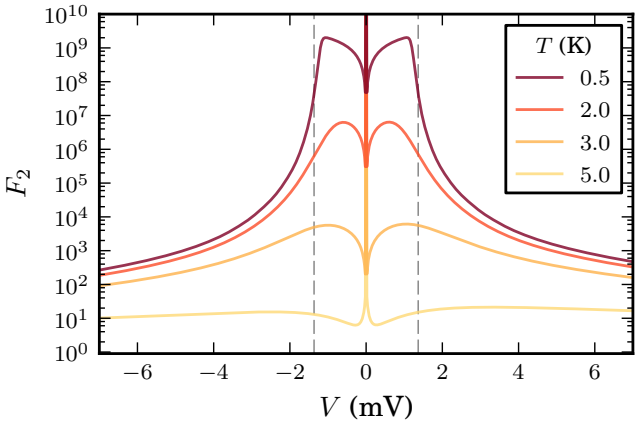

Figure 3.8: Temperature dependence of the Fano factor F_2, dashed lines indicate the spin-excitation energy Δ. The overall magnitude of the Fano factor decreases with temperature due to an enhancement of the switching rate.

for large bias $eV > \Delta$. However, the interaction of the atoms with surface electrons leads to a transfer of the spin through the anisotropy barrier with the rate

$$\gamma_{tunnel} \propto k_B T \, (E/D)^{2S-1}, \tag{3.67}$$

which reduces the time between switching events and explains the low-temperature behavior. This result is remarkably different from coherent quantum tunneling of magnetization (QTM), which is temperature independent [14, 132].

The bias dependence of the Fano factor (Fig. 3.8) illustrates that the temperature reduces the overall current noise by increasing the switching frequency. Temperature also blurs the crossover between the regimes in which magnetization tunneling dominates the switching behavior and the regime of inelastic excitation of the spin. Temperature-assisted inelastic excitation already sets in at bias voltages of $|eV| < \Delta$.

These results demonstrate the importance of the electron-mediated magnetization tunneling through the anisotropy barrier for the description of spin switching at low temperatures.

3.5.3 Interplay between spin-transfer torque and magnetic fields

In a next step, we discuss the effect of an external magnetic field B that modifies the system. A magnetic field along the easy axis of the cluster shifts the energies of the system by the Zeeman term (Eq. 3.1). Specifically, the Zeeman energy lifts the two-fold

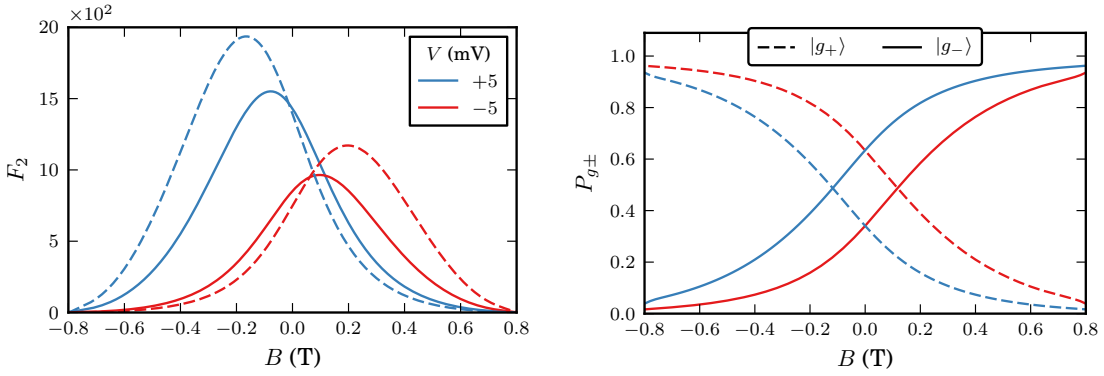

Figure 3.9: The maximum of the Fano factor F_2 (left) shows a dependence on the bias polarity ($D = -0.1$ meV, $E = 0.02$ meV and $g = 2$). Compared to the case of $\mathcal{P}_T = 0.1$ (solid lines), the maxima shift to larger values of $|B|$ for $\mathcal{P}_T = 0.2$ (dashed lines; scaled by 1/3). The right figure shows the occupation probabilities of the two lowest energy states $|g_-\rangle$ and $|g_+\rangle$ for the same bias values as in the left figure.

degeneracy of the states in the cluster and leads to a single, non-degenerate ground state. If the magnetic field has a transversal component, the eigenstates receive admixtures of different S_z states similar to the effect of the transverse anisotropy. In this case, quantum tunneling of magnetization (QTM) can occur in systems with an even spin [132]. In the cluster with an odd spin, however, QTM is forbidden and therefore we will assume only a longitudinal component of the magnetic field.

Fig. 3.9 shows the magnetic field dependence of the shot noise with a constant bias voltage $V = 5$ mV. A maximum of the shot noise develops for a finite magnetic field that shifts under bias reversal. The shot noise is governed by two competing mechanisms. On the one hand, the magnetic field induces a polarization of the cluster. On the other hand, the spin-polarized current drives the system between the two ground states and creates an asymmetry between the states due to the polarization $\mathcal{P}_T$ of the tip electrons.

The maximum of the shot noise occurs at a B-field value where the effect of the magnetic field is compensated by the spin-polarized current flow. The effective rate for switching is given by

$$\Gamma \approx \gamma^{+}_{inel}(B) + \gamma^{-}_{inel}(B). \tag{3.68}$$

The value B_{comp}, for which the two mechanisms compensate each other, can be approximated through $\gamma^{+}_{inel}(B_{comp}) = \gamma^{-}_{inel}(B_{comp})$, yielding

$$g\,\mu_B\,B_{comp} \approx \pm\mathcal{P}_T\,\frac{|\Delta| - eV}{2S-1}, \tag{3.69}$$

where the sign depends on the direction of the current flow, and any transverse anisotropy E is neglected. The switching time drops with $|B|^{-1}$ when the absolute value of the magnetic field is increased towards ±0.8 T. One of the two former ground states $|g_{\pm}\rangle$ becomes the only ground state of the cluster and the probability to switch into other states is small (Fig. 3.9 right).

For a magnetic field B_{comp}, the probabilities of occupying the two lowest energy states $|g_{+}\rangle$ and $|g_{-}\rangle$ are equal (Fig. 3.9 right). Furthermore, the probability of occupying $|g_{+}\rangle$ or $|g_{-}\rangle$ exhibits a different shape when reversing the bias. The separation between the probabilities for $V = +5$ meV and $V = -5$ meV can be measured in experiments [15] and serves as evidence for spin-transfer torque exerted by the spin-polarized current.

3.6 Summary

We have studied the spin noise in a ferromagnetic cluster coupled to a spin-polarized tip and a conducting substrate. Using a spin Hamiltonian and a master equation approach revealed that the dynamics of the spin fluctuations in the cluster are determined by the interplay of spin flips due to a spin-polarized current, magnetic relaxation and substrate-mediated magnetization tunneling.

We have shown that the bias-dependent current noise in the regime of weak coupling between cluster and tip originates from the dynamical switching between the two ground states of the system. The current cumulants resemble the statistics of an effective two-level system. Furthermore, the spin noise is reflected in the current noise when the current is mainly determined by elastic cotunneling. We find that the bias-dependent Fano factor decays for bias voltages above the magnetic excitation energy due to current-induced spin flips in the cluster and the resulting strong spin fluctuations. The occurrence of a threshold bias demonstrates the quantized nature of the spin in the system under study. For bias voltages below the magnetic excitation energy, the excitation of the cluster is suppressed at low temperatures. However, spin fluctuations can still be persistent in clusters of finite transverse anisotropy E due to substrate-electron assisted magnetization tunneling through the anisotropy barrier.

Subsequently, we studied the temperature dependence of spin fluctuations. For temperatures above the spin excitation energy, the cluster is thermally excited and the spin fluctuation corresponds to an Arrhenius-type spin switching. At low temperatures, however, thermal excitations are suppressed and we find that spin fluctuations are caused by the interplay of substrate electrons and transverse magnetic anisotropy which leads to magnetization tunneling. In this regime, spin fluctuations linearly dependent on the

temperature, which can serve as an experimental indicator for magnetization tunneling.

Furthermore, the introduction of a magnetic field reveals the effect of spin-transfer torque due to a spin-polarized current on the spin dynamics in the cluster. The polarization of the tip introduces an imbalance between current-induced spin-flips associated with the increasing and decreasing of the cluster spin, respectively. This effect of the spin-polarized current on the dynamics of the cluster spin is related to the influence of an effective magnetic field. We find that the competition between current-induced spin-transfer torque and an external magnetic field determines the occupation of two lowest energy states of the cluster. At a particular value of the magnetic field strength B_{comp} the interactions are balanced, which leads to two equally occupied lowest energy states and a maximal Fano factor. This value of the magnetic field depends on the polarization of the tip, the cluster spin, the magnetic excitation energy and applied voltage, and can serve as a tool to determine unknowns in the experiment.

This page intentionally left blank.

4 Non-equilibrium Quantum Monte Carlo

In the preceding chapters, we dealt with the dynamics of small nanostructures by employing the master equation approach, which was adequate for the experimental parameter regime. This perturbative method relies on the Markovian approximation and weak tunnel coupling [16,49,133]. Recently, the theoretical treatment of non-equilibrium transport through strongly correlated systems gained great attention for cases in which no small parameter is present [30–32, 134–138]. In this deep quantum regime, methods are necessary that go beyond a purely perturbative treatment of the problem and which are crucial for the description of advanced experiments ranging from transport and pump-probe spectroscopy on nanostructures and bulk systems to the spectroscopy of cold atoms in optical lattices [13, 139–142].

Several numerical approaches have been developed to treat coherent non-equilibrium dynamics and are often applied to the quantum (Anderson) impurity model serving as a reduced representation of quantum dots, single molecules or adatoms on surfaces. The impurity model consists of a finite-dimensional system exhibiting a single bound level tunnel coupled to an infinite system of two non-interacting electron baths. Numerical renormalization-group (RG) techniques have proven to provide an accurate treatment of non-equilibrium dynamics of the impurity model and to capture essential features [143–146]. However, the representation of the bath by a finite lattice can lead to the occurrence of finite size effects, which limit the propagation time and the energy scales that can be accessed.

Another class of approaches is based on the path integral sampling technique, originally introduced in the context of quantum chemistry [147]. In the iterative summation of path integrals (ISPI) [21, 22, 148], the path integral expansion is performed in terms of the quantum dot Coulomb interaction while the influence path integral technique (INFPI) relies on the expansion in the tunnel coupling [20, 149]. In both versions, the property of a finite 'memory time' in the leads is exploited in which electronic correlations exponentially decay on a time scale defined by the temperature and bias voltage. Therefore, these methods are restricted in their parameter regime and, in particular, do not allow to approach the zero bias and temperature regime.

In this chapter, we will give an introduction to the real-time quantum Monte Carlo (QMC) approach, which is based on the stochastic sampling of the diagrammatic path integral expansion for the Keldysh partition function [30, 31, 134]. Originally developed for the computation of equilibrium properties, QMC has been shown to be versatile in accessing a wide range of parameters and very flexible for the treatment of various systems [32, 150–152]. We are going to discuss two flavors of QMC that depend on the expansion of the Keldysh partition function either in the Coulomb interaction (weak coupling) or in the coupling of the quantum dot to the bath (strong coupling). The naming, weak-coupling and strong-coupling QMC, has historically developed and refers to interaction of the electrons on the quantum dot [152].

The weak-coupling QMC method for non-equilibrium has recently been applied by Werner et al. [32, 151] to study the dynamics of the impurity model when initially prepared in a non-equilibrium but non-interacting state and switching on the interaction at $t = 0$ [153]. This so-called interaction quench can be applied to model time-resolved experiments on ultracold atoms in (periodically) driven optical lattices [154, 155]. Furthermore, it has been successfully used to investigate dynamics of the impurity model after a voltage quench and for coupling to superconducting leads [32, 137, 138].

The strong-coupling QMC approach has been implemented by Mühlbacher et al. [30] and Schiro et al. [134, 135] for non-interacting quantum dots in non-equilibrium coupled to electron and phonon reservoirs. The method has also been applied to dynamics of an initially isolated quantum dot after the coupling to electron baths was switched on at time $t = 0$ [31, 32, 136].

With both methods, numerically exact results can be obtained for a wide range of parameter regimes, even at zero temperature and zero bias. However, these approaches are restricted to finite time simulations due to the dynamical sign problem. The contributions to the estimates of expectation values in real-time QMC are oscillatory due to the dynamical phase acquired during the propagation of the simulated system in time and can partially cancel each other. In order obtain reliable results and a satisfactory signal-to-noise ratio, the stochastic error has to be minimized. This task becomes exponentially difficult for long simulated times.

In the following methodological introduction, we compare the dynamical sign problem in the implementations of strong-coupling and weak-coupling QMC. In contrast to the weak-coupling approach previously applied to non-equilibrium [32, 151], which relies on the expansions of a Hubbard-Stratonovich field, we adopt the real-time version of the expansion in the Coulomb interaction term orginally developed by Rubtsov et al. for equilibrium [150]. The implementation of weak-coupling QMC relies on the introduction

of auxiliary parameters that can be exploited to reduce the sign problem. Furthermore, we implement the weak-coupling approach for an initially prepared quantum dot for which the tunnel coupling to electron baths is switched on at $t = 0$. This permits us to directly compare the advantages and limitations of strong-coupling and weak-coupling QMC for the same system and parameters.

4.1 Quantum Monte Carlo for non-equilibrium transport

We introduce the two versions of the real-time quantum Monte Carlo approach for the example of transport through a single-level quantum dot (impurity model). The spin-degenerate quantum dot is tunnel coupled to two electron baths (leads) and the entire system is described by the Hamiltonian

$$H = H_{dot} + H_{bath} + H_{tunnel}. \tag{4.1}$$

The single-level quantum dot with Coulomb interaction can be occupied by up to two electrons and is given by

$$H_{dot} = \varepsilon_d \left(n_\uparrow + n_\downarrow\right) + U\, n_\uparrow n_\downarrow, \tag{4.2}$$

with the single-particle energy ε_d, the Coulomb energy U and the particle operator n_σ for an electron with spin $\sigma = \{\uparrow, \downarrow\}$. The leads are described by free electron baths

$$H_{bath} = \sum_{\alpha,k,\sigma} \left(\varepsilon_{\alpha,k,\sigma} - \mu_\alpha\right) c^\dagger_{\alpha,k,\sigma} c_{\alpha,k,\sigma}, \tag{4.3}$$

with the operators $c^{(\dagger)}_{\alpha,k,\sigma}$ that annihilate (create) an electron with momentum k and spin σ in the left (right) leads $\alpha = L(R)$. Quantum dot and leads are coupled by the tunnel Hamiltonian

$$H_{tunnel} = \sum_{\alpha,k,\sigma} t_{\alpha,k} c^\dagger_{\alpha,k,\sigma} d_\sigma + H.c., \tag{4.4}$$

with operators $d^{(\dagger)}_\sigma$ annihilating (creating) a spin-σ electron in the quantum dot. In the following, we assume an infinite number of electrons in the leads. Furthermore, we require the leads to be initially in equilibrium, resulting in the following correlation function of the bath operators

$$\langle a^\dagger_{\alpha,k,\sigma} a_{\alpha,k,\sigma} \rangle = f\left(\varepsilon_{\alpha,k,\sigma} - \mu_\alpha\right) \delta_{\alpha,\beta}\, \delta_{k,k'}\, \delta_{\sigma,\sigma'}, \tag{4.5}$$

with the Fermi function $f(x) = [\exp(x/k_BT) + 1]^{-1}$ and temperature T. A bias voltage V can be applied between the leads, which defines the chemical potentials $\mu_L = V/2$ for the left lead and $\mu_R = -V/2$ for the right lead. The level broadening $\Gamma = \Gamma_R + \Gamma_L$ with

$$\Gamma_\alpha = \pi \sum_k |t_{\alpha,k}|^2 \, \delta(\omega - \varepsilon_{\alpha,k}) \tag{4.6}$$

and the Coulomb interaction strength U define the transport regime. A distinction is made between the strong-coupling regime ($U \gtrsim \pi\Gamma$) and the weak-coupling regime ($U \lesssim \pi\Gamma$).

The aim of real-time quantum Monte Carlo is to compute the expectation value $\langle \mathcal{O}(t) \rangle$ of an operator $\mathcal{O}$ at time t given by

$$\langle \mathcal{O}(t) \rangle = \mathrm{Tr}\left[\exp\left(i \int_0^t dt' H(t') \right) \mathcal{O} \exp\left(-i \int_0^t dt' H(t') \right) \rho_0 \right], \tag{4.7}$$

with ρ_0 being the density matrix of the system at time $t = 0$. If we assume that the quantum dot and the leads are separated at $t = 0$, the density matrix splits into

$$\rho_0 = \rho_{bath} \otimes \rho_{dot}(t = 0), \tag{4.8}$$

with the quantum dot initially in a state given by $\rho_{dot}(t = 0)$ and the electron bath in equilibrium, $\rho_{bath} = \exp(-H_{bath}/k_BT)$. In the present study, the system is brought out of equilibrium by switching on the tunnel coupling at $t = 0$. The methods presented in this chapter, however, can be straightforwardly generalized to treat other situations like time-dependence of the system Hamiltonian. The general approach is to split the system Hamiltonian into two terms, H_0 and H_1, where the time evolution of H_0 can be treated exactly. The time evolution of the full system is then obtained by a formal perturbation expansion in H_1. In case of the partition function, this results in

$$\begin{aligned} Z = \mathrm{Tr}\Bigg[\sum_m i^m \int_0^t d\tilde{t}_1 \ldots \int_{\tilde{t}_{m-1}}^t d\tilde{t}_m H_1(\tilde{t}_1) \ldots H_1(\tilde{t}_m) \\ \times \sum_n (-i)^n \int_0^t dt_1 \ldots \int_{t_{n-1}}^t dt_n H_1(t_n) \ldots H_1(t_1) \, \rho_0 \Bigg], \end{aligned} \tag{4.9}$$

with $H_1(t)$ given in the interaction picture with respect to H_0. In order to evaluate this multi-dimensional time integral, the Monte Carlo (MC) algorithm is employed. In a nutshell, the Monte Carlo method is a stochastic algorithm capable of numerically evaluating (multi-dimensional) integrals. In the following, we give a rough overview over

the ordinary Monte Carlo algorithm while referring to the literature for details [156–159].

The approach, also denoted as Monte Carlo integration, evaluates (multi-dimensional) integrals by randomly sampling elements of a configuration space (or integration domain). A multi-dimensional definite integral can be approximation by

$$\frac{1}{V}\int_V f(\bar{x})\,d\bar{x} \approx \lim_N \frac{1}{N}\sum_{i=1}^{N} f(\bar{x}_i), \tag{4.10}$$

with randomly chosen elements $\bar{x}_i$ of a configuration space C with volume V. In the case of real-time quantum MC, the algorithm samples the partition function and other time-dependent observables by generating configurations given by different orders in H_1 (cf. Eq. 4.9) and associated times, i.e. different configurations on the Keldysh contour. Subsequently, the contribution of each configuration to the integral is summed up. With this approach, QMC performs a summation over all expansion orders in Eq. (4.9) as well as the time integration over the contour. The efficiency of MC lies in the particular strategy to stochastically generate different configurations called importance sampling [156, 157]. The expectation value over a configuration space, for example, can be expressed by

$$\langle\mathcal{O}\rangle = \frac{1}{Z}\int \mathcal{O}(\bar{x})\,\rho(\bar{x})\,d\bar{x} = \frac{\int \mathcal{O}(\bar{x})\,\rho(\bar{x})\,d\bar{x}}{\int \rho(\bar{x})\,d\bar{x}}. \tag{4.11}$$

To each configuration, weights

$$w = \frac{\rho(\bar{x})}{\int \rho(\bar{x})\,d\bar{x}}, \tag{4.12}$$

can be assigned. The importance sampling algorithm generates configurations based on the probability distribution given by the weights w. The Metropolis-Hastings algorithm is an implementation that incorporates the importance sampling by generating a Markov chain of configurations distributed according to a given probability function [157, 160]. In each step of the random walk, a configuration is generated and accepted or rejected with a probability given by the change of the weights (Eq. 4.12) associated with the move. Thus, the random walk samples the important regions of the configuration space, i.e. the dominant contributions to the integral. During the random walk through the configuration space, the value of the observable $\mathcal{O}$ for the particular configuration $\bar{x}$ is accumulated.

Compared to deterministic methods, MC can be more efficient, but is accompanied by the deficiency of introducing a stochastic error. The error can be reduced by running the algorithm multiple times, even though the numerical expense increases considerably

if the integrand is oscillatory. In this case, the weights are rewritten into

$$w = \frac{|\rho(\bar{x})|}{\int |\rho(\bar{x})|\, d\bar{x}}, \tag{4.13}$$

in order to represent a probability distribution (see also later discussions and Eqn. 4.24 and 4.39). The expectation value is then given by

$$\langle \mathcal{O} \rangle = \frac{\langle \mathcal{O}(\bar{x})\ \arg(w) \rangle_{|w|}}{\langle \arg(w) \rangle_{|w|}}, \tag{4.14}$$

where $\langle \ldots \rangle_{|w|}$ denotes the MC average over configurations sampled according to the distribution function $|w|$ (cf. Eq. 4.10). If the phase of the weight $\arg(w)$ is highly oscillatory, the evaluation of the integrands results in small values that are difficult to estimate due to the inherent statistical error.

Oscillatory integrands, for example, occur in fermion systems where a permutation of particle coordinates induces a sign change of the wave function known as fermion sign problem [157, 160]. The integrand can give contributions of the same order in their absolute value but with opposite sign, which can almost cancel each other leading to small contributions to the integral. It has been shown that the fermion sign problem is a NP-hard problem and the numerical effort increases exponentially with particle number, interactions and decreasing temperature [161]. Only in special cases where the symmetry of the system can be exploited, a reduction of the sign problem has been achieved [150, 159, 162].

In the non-equilibrium version of the quantum Monte Carlo approach, an additional sign problem occurs due to the dynamical phase acquired in time. This is denoted as dynamical sign problem. In the present chapter, we will explore in which limits the real-time quantum Monte Carlo method can give reliable results and introduce certain options to deal with the dynamical sign problem.

4.1.1 Expansion in the tunnel coupling

Strong-coupling quantum Monte Carlo is based on the diagrammatic expansion of the system's partition function in powers of the tunnel coupling. Originally introduced for equilibrium systems, several implementations for non-equilibrium transport through impurity models have been recently developed [30, 134, 151]. In this approach, the interaction representation with respect to the tunnel coupling is employed and the Hamiltonian of the decoupled system $H_0 = H_{dot} + H_{lead}$ gives the time evolution of operators. Then,

the Monte Carlo algorithm samples the expansion of the non-equilibrium partition function

$$Z = \mathrm{Tr}\left[\left(\tilde{T}e^{i\int_0^t dt' H_{tunnel}(t')}\right) e^{i(H_{dot}+H_{lead})t}\, e^{-i(H_{dot}+H_{lead})t} \left(Te^{-i\int_0^t dt' H_{tunnel}(t')}\right) \rho_0\right] \tag{4.15}$$

which, by definition, is $Z = 1$ if the initial density matrix is normalized. The expansion of the partition function in order of the tunnel Hamiltonian reads

$$\begin{aligned} Z = \mathrm{Tr}\Bigg[&\sum_m i^m \int_0^t d\tilde{t}_1 \ldots \int_{\tilde{t}_{m-1}}^t d\tilde{t}_m H_{\mathrm{tunnel}}(\tilde{t}_1)\ldots H_{\mathrm{tunnel}}(\tilde{t}_m) \\ &\times \sum_n (-i)^n \int_0^t dt_1 \ldots \int_{t_{n-1}}^t dt_n H_{\mathrm{tunnel}}(t_n)\ldots H_{\mathrm{tunnel}}(t_1)\,\rho_0\Bigg]. \end{aligned} \tag{4.16}$$

The particle number and spin in the bath are conserved quantities, which implies an equal number of creation and annihilation operators for the bath. Separating the trace over bath and quantum dot degrees of freedom gives

$$\begin{aligned} Z = &\sum_{m_\sigma+n_\sigma=m'_\sigma+n'_\sigma} \prod_\sigma i^{m_\sigma+m'_\sigma}(-i)^{n_\sigma+n'_\sigma} \\ &\times \int_0^t d\tilde{t}_1^\sigma .. \int_{\tilde{t}^\sigma_{m_\sigma-1}}^t d\tilde{t}^\sigma_{m_\sigma} \int_0^t d\tilde{t}_1'^\sigma .. \int_{\tilde{t}'^\sigma_{m'_\sigma-1}}^t d\tilde{t}'^\sigma_{m'_\sigma} \int_0^t dt_1^\sigma .. \int_{t^\sigma_{n_\sigma-1}}^t dt^\sigma_{n_\sigma} \int_0^t dt_1'^\sigma .. \int_{t'^\sigma_{n'_\sigma-1}}^t dt'^\sigma_{n'_\sigma} \\ &\times \mathrm{Tr}_{dot}\left[\tilde{T}T\, d_\sigma(\tilde{t}_1^\sigma) d_\sigma^\dagger(\tilde{t}_1'^\sigma) d_\sigma(\tilde{t}_2^\sigma) d_\sigma^\dagger(\tilde{t}_2'^\sigma)\ldots d_\sigma(t_2^\sigma) d_\sigma^\dagger(t_2'^\sigma) d_\sigma(t_1^\sigma) d_\sigma^\dagger(t_1'^\sigma)\,\rho_{\mathrm{dot}}(t=0)\right] \\ &\times \mathrm{Tr}_{bath}\left[\tilde{T}T\, c_\sigma^\dagger(\tilde{t}_1^\sigma) c_\sigma(\tilde{t}_1'^\sigma) c_\sigma^\dagger(\tilde{t}_2^\sigma) c_\sigma(\tilde{t}_2'^\sigma)\ldots c_\sigma^\dagger(t_2^\sigma) c_\sigma(t_2'^\sigma) c_\sigma^\dagger(t_1^\sigma) c_\sigma(t_1'^\sigma)\,\rho_{bath}\right], \end{aligned} \tag{4.17}$$

with the abbreviation $c_\sigma^\dagger(t) = \sum_{\alpha,k} t_{\alpha,k,\sigma} c^\dagger_{\alpha,k,\sigma}(t)$. For non-interacting bath electrons, the trace over bath degrees of freedom can be analytically evaluated by applying Wick's theorem, which gives a product of two determinants

$$\mathrm{Tr}_{bath}[\ldots] = \prod_\sigma \det(\Delta_\sigma). \tag{4.18}$$

The size of the matrix Δ_σ is given by the number of quantum dot operators $d_\sigma^\dagger$ and its matrix elements are [151]

$$\Delta_\sigma^{(i,j)} = \begin{cases} \Delta^<(t'_j - t_i) & \text{if } t_{K,i} \geq t_{K,j}, \\ \Delta^>(t'_j - t_i) & \text{if } t_{K,i} < t_{K,j}, \end{cases} \tag{4.19}$$

with $t_{K,j}$ being the position of the jth creation operator and $t_{K,i}$ the position of the ith annihilation operator on the unfolded Keldysh contour. The hybridization function

$\Delta^{</>}$ is given by

$$\Delta^{<}(t) = -i \sum_{\alpha=L,R} \int_{-\infty}^{\infty} \frac{d\omega}{\pi} \Gamma_\alpha(\omega) f(\omega - \mu_\alpha) \exp(-i\omega t), \tag{4.20}$$

$$\Delta^{>}(t) = i \sum_{\alpha=L,R} \int_{-\infty}^{\infty} \frac{d\omega}{\pi} \Gamma_\alpha(\omega) \left[1 - f(\omega - \mu_\alpha)\right] \exp(-i\omega t). \tag{4.21}$$

We model $\Gamma_\alpha(\omega)$ by a flat band with a bandwidth of $2\omega_c$ given by

$$\Gamma_\alpha(\omega) = \frac{\Gamma_\alpha}{(1 + e^{\nu(\omega-\omega_c)})(1 + e^{-\nu(\omega+\omega_c)})}, \tag{4.22}$$

with a smoothing factor ν, which can be defined as $\nu = 1/k_B T$. In principle, a metallic bath with infinite bandwidth can be implemented. However, as we will later see, the dynamical sign problem aggravates for large bandwidths. Furthermore, it needs to be noted that in the present definition of $\Gamma_\alpha(\omega)$, the time-dependent observables depend on the particular values of ω_c. However, for voltages that are small compared to the bandwidth $2\omega_c$, changes in observables are vanishingly small and decay on a time scale of the order ω_c^{-1} [31]. Finally, the hybridization function yields

$$\Delta^{</>}(t) = \Gamma\, k_B T \frac{\cos(Vt/2) - \exp(\pm i\omega_c t)}{\sinh(\pi k_B T\, t)}. \tag{4.23}$$

The trace over the quantum dot states in Eq. (4.17) has to be numerically evaluated. In Refs. [30, 151] the segment or kink representation has been employed, which is applicable for quantum dots with density-density interaction. The occupation of the quantum dot with spin up or spin down particles is uniquely determined by the order of creation and annihilation operators. In this case, the representation of the quantum dot occupation as segments for different times[1] allows for an efficient algorithm. In the following, however, the segment representation is not applied in order to be able to incorporate other interaction types than density-density interactions. Instead, the reduced quantum dot system will be represented in the eigenbasis of the quantum dot Hamiltonian. In order to speed up the multiplication of matrices associated with creation and annihilation operators, matrices are stored as sparse data types.

The Monte Carlo algorithm samples orders of operators on the Keldysh contour

[1] A segment is an interval in time during which the quantum dot is occupied.

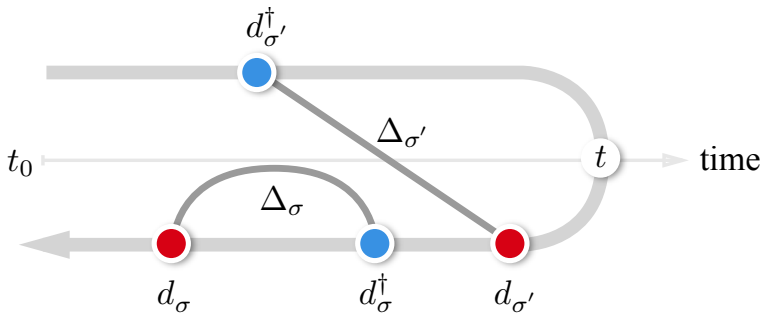

Figure 4.1: A particular diagram on the Keldysh time contour emerging in the expansion of Eq. (4.17). The blue (red) dots mark quantum dot creation (annihilation) operators on the forward (upper) and backward (lower) branch. Each pair of creation and annihilation operators of same spin is connected by the hybridization function (Eq. 4.21).

(Fig. 4.1) according to the weight

$$w(t_{K,1},\ldots,t_{K,2n+1}) = \prod_\sigma (i)^{m_\sigma+m'_\sigma}(-i)^{n_\sigma+n'_\sigma}\,\det\Delta_\sigma\,\mathrm{Tr}_{dot}[\ldots]. \tag{4.24}$$

The Markov chain of orders is constructed by the following local updates[2]: (i) insertion of a quantum dot creation and annihilation operator and (ii) removal of a quantum dot creation and annihilation operator.

The time-evolution of observables $\langle O(t)\rangle$ can be computed by summing up all possible diagrams

$$\langle\mathcal{O}(t)\rangle = \mathrm{Tr}\left[\left(\tilde{T}e^{i\int_0^t dt'\,H_{\mathrm{mix}}(t)}\right)\mathcal{O}\left(Te^{-i\int_0^t dt'\,H_{\mathrm{mix}}(t)}\right)\rho_0\right] = \frac{\langle\arg(w)\,\mathcal{O}\rangle_{|w|}}{\langle\arg(w)\rangle_{|w|}}. \tag{4.25}$$

The current through lead α can be estimated by the following expansion

$$I_\alpha = -2\,\mathrm{Im}\sum_{k,\sigma} t_{\alpha,k,\sigma}\,\langle c^\dagger_{\alpha,k,\sigma}d_\sigma\rangle \tag{4.26}$$

$$= -2\,\mathrm{Im}\,\mathrm{Tr}\left[\left(\tilde{T}e^{i\int_0^t dt'\,H_{tunnel}(t')}\right)e^{i(H_{dot}+H_{lead})t}\sum_{k,\sigma} t_{\alpha,k,\sigma}\,c^\dagger_{\alpha,k,\sigma}d_\sigma\right. \tag{4.27}$$

$$\left.\times\, e^{-i(H_{dot}+H_{lead})t}\left(Te^{-i\int_0^t dt'\,H_{tunnel}(t')}\right)\rho_0\right]. \tag{4.28}$$

For the current estimate, similar diagrams as in the expansion of the partition function

[2]Local updates change only a small part of a configuration, in that they add or remove a pair of operators. Additionally, global updates could be implemented, creating completely new sequences of operators.

(Eq. 4.17) are obtained. Here, however, one quantum dot operator is fixed at time t, and a hybridization function is used that only connects the lead α. By sampling the corresponding diagrams the current is obtained via [151]

$$I_\alpha = \sum_C w_C, \tag{4.29}$$

with the configurations C given by all current diagrams for lead α and spin σ. While the strong-coupling approach represents a perturbation expansion in the tunnel coupling, it has to be emphasized that the method generates numerically exact solutions only restricted by computing power and time.

4.1.2 Expansion in the Coulomb interaction

The strong-coupling version of real-time quantum Monte Carlo described in the previous section has been originally developed for equilibrium calculations and was only recently adapted to non-equilibrium transport. Besides strong-coupling QMC, a complementary approach, the weak-coupling QMC, was developed, which relies on an expansion in powers of the Coulomb interaction U. Weak-coupling QMC comes in two flavors: One incorporates the sampling of a Hubbard-Stratonovich (HS) field and the other the direct sampling of the Green's function expansion in U. Transport calculations using auxiliary-field QMC were recently conducted by Werner et al. [32,151]. The expansion in U is obtained by using the Hubbard-Stratonovich transformation to decouple the quartic Coulomb term, leading to a summation over HS field variables. During the transformation, Werner et. al introduced an auxiliary parameter that helps reducing the oscillatory behavior of the integrand and thereby the dynamical sign problem.

In this section, we take the other path and adopt the weak-coupling QMC version developed by Rubtsov et al. for equilibrium [150] to calculate non-equilibrium transport by directly sampling the Green's function expansion in the Coulomb interaction. In this approach, we use the exact solution of the non-interacting Green's function (GF) for a quantum dot tunnel coupled to leads, which we had already derived in section 1.3. The Coulomb interaction is introduced by standard GF perturbation theory around this non-interacting solution. We introduce two so-called α parameters, similarly to the equilibrium method by Rubtsov et al., in which these parameters allowed to extinguish the sign problem [150]. For the first time, we apply this method to transport through the single-level quantum dot and explore the effect of the α parameters on the dynamical sign problem. It has to be noted that while auxiliary-field QMC and the direct expansion

both are based on the expansion in U, they only become formally equivalent in the case of particle-hole symmetry [163].

In order to obtain the weak-coupling version of QMC in non-equilibrium we start by splitting the single-level quantum dot Hamiltonian into two parts, the single-particle energy and the Coulomb interaction,

$$H_{dot} = H^0_{dot} + H^U_{dot} = \varepsilon_d \left(n_\uparrow + n_\downarrow\right) + U\, n_\uparrow n_\downarrow. \tag{4.30}$$

The time evolution of $H_0 = H^0_{dot} + H_{bath} + H_{tunnel}$ is treated exactly while the expansion in perturbation orders of H^U_{dot} is numerically sampled.

In the spirit of weak-coupling Monte Carlo for equilibrium calculations [150], we introduce the parameter $\alpha_\uparrow$ and $\alpha_\downarrow$ by the transformation $n_\sigma \to n_\sigma + \alpha_\sigma$. This transformation allows to re-express the interaction part of the Hamiltonian

$$H_{int} = U(n_\uparrow - \alpha_\uparrow)(n_\downarrow - \alpha_\downarrow), \tag{4.31}$$

and the single-particle term

$$H_{dot} = (\varepsilon_d + \alpha_\downarrow U)n_\uparrow + (\varepsilon_d + \alpha_\uparrow U)n_\downarrow - U\alpha_\uparrow\alpha_\downarrow. \tag{4.32}$$

Note that the constant term $U\alpha_\uparrow\alpha_\downarrow$ is irrelevant as it drops out due to the proper normalization of the density matrix. The introduction of the auxiliary α parameter allows us to modify the expansion terms and ideally reduce the expansion order. In fact, it has been shown in the equilibrium version of weak-coupling QMC that every odd order in the U expansion vanished for the particle-hole symmetric case and the proper value of α_σ [150].

The quantum dot and leads are disconnected for times $t < 0$, and the quantum dot is prepared in an empty state $|0\rangle$, while the leads are in equilibrium, resulting in the initial density matrix,

$$\rho_0 = |0\rangle\langle 0| \otimes e^{-\beta H_{bath}}. \tag{4.33}$$

Similar to the strong-coupling version of non-equilibrium QMC, we expand the partition function of the time-dependent density matrix

$$Z = \mathrm{Tr}\left[\tilde{T} e^{i\int_0^t ds H_{int}(s)} e^{it(H_{dot}+H_{bath}+H_{tunnel})} e^{-it(H_{dot}+H_{bath}+H_{tunnel})} e^{-i\int_0^t ds H_{int}(s)}\, \rho_0\right], \tag{4.34}$$

which is by construction $Z = 1$. In a next step, the Coulomb interaction term is expanded

around the the exact solution for the non-interacting system (cf. section 1.3), giving

$$\begin{aligned} Z = \mathrm{Tr}[\sum_{n_+} (iU)^{n_+} \int_0^t d\tilde{t}_1 \dots \int_{\tilde{t}_{n_+-1}}^t d\tilde{t}_{n_+} e^{i\tilde{t}_1 H_0} (n_\uparrow - \alpha_\uparrow)(n_\downarrow - \alpha_\downarrow) \dots \\ e^{i(\tilde{t}_{n_+} - \tilde{t}_{n_+-1})H_0} (n_\uparrow - \alpha_\uparrow)(n_\downarrow - \alpha_\downarrow) e^{i(t-\tilde{t}_{n_+})H_0} \\ \sum_{n_-} (-iU)^{n_-} \int_0^t dt_1 \dots \int_{t_{n_--1}}^t dt_{n_-} e^{-i(t-t_{n_-})H_0} (n_\uparrow - \alpha_\uparrow)(n_\downarrow - \alpha_\downarrow) \dots \\ e^{-i(t_2-t_1)H_0} (n_\uparrow - \alpha_\uparrow)(n_\downarrow - \alpha_\downarrow) e^{-it_1 H_0} \rho_0] \end{aligned} \tag{4.35}$$

with $H_0 = H_{dot} + H_{bath} + H_{tunnel}$. The expansion leads to a product of expectation values of the particle operator n_σ with respect to the non-interacting Hamiltonian H_0 and allows for applying Wick's theorem,

$$Z = \sum_{n_+} \sum_{n_-} (i)^{n_+} (-i)^{n_-} U^{n_+ + n_-} \int_0^t d\tilde{t}_1 \dots \int_{\tilde{t}_{n_+-1}}^t d\tilde{t}_{n_+} \int_0^t dt_1 \dots \int_{t_{n_--1}}^t dt_{n_-} \prod_\sigma \det i G^\alpha_{0,\sigma}. \tag{4.36}$$

The auxiliary Green's function

$$iG^\alpha_{0,\sigma}(t'_K, t''_K) = iG_{0,\sigma}(t'_K, t''_K) - \alpha_\sigma \, \delta_{t'_K, t''_K}, \tag{4.37}$$

incorporates the α parameter and the Green's function of the non-interacting system of a quantum dot tunnel coupled to leads,

$$G_{0,\sigma}(t', t'') = \begin{cases} G^<_{0,\sigma}(t'_K, t''_K), & t'_K < t''_K \\ G^>_{0,\sigma}(t'_K, t''_K), & t'_K \geq t''_K, \end{cases} \tag{4.38}$$

which has been obtained in chapter 1.3 for the case in which the quantum dot and leads are decoupled for $t < 0$ and the tunnel coupling is instantly switched on at $t = 0$. Finally, the Monte Carlo algorithm samples the expansion orders in $G_{0,\sigma}$ (Fig. 4.2) according to the weight

$$w(t_1^K, t_2^K \dots t_n^K) = (i)^{n_+} (-i)^{n_-} U^{n_+ + n_-} \prod_\sigma \det G^\alpha_{0,\sigma}. \tag{4.39}$$

The different expansion orders are constructed by the following local updates: (i) two (time) points are randomly selected on the Keldysh time contour and connected by $G^\alpha_{0,\sigma}$, and (ii) a Green's function $G^\alpha_{0,\sigma}$ is removed.

In order to obtain the time evolution of the particle expectation value $\langle n_\sigma \rangle(t)$ and the

double occupancy $\langle n_\uparrow n_\downarrow\rangle(t)$, the full Green's function $G_\sigma(t'_K, t''_K) = \langle d_\sigma(t') d^\dagger_\sigma(t')\rangle$ of the interacting quantum dot is required, which can be obtained by sampling the following quantity [32, 150, 151]

$$\begin{aligned}\tilde{G}_\sigma(t'_K, t''_K) &= \frac{w\{(t_1^K, t_2^K \dots t_n^K); d_\sigma(t') d^\dagger_\sigma(t'')\}}{w(t_1^K, t_2^K \dots t_n^K)} \\ &= \frac{1}{\det G_{0,\sigma}} \det \begin{bmatrix} G_{0,\sigma}(t_{K,i}, t_{K,j}) & iG_{0,\sigma}(t_{K,i}, t''_K) \\ -iG_{0,\sigma}(t'_K, t_{K,j}) & iG_{0,\sigma}(t'_K, t''_K) \end{bmatrix} \\ &= G_{0,\sigma}(t'_K, t''_K) - i \sum_{i,j} G_{0,\sigma}(t'_K, t_{K,i}) G_{0,\sigma}(t_{K,i}, t_{K,j}) G_{0,\sigma}(t_{K,j}, t''_K). \end{aligned} \tag{4.40}$$

The full Green's function is then obtained by evaluating the Monte Carlo expectation value

$$G_\sigma(t'_K, t''_K) = \langle \tilde{G}_\sigma(t'_K, t''_K)\rangle, \tag{4.41}$$

and sampling the orders of the expansion Eq. (4.36). With knowledge of $G_\sigma(t'_K, t''_K)$, the time-dependent occupation of the quantum dot

$$\langle n_\sigma\rangle(t) = 1 - i\langle \tilde{G}_\sigma(t,t)\rangle \tag{4.42}$$

and the double occupation

$$\langle n_\uparrow n_\downarrow\rangle(t) = \langle [1 - i\tilde{G}_\uparrow(t_K, t_K)][1 - i\tilde{G}_\downarrow(t,t)]\rangle \tag{4.43}$$

can be obtained.

In the next section, we compare the dynamical sign problem for strong-coupling and

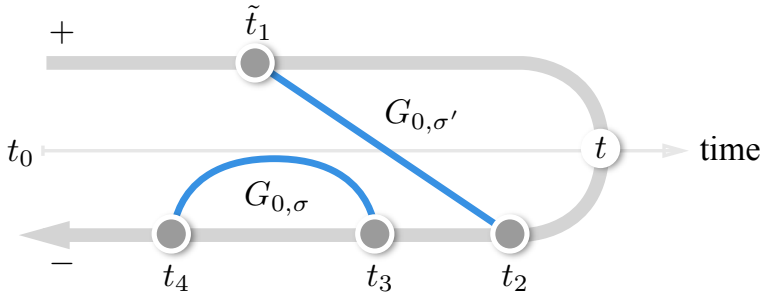

Figure 4.2: Configurations are constructed by randomly selecting pairs of time on the two branches of the Keldysh contour. A sequence of non-interacting Green's functions connect each pair of times according to Eq. (4.36).

weak-coupling QMC in the simulation of real-time dynamics of the impurity model. In both cases, the quantum dot is initially prepared in an empty state and the coupling to the electron bath is switched on at time $t = 0$. Furthermore, we investigate the optimal choice of the α parameters in our implementation of the weak-coupling QMC.

4.2 Dynamical sign problem

Strong-coupling and weak-coupling QMC estimate the expectation values of observables at time t by sampling the different expansion orders in the hybridization and non-interacting Green's function, respectively. The order corresponds to the number of operator pairs on the Keldysh contour (strong coupling) or the number of Green's functions (weak coupling), respectively (cf. Eqn. 4.36 and 4.25). The Monte Carlo procedure samples these different orders according to their contribution (weight) to the estimates. The sampling probability of the expansion orders n is shown in Fig. 4.3 for simulations of the single-level impurity model. In both methods, the probability to sample higher orders grows with the simulated time t. The probability of certain expansion orders n are distributed around an average order $\bar{n}$ and decay exponentially for larger orders $n > \bar{n}$. This ensures that the QMC simulation converges to the exact result as higher order contributions become vanishingly small. The maxima in the curves of the expansion order distribution give an estimate of the mean expansion order $\bar{n}$, which increases linearly in time.

While the average expansion order grows with the simulation time, it does not define

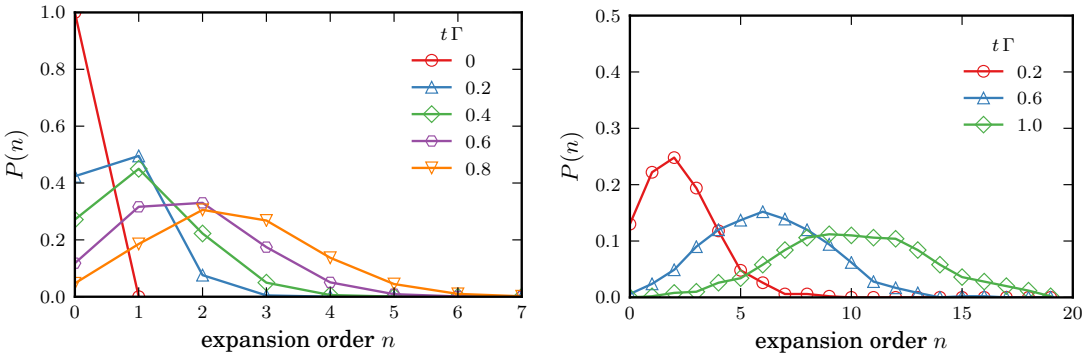

Figure 4.3: Distribution of the expansion order n in the strong-coupling (left) and weak-coupling approach (right) for different simulated times t. Parameters for the strong-coupling simulation are $\varepsilon_d = U = 0$, temperature $k_bT = 0.1\,\Gamma$, bandwidth $2\omega_c = 10$. The weak-coupling simulation is conducted for $\varepsilon_d = 2U = 3$ and $\alpha_\uparrow = \alpha_\downarrow = 0.1$.

the main limiting factor of the simulation. The average sign, which is found to decrease exponentially with the expansion order, primarily limits the simulation time as well as the accessible interaction strengths in the model. The complex valued hybridization function, Green's function and the free quantum dot propagation contribute to the decay of the sign. The panels of Fig. 4.4 show the average sign versus the simulation time for different interaction strengths U.

The average sign in the strong-coupling approach limits the possible simulation times t to the order of Γ^{-1}. However, it depends only weakly on the selected energy and interaction strength. For every parameter set, the average sign exponentially decays (cf. right panel of Fig. 4.5), but the strength of the decay depends on the model parameters. In particular, a finite voltage as well as a larger bandwidth of the bath accelerates the approach to steady state. At the same time, however, the sign decays more rapidly with bandwidth, demanding a carefully chosen value of ω_c that finds a balance between simulation time and reaching a steady state if possible (right panel Fig. 4.5). Results presented in the next section are obtained for $2\omega_c = 10$.

In contrast, the average sign in the weak-coupling approach strongly depends on the strength of the expansion parameter given by the Coulomb interaction U/Γ. Similar to the equilibrium version of the approach, the expansion order grows linearly with the interaction strength. This approach can be optimized through the α_σ parameters to

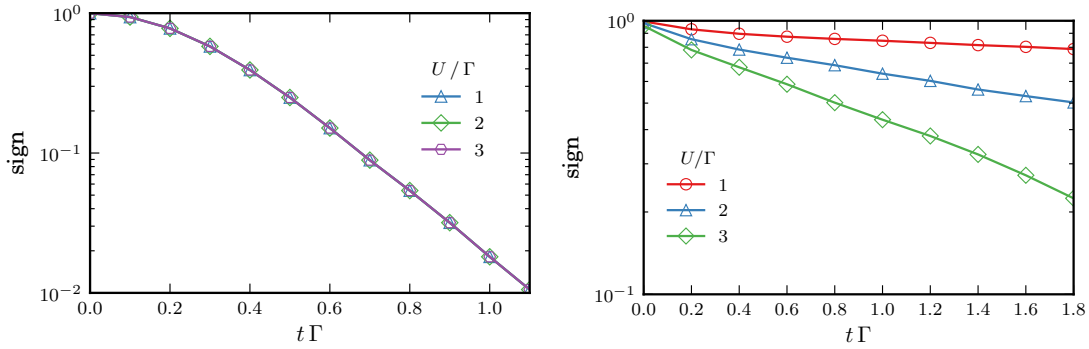

Figure 4.4: Average sign $\langle \arg(w) \rangle_{|w|}$ of the Monte Carlo weight w in the strong-coupling (left) and weak-coupling (right) approach for different interaction strengths U in the Coulomb blockade regime $2\varepsilon_d + U = 0$. While the strong-coupling approach does not show any dependency of the sign decay on the interaction strength, the weak-coupling approach considerably depends on U/Γ (shown for $\delta = 0.01$, see text). The strong dependence of the average sign on the Coulomb interaction in the weak-coupling approach is due to the fact that for stronger interactions higher orders in the expansion around the non-interacting system are needed.

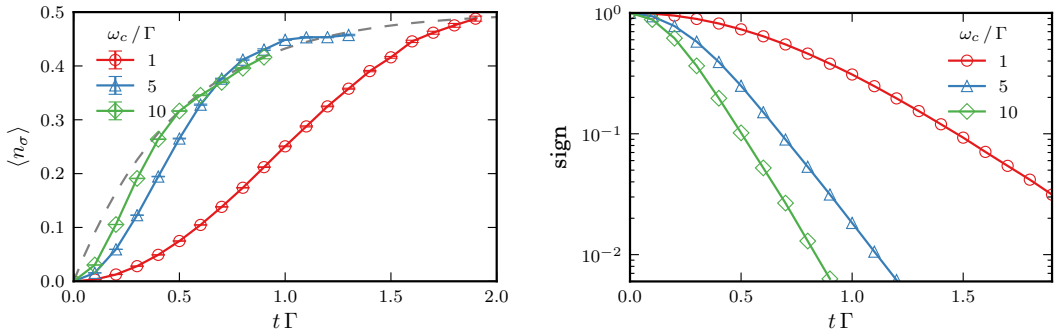

Figure 4.5: left: Time-dependent occupation of the quantum dot with $\varepsilon_d = U = 0$, $k_B T = 0.1\Gamma$ and for different bandwidths ω_c compared to the analytical solution (gray). right: decay of the average sign for the same parameters.

reach longer simulated times. In principle, one can choose $\alpha_\uparrow$ and $\alpha_\downarrow$ independently. Each choice will add a mean-field interaction $\alpha_\sigma U$ to the single-electron energy for spin-up and spin-down. When $\alpha_\uparrow \neq \alpha_\downarrow$, the spin inversion symmetry of the system is formally restored through sampling the entire series expansion Eq. (4.36), however, in practice the Monte Carlo sampling of the expansion around a spin-split, non-interacting system is challenging [159]. One way to avoid the symmetry breaking is to introduce auxiliary fields $s = \uparrow, \downarrow$ and expanding in

$$H_{int} = \frac{U}{2} \sum_{s=\uparrow,\downarrow} (n_\uparrow - \alpha_{s,\uparrow})\,(n_\downarrow - \alpha_{s,\downarrow}). \tag{4.44}$$

For equilibrium, the following choice has been found to be beneficial in actual calculations [150],

$$\alpha_{s,\sigma} = \begin{cases} \frac{1}{2} + \delta & s = \sigma, \\ -\delta & s \neq \sigma, \end{cases} \tag{4.45}$$

with a small positive value δ for the half-filling regime where $\langle n_\sigma^{eq} \rangle = 1/2$.

In the real-time version of the weak-coupling approach, we also find a favorable sign decay for the choice $\delta \approx 0.01$ while avoiding numerical instabilities (Fig. 4.4, right). With this choice, the probability for each odd expansion order is reduced (Fig. 4.6). In fact, the power of the $\alpha_{s,\sigma}$ parameters in tackling the sign problem stems not from reducing the overall order of the expansion, but from reducing the contribution of every second order. This behavior has also been recently found in the real-time version of the auxiliary field QMC in Ref. [32].

With both methods, accurate results for expectation values of observables can be

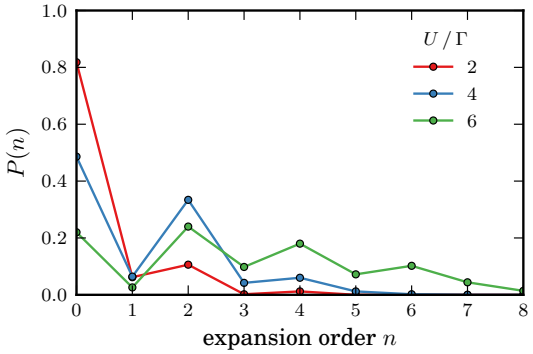

Figure 4.6: Distribution of the expansion order n in the weak-coupling approach for $2\varepsilon_d + U = 0$ and different interaction strengths, $\delta = 0.01$ and $t\,\Gamma = 1$. The probability of odd orders decreases when choosing a small parameter δ.

obtained as long as the magnitude of the average sign is larger than its statistical error, which is feasible for $\langle \text{sign} \rangle \gtrsim 0.001$. However, whether the steady state can be reached within the accessible simulation time depends on the model and its parameters as well as on the measured observable.

4.3 Strong-coupling QMC for the dynamics of the magnetic impurity model

In the following, we study the non-equilibrium dynamics of charge carriers tunneling through a magnetic quantum dot by applying strong-coupling QMC. The goal of this section is to give a proof of principle for the implementation of quantum Monte Carlo method for a wider class of systems.

The underlying model is the Anderson impurity model consisting of a single-level quantum dot coupled to two electronic reservoirs. Additionally, the electrons on the dot are exchange coupled to a local spin $1/2$ of a magnetic impurity embedded into the quantum dot. This system serves as a minimal model to study the dynamics in dilute magnetic semiconductor quantum dots [22, 164–166], but also the influence of nuclear spins on the electron dynamics [36, 167, 168]. While the magnetic impurity model is not conceived to provide quantitative results for realistic systems, it serves as a generic model to understand the mutual interactions of electrons and localized spins as well as their impact on dephasing and relaxation in nanosystems.

From a methodological perspective, the magnetic impurity model is also an ideal basis to develop and benchmark numerical methods for the treatment of the dynamics

in systems subject to electron-impurity interactions. Here, we implement the strong-coupling QMC method to include exchange interactions between electrons and the local impurity spin. While we have shown that the weak-coupling approach is preferable for weak interactions, the strong-coupling approach allows to treat the dynamics for the full crossover between weak and strong electron-impurity coupling.

The implemented total Hamiltonian is given by the Anderson impurity part H_{dot} + $H_{bath} + H_{tunnel}$ introduced in section 4.1 (Eq. 4.1) and an additional exchange Hamiltonian term H_{exch} describing the coupling between the electron spin $\vec{S}$ and the impurity spin $\vec{M}$ by exchange interaction of strength J,

$$H_{\text{exch}} = J\,\vec{S}\,\vec{M} = \underbrace{J\,M_z\,(d_\uparrow^\dagger d_\uparrow - d_\downarrow^\dagger d_\downarrow)}_{H_{\text{exch}}^{(\text{long})}} + \underbrace{\frac{J}{2}\,(M^+ d_\downarrow^\dagger d_\uparrow + M^- d_\uparrow^\dagger d_\downarrow)}_{H_{\text{exch}}^{(\text{trans})}}, \tag{4.46}$$

with the spin operators of the impurity given by $\vec{M} = (M_x, M_y, M_z)$ and $M_\pm = M_x \pm iM_y$. The exchange interaction can be divided into a longitudinal part $H_{\text{exch}}^{(\text{long})}$ and a transversal part $H_{\text{exch}}^{(\text{trans})}$. The longitudinal part merely renormalizes the electron energies and resembles the impact of an effective magnetic field, while the second part creates mutual flips of the electron spin and impurity spin. Furthermore, the interaction H_{exch} is only present for a single electron in the quantum dot, while vanishing for a two electron state forming a singlet.

We have implemented strong-coupling QMC to treat the dynamics of the quantum dot described by full the Hamiltonian $H = H_{dot} + H_{bath} + H_{tunnel} + H_{exch}$ coupled to non-interacting leads. Initially, the quantum dot is prepared in a given state and decoupled from the leads. We investigate the dynamics and transport after the coupling is switched on at $t = 0$, emphasizing the effects introduced by the transversal exchange interaction that induces electron-impurity spin flips. In order to distinguish between non-trivial spin-flip dynamics due to the transversal part and the effects caused by the longitudinal part of the exchange interaction, we first discuss the consequences of $H_{\text{exch}}^{(\text{long})}$ on the dynamics.

If the transversal interaction part is not present, the orientation of the impurity will be frozen without the possibility of electron-impurity flip-flops. In that case, the longitudinal part of the exchange interaction, acting as an effective magnetic field, only renormalizes the energies and rates. In the absence of exchange interactions, the quantum dot density of states for spin-up and spin-down electrons equals, while the longitudinal interaction term, on the other hand, shifts the densities for spin-up and spin-down elec-

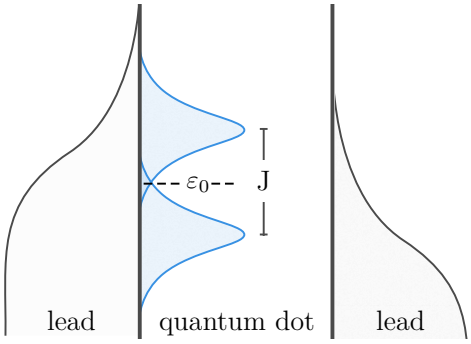

Figure 4.7: Schematic depiction of the density of states in the quantum dot and lead while incorporating the longitudinal component of the exchange interaction. The density of states in the leads is given by the respective Fermi function and includes temperature broadening. The density of states in the dot is shifted apart by the exchange interaction J due to the effective exchange field $B_{exch} = 1/2\, J\, S_z\, M_z$ and shows tunnel-induced broadening.

trons apart. This process is proportional to the energy J and depending on the relative orientation between electron spin and impurity spin (Fig. 4.7). In line with this, the energies of spin-up and spin-down electrons are renormalized $\varepsilon_d \to \varepsilon_d + 1/2 J \langle S_z \rangle \langle M_z \rangle$.

Including the transversal interaction part, by contrast, induces electron-impurity spin flips, resulting in the relaxation of an initially polarized impurity spin. For weak exchange interaction $J \ll \Gamma$, the time scale of the impurity relaxation can be expected to be long compared to the tunneling time of electrons Γ^{-1}. In this regime, the impurity primarily acts as an effective magnetic field and can be included by the mean-field type of interaction described above. In the regime of strong exchange interaction, $J \gtrsim \Gamma$, however, electron-impurity spin flips (flip-flops) are expected to dominate the non-equilibrium dynamics of the system. In the following, we analyze the transition from weak exchange interaction $J \lesssim \Gamma$ to strong exchange interaction $J \gtrsim \Gamma$, including both longitudinal and transversal components. In contrast to perturbative approaches, the QMC method allows for the calculation of the continuous parameter crossover.

In a first step, the time evolution from non-equilibrium to equilibrium is considered for an empty quantum dot that is initially decoupled from the bath and for a polarized impurity spin $\langle M_z \rangle = 1/2$. Fig. 4.8 shows the time-dependent occupation and double occupancy of the quantum dot after the coupling between quantum dot and bath is switched on at $t = 0$. The bias voltage between the leads is set to $V = 0$, and for energies $\varepsilon_d = U = 0$ the tunneling of electrons into the quantum dot is studied.

As the quantum dot is charged over time, a splitting of the electron density for spin-

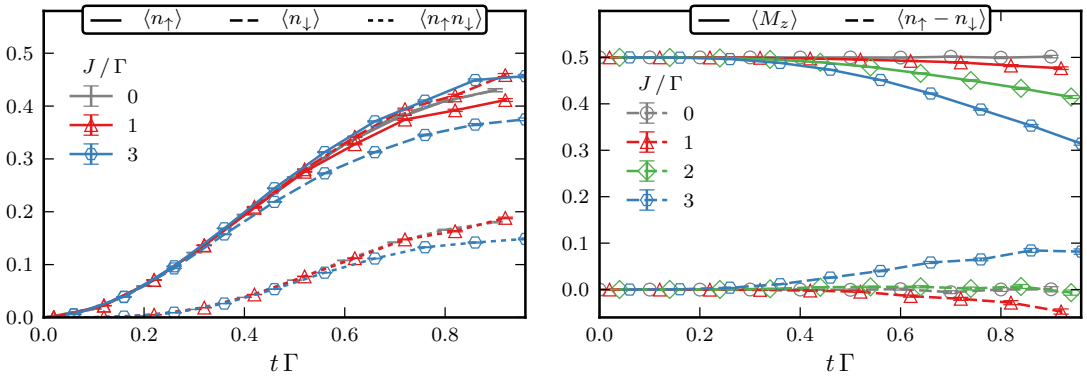

Figure 4.8: left: Time-dependent, spin-resolved occupation and double occupancy of the quantum dot for $\varepsilon_d = U = 0$, zero bias $V = 0$ and different values of the exchange interaction strength J/Γ. Occupancy of spin-up and spin-down electron splits apart with time for finite J/Γ, while double occupancy is slightly suppressed. right: Corresponding spin accumulation on the quantum dot $\langle S_{acc}\rangle = \langle n_\uparrow - n_\downarrow\rangle$ and expectation value of the impurity spin projection $\langle M_z\rangle$. Weak exchange interaction $J \lesssim \Gamma$ results in a negative spin accumulation, while stronger exchange couplings $J > \Gamma$ produce a transient positive spin accumulation. The impurity spin relaxes on time scales larger than the electron tunneling time Γ^{-1}.

up and spin-down is clearly observable and accompanied by a suppression of the double occupation for larger values of J. While the splitting of the spin-resolved density can be expected due to the effect of the longitudinal exchange interaction, the majority spin type on the quantum dot changes for larger J. This is revealed in the spin accumulation $\langle S_{acc}\rangle = \langle n_\uparrow - n_\downarrow\rangle$ shown on the right panel of Fig. 4.8 together with the impurity orientation $\langle M_z\rangle$. As for the present initial configuration, a small value $J \lesssim \Gamma$ results in an effective magnetic field $B_{exch} = J/2$ and induces a majority of spin-down electron density on the quantum dot (negative spin accumulation $S_{acc} < 0$). In this regime, the impurity spin shows evidence of very slow relaxation, implying that electron-impurity spin flips play a subordinate role. As the exchange interaction is increased, coherent spin flip-flops between electrons and impurity become more important and result in an accelerated relaxation of the impurity spin. At the same time, the emergence of a positive spin accumulation on the quantum dot can be observed. This is a transient effect stemming from the initial polarization of the impurity, which results in a spin-flip probability that is skewed towards flip-flops increasing the spin accumulation on the quantum dot. One can expect, however, that both flip-flop rates become equal as the impurity spin relaxes.

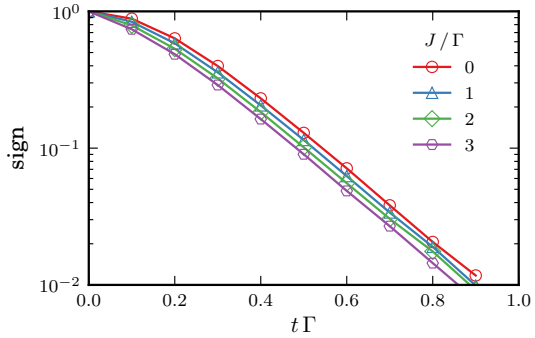

Figure 4.9: Average sign versus time for different exchange coupling and parameters as in Fig. 4.9.

For the present initial state, we are unable to reach equilibrium (due to the dynamic sign problem, Fig. 4.9) and hence are not able to observe the exponential relaxation of the impurity spin studied in [22,169]. In fact, a second order diagrammatic perturbation theory can give an estimate for the impurity relaxation time τ_{relax} for weak exchange coupling $J \ll \Gamma$ [22],

$$\tau_{relax}^{-1} = \frac{J^2\,\Gamma^2}{16\pi} \sum_{\sigma,\sigma'=\pm} \int_{-\infty}^{\infty} d\omega \frac{[f_R^+(\omega) + f_L^+(\omega)][f_R^-(\omega) + f_L^-(\omega)]}{[(\omega - \varepsilon_d - \sigma J/2)^2 + \Gamma^2][(\omega - \varepsilon_d - \sigma' J/2)^2 + \Gamma^2]}, \tag{4.47}$$

which is inaccessible in the present study due to the dynamical sign problem. Therefore, we shift the discussion towards the time evolution for a quantum dot initially prepared in the one-electron ground state given by a singlet state

$$|S\rangle = \frac{1}{\sqrt{2}} \left(|\uparrow\Downarrow\rangle - |\downarrow\Uparrow\rangle \right), \tag{4.48}$$

with an up (down) spin denoted by $|\uparrow\rangle$ ($|\downarrow\rangle$) for electrons and by $|\Uparrow\rangle$ ($|\Downarrow\rangle$) for the impurity. Other parameters remain unchanged and the zero-bias case is regarded.

Fig. 4.10 shows the time-evolution of the quantum dot with initial occupation $\langle n\rangle^0 = \langle n_\uparrow\rangle^0 + \langle n_\downarrow\rangle^0 = 1$ and $\langle n_\uparrow\rangle^0 = \langle n_\downarrow\rangle^0 = 1/2$, while the initial impurity spin projection is given by $\langle M_z\rangle^0 = 0$. For numerically accessible times, the spin-resolved occupation $\langle n_\sigma\rangle$ of the quantum dot barely show any time dependence for short times (inset Fig. 4.10 left). Instead, a time evolution in the double occupancy is noticeable. For $J = 0$, the equilibrium expectation value $\langle n_\uparrow n_\downarrow\rangle \simeq \langle n_\uparrow\rangle\langle n_\downarrow\rangle = 1/4$ for non-interacting electrons is approached. A finite exchange interaction between electrons and impurity spin suppresses the double occupation similar to the effect of finite Coulomb interaction (right panel of Fig. 4.10).

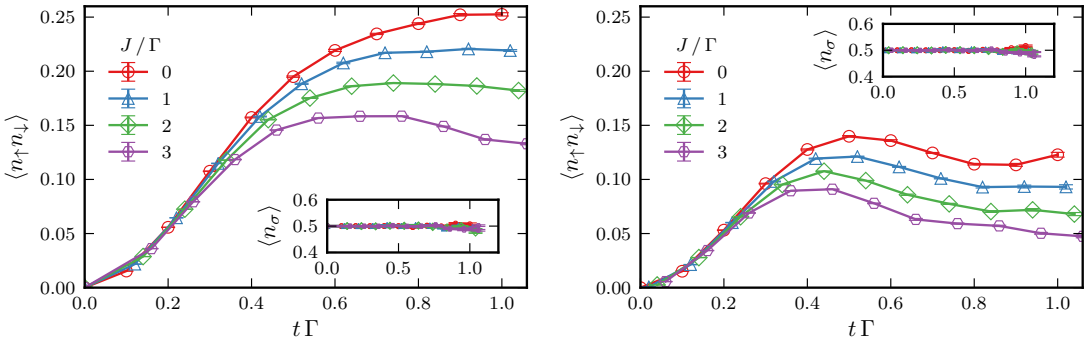

Figure 4.10: Time-dependent double occupation of the quantum dot for different values of the exchange interaction strength J/Γ between electron and impurity. The quantum dot is initially prepared in the one-particle ground state and the approach to equilibrium is computed for $V = 0$. The non-interacting case $U = \varepsilon_d = 0$ (left) and the finite Coulomb interaction case $U = -\varepsilon_d/2 = 4$ (right) exhibit a reduction of double occupancy for larger values J, while the occupancy $\langle n_\sigma \rangle$ barely show any dynamics for short times (inset).

The origin of the reduced double occupancy can be understood through the following picture. While the expectation value of the impurity spin gives $\langle M_z \rangle \approx 0$, fluctuations of the impurity shift apart the density of states in the quantum dot (cf. Fig. 4.7). In contrast to the previous situation, the electron spin orientation is subordinate as the field created by the impurity averages to zero. For an instance in time, however, each spin species of electrons can perceive a different effective field. This allows to calculate

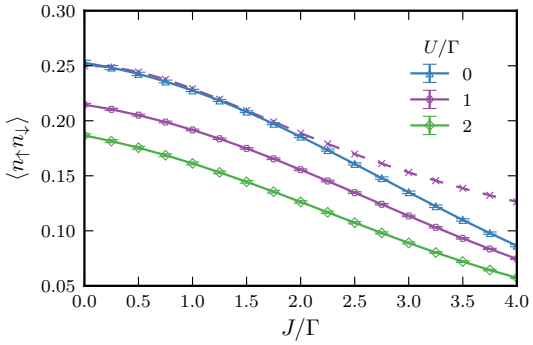

Figure 4.11: Double occupation of the quantum dot at time $t = \Gamma^{-1}$ for different interaction strengths U with $\varepsilon_d = -U/2$ and $V = 0$. Dashed line shows results obtained by Eq. (4.49). The double occupancy is suppressed for stronger exchange interaction strength between electron and impurity, which can be partly attributed to the longitudinal interaction term (for $J \lesssim 1.5\Gamma$).

the long-time limit of the double occupancy,

$$\langle n_\uparrow n_\downarrow \rangle \simeq \langle n_\uparrow \rangle \langle n_\downarrow \rangle = \frac{\Gamma^2}{4\pi^2} \int d\omega \int d\omega' \frac{[f_R^+(\omega) + f_L^+(\omega)][f_R^+(\omega') + f_L^+(\omega')]}{[(\omega - \varepsilon_d - J/2)^2 + \Gamma^2][(\omega' - \varepsilon_d + J/2)^2 + \Gamma^2]}. \tag{4.49}$$

This ansatz is supported by the long-time limit ($t = \Gamma^{-1}$) in Fig. 4.11, showing good agreement between the numerical results at $t = \Gamma^{-1}$ and Eq. 4.49 for small exchange coupling $J \lesssim 1.5\,\Gamma$. For larger values of J, flip-flops become increasingly important and lead to a stronger suppression of double occupancy and deviations from the above picture.

4.3.1 Non-equilibrium current in the magnetic impurity model

Furthermore, we studied the current through the magnetic quantum dot for an initially empty quantum dot and for different bias voltages V (Fig. 4.12). The previous section has revealed that the relaxation of the magnetic impurity occurs on time scales longer than the electron tunneling time. The time-dependent current, however, appears to reach a steady value on the time scale of Γ^{-1}, which is in agreement with results for small exchange interaction previously obtained by Becker et al. [22, 169]. In contrast, the displacement current $I_{disp} = (I_L + I_R)/2$ on the right panel of Fig. 4.12 still shows dynamics for times longer than the electron tunneling time, which reflects the time-dependent occupation of quantum dots observed in the previous section (cf. Fig. 4.8). Here, I_L (I_R) gives the current from the left (right) lead into the quantum dot.

The current through the quantum dot $I = I_L - I_R$ at $t = \Gamma^{-1}$ shows a monotonous

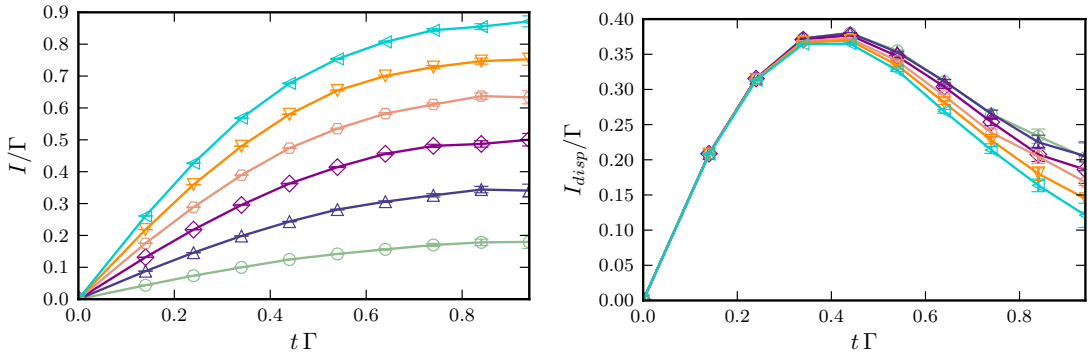

Figure 4.12: Time-dependent current through the quantum dot $I = I_L - I_R$ (left) and displacement current $I_{disp} = (I_L + I_R)/2$ (right) for different bias voltages $V = 1, 2, \ldots 6$ from bottom to top. The energies in the quantum dot are $\varepsilon_d = U = 0$ and $J = 2\,\Gamma$.

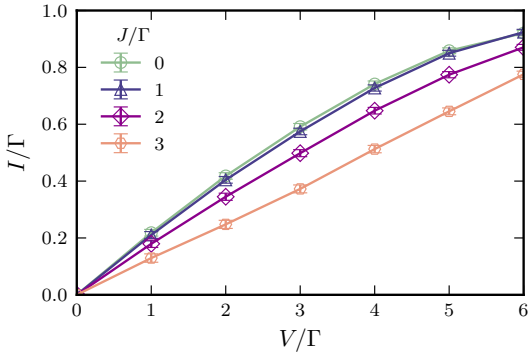

Figure 4.13: Current through the quantum dot $I = I_L - I_R$ at time $t = \Gamma^{-1}$ for different values of the electron-impurity interaction strength J/Γ. Small interaction strengths $J \lesssim \Gamma$ have a weak impact on the voltage-dependent current characteristics, while larger values $J > \gamma$ reduce the conductivity of the quantum dot.

dependence on the applied bias (Fig. 4.13). While it cannot be assumed that the steady state has yet been reached for all values of the exchange interaction strength J/Γ, the general trend can be deducted. Weak exchange interaction between electron and impurity $J \lesssim \Gamma$ shows minimal effect on the current for the considered bias regime. Stronger exchange interaction $J > \Gamma$ suppresses the current at finite bias and reduces the conductance of the quantum dot.

4.4 Summary

We have investigated the quantum Monte Carlo approach for transport dynamics that is based on the stochastic sampling of the Keldysh path integral. Expansions in the Coulomb interaction strength and in the tunnel-coupling between quantum dot and leads have been presented. Both approaches suffer from the dynamical sign problem that arises due to the sampling of complex (oscillatory) phases during the propagation in time. The limiting factor of the simulations is the average sign that decays exponentially with the expansion order and renders the simulation of long times prohibitively difficult.

We have transferred the diagrammatic Monte Carlo approach by Rubtsov et al. [150] to non-equilibrium problems. For weakly interacting quantum dots, this method can be carried out for longer times compared to the strong-coupling approach that expands in terms of the tunnel coupling. Its applicability strongly depends on the optimal choice of auxiliary parameters, which we showed to have a considerably favorable impact on the capable simulation time. However, as an expansion around the non-interacting system,

the average expansion order grows with the strength of the Coulomb interaction which makes it preferable for systems with weak to intermediate interaction strengths.

The expansion in the tunnel coupling shows rather unfavorable convergence properties. However, the decay of the average sign turns out to be almost independent of the quantum dot energies, making this approach suitable for all interaction strength and for the study of crossovers between interaction regimes. Choosing different initial states turned out beneficial for studying the time evolution from non-equilibrium to equilibrium.

The general advantage of both presented versions of quantum Monte Carlo compared to other non-equilibrium approaches is that the methods are numerically exact within the given stochastic error bars. There are no approximations like discretization or truncations.

We have also demonstrated that the QMC approach has potential for the simulation of small systems with additional degrees of freedom based on the example of the magnetic impurity model. We first discussed the dynamics of a quantum spin $1/2$ incorporated into a single-level quantum dot, which serves as a minimal model for e.g. magnetic impurities embedded in quantum dots or the interaction between nuclear spins and electrons. QMC allowed studying the dynamics of the impurity and electrons in the quantum dot after the coupling to leads is switched on. The evolution from non-equilibrium to equilibrium has been studied for the parameter crossover from weak to strong exchange interaction. For weak-exchange coupling between impurity and electrons, we find a reasonable agreement with the mean-field type approach, suggesting that the impurities act as an effective magnetic field in the dynamics of the electrons. Furthermore, the impurity spin shows slow relaxation that occurs on time scales much larger than the transient electron dynamics. A larger exchange-coupling, on the other hand, results in an enhanced impact of coherent electron-impurity flip-flops and induces transient spin accumulation on the quantum dot. In this regime, fluctuations of the impurity spin additionally suppress the quantum dot double occupancy. In the present study, QMC proves to be a potential tool to investigate the dynamics for the full parameter crossover in the low-temperature regime and even for zero bias.

This page intentionally left blank.

5 Conclusions and Outlook

The aim of this thesis has been to understand charge and spin dynamics in nanostructures that are brought out of equilibrium. In its three main parts the thesis covers the interactions and mechanisms defining the time scales of dynamics in quantum dots and small magnetic clusters. Chapter 2 deals with the charging dynamics of quantum dots coupled to a two-dimensional electron gas after an abrupt change in the gate potential. We investigated the dependence of the charging times on Coulomb correlations in the quantum dot and on spin and charge relaxation processes. In chapter 3, the spin dynamics of a small, ferromagnetic cluster are analyzed and its signatures in the current noise are investigated. Here, the spin switching is defined by the interplay of inelastic spin excitations and the interaction with the environment. Both model systems have been treated with the master equation approach, which has proven to adequately describe the dynamics of systems that are weakly coupled to electron baths. In chapter 4, we advanced from the weak coupling approximation and showed first results obtained by non-equilibrium QMC, a numerical method capable to describe the time evolution of systems with arbitrary interactions and couplings. We implemented strong-coupling and weak-coupling versions of the non-equilibrium QMC and discussed results for the magnetic impurity model. In the following, the main findings are discussed in detail.

In **chapter 2**, we have studied the charging times emerging in the time evolution of a multi-level quantum dot with full Coulomb interaction coupled to an electron gas, after a sudden change in the gate potential. Exact diagonalization and the master equation approach have been employed to reveal various contributing factors that determine the defining time scales:

- degeneracy of the few-electron states in the quantum dot,
- exchange and Coulomb correlations emerging between electrons,
- internal orbital and spin relaxation,
- wave function overlap between electrons in the quantum dot and electron gas.

The charging times in a toy model of a single-level quantum dot can be directly related to the degeneracy of the system. We have have extended the analysis to a multi-level

quantum dot for which the tunneling rates are no longer uniquely determined by the degeneracy. In particular, charging times of few-electron states are prolonged due to exchange correlations prevalent in many-electron states that act to reduce the magnitude of spectral weights. This shows that the inclusion of correlated many-body states is particularly important in the description of charge dynamics in strongly interacting quantum dots.

Furthermore, we studied the effect of orbital relaxation and spin relaxation on the charging rates. While a direct observation of relaxation rates in the time-dependent occupation of the quantum dot is not possible, internal relaxation affects the number of available tunneling channels as well as the magnitude of transients in $dn(t)/dV$. In systems with long spin relaxation times, a transient occupation of excited states is available, leading to huge charging rates compared to single-particle tunneling times. The presented results show that the impact of internal relaxation is only observable in the transient behavior on time scales of the single-particle tunneling time and can serve as a reference for future experiments. Moreover, we investigated the effect of the wave function overlap between quantum dot and electron gas, which shows a strong dependence on the quantum dot size and the carrier concentration in the electron gas. For designated parameters, a stronger tunneling into ground states or excited states can be induced.

The analysis has shown that the presented theoretical approach provides a sound framework for the interpretation of experimental findings and for the disentanglement of effects observed. As experiments approach smaller ensembles of quantum dots and ultimately the single quantum dot limit, the presented theory can be used as a starting point for the targeted design of experiments to study the charging dynamics of quantum dot systems when brought out of equilibrium.

The analysis conducted in chapter 2 demonstrated the wealth of information about the quantum dot system that is obtainable from the time scales involved in the dynamics. In **chapter 3**, we extended the study to the time-dependent spin switching and noise in a small ferromagnetic cluster that is deposited on a conducting substrate and tunnel coupled to a spin-polarized STM tip. By applying the master equation approach and using a spin Hamiltonian, we revealed that the dynamics of the spin fluctuations in the cluster are determined by the interplay of

- inelastic spin flips due to a spin-polarized current,
- magnetic relaxation of the cluster spin,
- substrate-mediated magnetization tunneling.

We have investigated the dynamics of a cluster with a degenerate ground state in the

regime where the tunneling electrons from the tip represent a weak perturbation to the cluster. In this regime, we could show that the spin fluctuations of the system effectively resemble the spin noise of a two-level system. The dependence of the effective switching rate on the external parameters voltage, temperature and magnetic field allowed us to infer the underlying interplay of inelastic spin flips and anisotropy. This ultimately allowed for the interpretation of recent experimental results on small iron clusters [15].

In particular, we determined bias-dependent spin switching for voltages above the magnetic excitation energy that is caused by current-induced spin flips in the cluster. The occurrence of a threshold bias demonstrates the quantized nature of the spin in the system under study. For bias voltages below the magnetic excitation energy, the excitation of the cluster in the spin Hamiltonian model is suppressed at low temperatures. Another crossover has been found in the temperature dependence of spin fluctuations. For temperatures above the spin excitation energy, the cluster is thermally excited and the spin fluctuation corresponds to an Arrhenius-type spin switching. At low temperatures, however, thermal excitations are suppressed and we find that spin fluctuations are caused by the interplay of substrate electrons and transverse magnetic anisotropy, which leads to magnetization tunneling. In this regime, spin fluctuations linearly dependent on the temperature, which can serve as an experimental indicator for magnetization tunneling.

Furthermore, the introduction of a magnetic field revealed the effect of spin-transfer torque due to a spin-polarized current on the dynamics in the cluster. The polarization of the tip introduces an imbalance between current-induced spin-flips associated with an increasing and decreasing cluster spin, respectively. We find that the competition between current-induced spin-transfer torque and the external magnetic field determines the occupation of the two lowest energy states in the cluster.

The presented system was described by an effective total spin in the spin Hamiltonian framework and under the assumption of fast decoherence of the cluster compared to the switching dynamics. This gives rise to the question how the behavior of spin noise changes in the regime where the coherence time is of the order of the switching time. Furthermore, the presented framework has the potential to be extended in order to treat multiple weakly coupled atoms or clusters. In these systems, the direct interaction is weak. The spins, however, are coupled by means of an indirect interaction through electrons of the conducting substrate (Ruderman-Kittel-Kasuya-Yosida interaction). These systems show complex collective behavior and the understanding of their dynamics is of importance in pursuing the goal of implementing logic gates in an atomic scale device [170].

In **chapter 4**, we have applied the quantum Monte Carlo approach for transport dynamics that is based on the stochastic sampling of the Keldysh path integral. We have implemented expansions in

- the Coulomb interaction strength,
- the tunnel-coupling between quantum dot and leads.

Both approaches suffer from the dynamic sign problem, which is the limiting factor of QMC calculations and makes the simulation of long times prohibitively difficult.

For weakly interacting quantum dots, the presented weak-coupling approach can be carried out for longer times compared to the strong-coupling approach that expands in terms of the tunnel coupling. However, as an expansion around the non-interacting system, the average expansion order grows with the strength of the Coulomb interaction. This makes it preferable for systems with weak to intermediate interaction strengths.

Unfavorable convergence properties have been determined in the expansion in the tunnel coupling. Here, however, the decay of the average sign turns out to be almost independent of the quantum dot energies, making this approach suitable for all interaction strengths and for the study of crossovers between interaction regimes.

We have also demonstrated that the QMC approach has the potential to be used for the simulation of small systems with additional degrees of freedom based on the example of the magnetic impurity model. In particular, we discussed the dynamics of a quantum spin $1/2$ incorporated into a single-level quantum dot, which serves as a minimal model for, e.g., magnetic impurities embedded in quantum dots or the interaction between nuclei spins and electrons.

Strong-coupling QMC allowed studying the dynamics of the impurity and electrons in the quantum dot after the coupling to leads is switched on. The time evolution from non-equilibrium to equilibrium has been studied for the parameter crossover from weak to strong exchange interaction. For weak-exchange coupling between impurity and electrons, we find a reasonable agreement with the mean-field type approach, suggesting that the impurities act as an effective magnetic field in the dynamics of the electrons.

Furthermore, the impurity spin shows slow relaxation that occurs on time scales much larger than the transient electron dynamics. A larger exchange-coupling, on the other hand, results in an enhanced impact of coherent electron-impurity flip-flops and induces transient spin accumulation on the quantum dot. In this regime, fluctuations of the impurity spin additionally suppress the quantum dot's double occupancy.

The study is a first step toward the investigation of the coherent dynamics in more complicated systems like dilute magnetic quantum dots with multiple impurities or atomic

clusters when brought out of equilibrium.

In the presented study, the non-equilibrium QMC approach proved to be a promising tool to investigate the dynamics in the crossover between parameter regimes and systems without small expansion parameters, i.e. the deep quantum regime. Compared to other non-equilibrium approaches, quantum Monte Carlo has the general advantage to be numerically exact within the given stochastic error bars. There are no approximations like discretization or truncations.

Crucial for the general applicability of quantum Monte Carlo is the handling of the dynamic sign problem with the aim to approach longer simulation times. We demonstrated that the introduction of auxiliary parameters can be one step toward reaching this goal and further optimizations seem to be worthwhile.

This page intentionally left blank.

References

[1] T. A. Fulton and G. J. Dolan, Physical Review Letters **59**, 109 (1987).

[2] H. Grabert, M. H. Devoret, and M. Kastner, Physics Today **46**, 62 (1993).

[3] S. Cronenwett, T. Oosterkamp, and L. Kouwenhoven, Science **281**, 540 (1998).

[4] W. B. Thimm, J. Kroha, and J. von Delft, Physical Review Letters **82**, 2143 (1999).

[5] J. Kondo, Progress of Theoretical Physics **32**, 37 (1964).

[6] D. Loss and D. DiVincenzo, Physical Review A **57**, 120 (1998).

[7] D. D. Awschalom, D. Loss, and N. Samarth, *Semiconductor spintronics and quantum computation* (Springer, Berlin, 2002).

[8] A. Stolow, A. E. Bragg, and D. M. Neumark, Chemical Reviews **104**, 1719 (2004).

[9] B. Marquardt *et al.*, Nature Communications **2**, 209 (2011).

[10] C. R. Moon *et al.*, Nature Nanotechnology **4**, 167 (2009).

[11] F. Meier, L. Zhou, J. Wiebe, and R. Wiesendanger, Science **320**, 82 (2008).

[12] A. A. Khajetoorians, J. Wiebe, B. Chilian, and R. Wiesendanger, Science **332**, 1062 (2011).

[13] S. Loth *et al.*, Science **329**, 1628 (2010).

[14] S. Loth *et al.*, Science **335**, 196 (2012).

[15] A. A. Khajetoorians *et al.*, Science **339**, 55 (2013).

[16] H. Schoeller and J. König, Physical Review Letters **84**, 3786 (2000).

[17] S. Jakobs, V. Meden, and H. Schoeller, Physical Review Letters **99**, 150603 (2007).

[18] R. Gezzi, T. Pruschke, and V. Meden, Physical Review B **75**, 045324 (2007).

[19] D. Segal, A. Millis, and D. Reichman, Physical Review B **82**, 205323 (2010).

[20] D. Segal, A. J. Millis, and D. R. Reichman, Physical Chemistry Chemical Physics **13**, 14378 (2011).

[21] S. Weiss, J. Eckel, M. Thorwart, and R. Egger, Physical Review B **77**, 195316 (2008).

[22] D. Becker, S. Weiss, M. Thorwart, and D. Pfannkuche, New Journal of Physics **14**, 073049 (2012).

[23] P. W. Anderson, Physical Review **124**, 41 (1961).

[24] B. Marquardt *et al.*, Applied Physics Letters **99**, 223510 (2011).

[25] A. Beckel *et al.*, Applied Physics Letters **100**, 232110 (2012).

[26] D. Gatteschi, R. Sessoli, and J. Villain, *Molecular Nanomagnets* (Oxfort University Press, London, 2006).

[27] T. Schuh *et al.*, Journal of Applied Physics **107**, 09E156 (2010).

[28] A. Furrer and O. Waldmann, International Journal of Modern Physics B **24**, 3653 (2010).

[29] S. Krause *et al.*, Physical Review Letters **107**, 186601 (2011).

[30] L. Mühlbacher and E. Rabani, Physical Review Letters **100**, 176403 (2008).

[31] T. Schmidt, P. Werner, L. Mühlbacher, and A. Komnik, Physical Review B **78**, 235110 (2008).

[32] P. Werner, T. Oka, M. Eckstein, and A. J. Millis, Physical Review B **81**, 035108 (2010).

[33] J. Climente, M. Korkusiski, P. Hawrylak, and J. Planelles, Physical Review B **71**, 125321 (2005).

[34] Y. Léger *et al.*, Physical Review Letters **97**, 107401 (2006).

[35] F. H. L. Koppens *et al.*, Nature **442**, 766 (2006).

[36] C. López-Monís, J. Iñarrea, and G. Platero, New Journal of Physics **13**, 053010 (2011).

[37] J. Bardeen, Physical Review Letters **6**, 57 (1961).

[38] M. Cohen, L. Falicov, and J. Phillips, Physical Review Letters **8**, 316 (1962).

[39] J. Rammer, *Quantum Field Theory of Non-equilibrium States* (Cambridge University Press, Cambridge, 2007).

[40] H. Haug and A.-P. Jauho, *Quantum kinetics in transport and optics of semiconductors* (Springer, Berlin, Heidelberg, New York, 2008), Vol. 123.

[41] J. Schwinger, Journal of Mathematical Physics **2**, 407 (1961).

[42] L. V. Keldysh, Sov. Phys. JETP **20**, 1018 (1965).

[43] A.-P. A. Jauho, N. Wingreen, and Y. Meir, Physical Review B **50**, 5528 (1994).

[44] M. Plihal, D. Langreth, and P. Nordlander, Physical Review B **71**, 165321 (2005).

[45] D. Langreth and P. Nordlander, Physical Review B **43**, 2541 (1991).

[46] M. Abramowitz and I. A. Stegun, *Handbook of Mathematical Functions: With Formulars, Graphs, and Mathematical Tables* (Dover Publications, New York, 1964), Vol. 55.

[47] H. P. Breuer and F. Petruccione, *The theory of open quantum systems* (Oxford University Press, USA, 2002).

[48] C. Gardiner and P. Zoller, *Quantum noise: a handbook of Markovian and non-Markovian quantum stochastic methods with applications to quantum optics* (Springer, Berlin, 2004), Vol. 56.

[49] C. Timm, Physical Review B **77**, 195416 (2008).

[50] M. Kastner, Reviews of Modern Physics **64**, 849 (1992).

[51] J. König, H. Schoeller, and G. Schön, Physical Review B **58**, 7882 (1998).

[52] R. Warburton *et al.*, Nature **405**, 926 (2000).

[53] P. Hawrylak, G. Narvaez, M. Bayer, and A. Forchel, Physical Review Letters **85**, 389 (2000).

[54] T. Köppen *et al.*, Physical Review Letters **103**, 037402 (2009).

[55] J. Elzerman *et al.*, Nature **430**, 431 (2004).

[56] S. Gustavsson *et al.*, Physical Review Letters **96**, 076605 (2006).

[57] R. Hanson *et al.*, Reviews of Modern Physics **79**, 1217 (2007).

[58] R. Hanson and D. D. Awschalom, Nature **453**, 1043 (2008).

[59] S. Gustavsson *et al.*, Physical Review B **74**, 195305 (2006).

[60] M. Geller *et al.*, Applied Physics Letters **82**, 2706 (2003).

[61] A. Marent *et al.*, Applied Physics Letters **91**, 242109 (2007).

[62] M. Russ, Ph.D. thesis, Universität Duisburg-Essen, 2006.

[63] B. Marquardt, Ph.D. thesis, Universität Duisburg-Essen, 2011.

[64] Creative Commons Attribution-NonCommercial-ShareAlike 3.0 Unported License. http://creativecommons.org/licenses/by-nc-sa/3.0/.

[65] N. Ashcroft and N. Mermin, *Solid State Physics* (Holt-Saunders, New York, 1976).

[66] C. Kittel, *Introduction to solid state physics* (Wiley, New York, 1986).

[67] S. Sze, *Physics of semiconductors* (John-Wiley and Sons, New York, 1981).

[68] S. Reimann and M. Manninen, Reviews of MPdern physics **74**, 1283 (2002).

[69] H. Grabert, Zeitschrift für Physik B Condensed Matter **85**, 319 (1991).

[70] J. Smoliner, Semiconductor Science and Technology **11**, 1 (1996).

[71] R. J. Luyken *et al.*, Applied Physics Letters **74**, 2486 (1999).

[72] J. H. Davies, *The physics of low-dimensional semiconductors* (Cambridge University Press, USA, 1997).

[73] N. G. Van Kampen, *Stochastic processes in physics and chemistry* (Elsevier B.V., Amsterdam, 1992), Vol. 1.

[74] R. Gutierrez-Osuna, H. Nagle, and S. Schiffman, Sensors and Actuators B **61**, 170 (1999).

[75] E. H. Hellen, American Journal of Physics **73**, 871 (2005).

[76] M. Kroutvar *et al.*, Nature **432**, 81 (2004).

[77] S. Amasha *et al.*, Physical Review B **78**, 041306R (2008).

[78] T. Meunier *et al.*, Physical Review Letters **98**, 126601 (2007).

[79] U. Bockelmann and G. Bastard, Physical Review B **42**, 8947 (1990).

[80] S. Erlingsson, Y. Nazarov, and V. Falko, Physical Review B **64**, 195306 (2001).

[81] S. I. Erlingsson and Y. V. Nazarov, Physical Review B **66**, 155327 (2002).

[82] W. A. Coish and D. Loss, Physical Review B **72**, 125337 (2005).

[83] G. Dresselhaus, Physical Review **100**, 580 (1955).

[84] M. Dyakonov and V. Kachorovskii, Soviet Physics Semiconductors **20**, 110 (1986).

[85] E. I. Rashba, Sov. Phys. Solid State **2**, 1109 (1960).

[86] Y. Bychkov and E. Rashba, Journal of Physics C: Solid State Physics **17**, 6039 (1984).

[87] A. Vorontsov and M. Vavilov, Physical Review Letters **101**, 226805 (2008).

[88] N. Shaji *et al.*, Nature Physics **4**, 540 (2008).

[89] D. Pfannkuche, V. Gudmundsson, and P. A. Maksym, Physical Review B **47**, 2244 (1993).

[90] R. Wiesendanger, Reviews of Modern Physics **81**, 1495 (2009).

[91] C. Rudowicz, Journal of Physics C: Solid State Physics **18**, 1415 (1985).

[92] H. A. Kramers, Proc. Amsterdam Acad. **33**, 973 (1930).

[93] S. Loth, C. P. Lutz, and A. J. Heinrich, New Journal of Physics **12**, 125021 (2010).

[94] P. Dirac, Proceedings of the Royal Society of London. Series A **123**, 714 (1929).

[95] W. Heisenberg, Zeitschrift für Physik A Hadrons and Nuclei **43**, 172 (1927).

[96] J. H. Van Vleck and J. H. van Vleck, *The theory of electric and magnetic susceptibilities* (Oxford University Press, London, 1965).

[97] D. Gatteschi and L. Sorace, Journal of Solid State Chemistry **159**, 253 (2001).

[98] L. L. Hirst, Advances in Physics **27**, 231 (1978).

[99] M. R. Calvo *et al.*, Nature **458**, 1150 (2009).

[100] F. Delgado and J. Fernández-Rossier, Physical Review B **84**, 045439 (2011).

[101] J. Schrieffer and P. Wolff, Physical Review **149**, 491 (1966).

[102] R. Žitko and J. Bonča, Physical Review B **74**, 045312 (2006).

[103] J. Fernández-Rossier, Physical Review Letters **102**, 256802 (2009).

[104] F. Delgado and J. Fernández-Rossier, Physical Review B **82**, 134414 (2010).

[105] L. Chen and C. Ting, Physical Review B **46**, 4714 (1992).

[106] S. Hershfield *et al.*, Physical Review B **47**, 1967 (1993).

[107] U. Hanke, M. Galperin, A. Chao, and N. Zou, Physical Review B **48**, 209 (1993).

[108] J. Martinek and J. Barnas, Physical Review B **60**, 246 (1999).

[109] A. Cottet and W. Belzig, Europhysics Letters (EPL) **66**, 405 (2004).

[110] A. Thielmann, M. Hettler, J. König, and G. Schön, Physical Review B **71**, 045341 (2005).

[111] W. Belzig, Physical Review B **71**, 161301R (2005).

[112] G. Kießlich *et al.*, Physical Review Letters **99**, 206602 (2007).

[113] F. Bodoky, W. Belzig, and C. Bruder, Physical Review B **77**, 035302 (2008).

[114] R. Sánchez, S. Kohler, P. Hänggi, and G. Platero, Physical Review B **77**, 035409 (2008).

[115] S. Safonov *et al.*, Physical Review Letters **91**, 136801 (2003).

[116] P. Barthold *et al.*, Physical Review Letters **96**, 246804 (2006).

[117] Y. Chen and R. Webb, Physical Review B **73**, 035424 (2006).

[118] B. Sothmann and J. König, New Journal of Physics **12**, 083028 (2010).

[119] F. Delgado and J. Fernández-Rossier, Physical Review Letters **108**, 196602 (2012).

[120] C. Flindt, T. Novotný, and A.-P. Jauho, Europhysics Letters **69**, 475 (2005).

[121] C. Flindt, Ph.D. thesis, Technical University of Denmark, 2007.

[122] C. Flindt, T. Novotný, and A.-P. Jauho, Physical Review B **70**, 205334 (2004).

[123] C. Flindt, T. Novotný, and A.-P. Jauho, Physical E **29**, 411 (2005).

[124] C. Flindt *et al.*, Physical Review Letters **100**, 150601 (2008).

[125] *Quantum Noise in Mesoscopic Physics*, edited by Y. V. Nazarov (Springer, Berlin, 2003).

[126] S. Machlup, Journal of Applied Physics **25**, 341 (1954).

[127] A. N. Jordan and E. V. Sukhorukov, Physical Review B **72**, 9 (2005).

[128] Z. Nussinov, M. F. Crommie, and A. V. Balatsky, Physical Review B **68**, 085402 (2003).

[129] L. Néel, Ann. Géophys. **5**, 99 (1949).

[130] W. J. Brown, Physical Review **130**, 1677 (1963).

[131] W. Wernsdorfer *et al.*, Physical Review Letters **4**, 1791 (1997).

[132] W. Wernsdorfer, Andvances in Chemical Physics **118**, 99 (2000).

[133] H. Schoeller and G. Schön, Physical Review B **50**, 18436 (1994).

[134] M. Schiró and M. Fabrizio, Physical Review B **79**, 153302 (2009).

[135] M. Schiró, Physical Review B **81**, 085126 (2010).

[136] L. Mühlbacher, D. Urban, and A. Komnik, Physical Review B **83**, 075107 (2011).

[137] M. Eckstein and P. Werner, Physical Review Letters **107**, 4 (2011).

[138] A. Koga, Physical Review B **87**, 115409 (2013).

[139] D. Goldhaber-Gordon and H. Shtrikman, Nature **391**, 1996 (1998).

[140] S. Iwai *et al.*, Physical Review Letters **91**, 057401 (2003).

[141] U. Schneider, L. Hackermüller, S. Will, and T. Best, Science **322**, 1520 (2008).

[142] A. Amaricci, C. Weber, M. Capone, and G. Kotliar, Physical Review B **86**, 085110 (2012).

[143] A. Rosch, J. Paaske, and J. Kroha, Physical Review Letters **90**, 076804 (2003).

[144] J. Paaske, a. Rosch, and P. Wölfle, Physical Review B **69**, 155330 (2004).

[145] S. Kehrein, Physical Review Letters **95**, 056602 (2005).

[146] F. Anders and A. Schiller, Physical Review B **74**, 245113 (2006).

[147] N. Makri, Journal of Mathematical Physics **36**, 2430 (1995).

[148] S. Weiss, J. Eckel, M. Thorwart, and R. Egger, Physical Review B **79**, 249901 (2009).

[149] S. Bedkihal and D. Segal, Physical Review B **85**, 155324 (2012).

[150] A. Rubtsov, V. Savkin, and A. Lichtenstein, Physical Review B **72**, 035122 (2005).

[151] P. Werner, T. Oka, and A. Millis, Physical Review B **79**, 035320 (2009).

[152] E. Gull *et al.*, Physical Review B **83**, 075122 (2011).

[153] N. Tsuji, T. Oka, P. Werner, and H. Aoki, Physical Review Letters **106**, 10 (2011).

[154] A. Eckardt, C. Weiss, and M. Holthaus, Physical Review Letters **95**, 260404 (2005).

[155] I. Bloch, J. Dalibard, and W. Zwerger, Reviews of Modern Physics **80**, 885 (2008).

[156] M. Takahashi and M. Imada, Journal of the Physical Society of ... **53**, 963 (1984).

[157] D. M. Ceperley, in *Monte Carlo and Molecular Dynamics of Condensed Matter Systems*, edited by K. Binder and G. Ciccotti (Editrice Compositori, Bologna, Italy, 1996).

[158] J. Kolorenč and L. Mitas, Reports on Progress in Physics **74**, 026502 (2011).

[159] E. Gull *et al.*, Reviews of Modern Physics **83**, 349 (2011).

[160] K. Binder and D. W. Heermann, *Monte Carlo simulation in statistical physics: an introduction* (Springer, Berlin, 2010).

[161] M. Troyer and U. Wiese, Physical Review Letters **94**, 170201 (2005).

[162] E. Gull, P. Werner, A. Millis, and M. Troyer, Physical Review B **76**, 235123 (2007).

[163] K. Mikelsons, A. Macridin, and M. Jarrell, Physical Review E **79**, 057701 (2009).

[164] L. Besombes *et al.*, Physical Review Letters **93**, 207403 (2004).

[165] N. Lebedeva, H. Holmberg, and P. Kuivalainen, Physical Review B **77**, 245308 (2008).

[166] S. T. Ochsenbein and D. R. Gamelin, Nature nanotechnology **6**, 112 (2010).

[167] B. Sothmann and J. König, Physical Review B **82**, 245319 (2010).

[168] M. Rudner *et al.*, Physical Review B **84**, 075339 (2011).

[169] D. Becker, Ph.D. thesis, Universtität Hamburg, 2011.

[170] A. Khajetoorians *et al.*, Physical Review Letters **106**, 6 (2011).